Rational design of nanofibrous materials

Panagiotis Angelikopoulos, M.Sc

A thesis submitted for the degree of Doctor of Philosophy.
Department of Engineering and Physical Sciences.
Heriot Watt University.
August 10, 2010

Abstract

Making Carbon nanotubes a functional material for widespread use is a very cumbersome and challenging task. Not only do CNT materials require the tubes to be well dispersed and individualized rather than in bundles but resulting material has much poorer properties than expected due to insufficient load transfer between crossing CNT. This work tries to provide insight and solutions onto both of these problems, by employing computer simulations to reveal the dual nature of surfactant mediated forces on CNT. A generic coarse grain model has been used along with a dissipative particle dynamics thermostat and implicit solvent treatment. Results illustrate that depending on the bulk concentration of surfactants and their geometry, one can control the surfatant mediated forces on tubes being able to trigger both tube gluing or dispersion. Furthermore, an adsorption study elucidating the differences between surfactant adsorption on individual tubes and their bundles has been done. Surfactants follow a superlinear synergetic adsorption isotherm on individual tubes, whereas adsorb via a Langmuir mechanism on their bundles. This work provides a solid framework of knowledge and insight regarding the nature of CNT and surfactants interaction and adsorption, providing rational arguments for the design of optimum CNT materials.

Declaration of originality

I hereby declare that the research recorded in this thesis and the thesis itself was composed and originated entirely by myself in the Department of Engineering and Physical Sciences at Heriot Watt University.

Panagiotis Angelikopoulos

Acknowledgements

Most people upon finishing their phd work address to their supervisor using scientific, stale, wooden and boring statements of thankfulness. I just feel extreme gratitude and being blessed with good luck for having Henry Bock as my phd advisor. Secondly, i would like to thank my family for without their support this thesis would never happen. There have been some people, without them i would have probably just given up. That is Dalila, Ricardo[1], michalis. Thank you guys, sincerely. I mean in just a statement its quite hard to include how i feel about it. I am quite sure though lila that you could put it in your c.v. A very special thanks to Noemie. Nono, although i don't hold the right to address you so, try to lose any contact with me please cause i don't know how can i afford to send you a whiskey for your 50th birthday! Ola-maria-aleksandra this was definitely my best year in edinburgh by far. Without you, this thesis would probably be very different...I mean, its quite hard to have such a nice time and inspire so much inspiration and feelings to anyone as you did to me. I hope you will continue to do so for a long long long time.

[1] a.k.a Don,not Xsax))

Contents

List of figures

List of tables

Acronyms and abbreviations

CGMD	= Coarse Grained Molecular Dynamics
CMC	= Critical Micelle Concentration
CNT	= Carbon Nanotube
CSD	= Cluster Size Distribution Function
DFT	= Density Functional Theory
DPD	= Dissipative Particle Dynamics
MD	= Molecular Dynamics
NH	= Nose-Hoover
NT	= Nanotube
PBC	= Periodic Boundary Condition
PMF	= Potential of Mean Force
SFT	= Surfactants
SWNT-MWNT	= Single Wall Nanotube-Multi Wall Nanotube
VMD	= Visualizing Molecular Dynamics
vdW	= van der Walls
VV	= Velocity Verlet

CHAPTER 1

Introduction

1.1 CNT properties

1.1.1 Carbon nanotubes properties and applications

Since their discovery in 1991 by Lijima [1], Carbon nanotubes and CNT materials enjoy widespread interest in research and increasing industrial attention. CNTs can be thought off as rolled up graphene sheets. In the case of Single Walled Nanotubes (SWNTs), only one sheet is used, whereas the use of more than one sheet results in the formation of a Multi Walled Nanotube (MWNT).

Among the two types of CNTs, SWNT are predicted to have higher Young's modulus $E \approx 1TPa$ and failure strength of $\sigma \approx 100GPa$, whereas MWNTs are predicted to have $E \approx 800GPa$ and $\sigma \approx 10GPa$ [2–4].

Their unique set of extraordinary properties, not only mechanical but electronic as

well, enables a number of advanced applications ranging from the medical sciences[5–7], drug delivery systems [8], catalyst support in gas diffusion electrodes [9], sensors [10–12], biomedical applications [13–15], device manufacturing [16], acoustics engineering [17], electronics [18], to composite materials [19–21]. It must be expected that many more applications will be developed in the future exploiting one or more of the CNT record properties.

Although CNTs are central to all these applications, usually they are accompanied by other materials such as polymers, for structural or functional reasons. For example, although individual nanotubes are strong, CNT materials are typically much weaker [22–25]. The weakest materials are those with a random arrangement of nanotubes such as sheets or papers [26, 27]. Their weakness is caused by the 'smoothness' of the CNTs, their weak mutual interaction and the small contact area. Deposition of material, usually polymers, between the nanotubes can improve material strength significantly [28, 29].

Additives can also enhance function: e.g. the selectivity of CNT sensors can be enhanced by coating the nanotubes with organic molecules [30]. This coating then acts as a filter letting only certain molecular species pass while blocking others. In CNT-biosensors, on the other hand, the coating might be endowed with receptors making it part of the transducer [31]. Amphiphilic molecules are often used for coatings as they can be applied conveniently from solution.

In these applications as well as in many others involving CNTs or other nanoscale building blocks it is essential that we can control the material's nanoscale structure, e.g. incomplete coating will reduce the sensors selectivity while an unnecessary thick coating might reduce sensitivity and increase response times. It is generally accepted that efficient structural control at the nanoscale can only be achieved by 'bottom-up' methods and that self-assembly processes will play a key role. Self-assembly processes are attractive as they allow us to control nanoscale features via convenient macroscopic control parameters such as concentration and temperature without direct intervention at the nanoscale.

1.1.2 Bottom-up design of a CNT material

In order to tackle the problem of low load tranfer between CNT we have concluded that material should be deposited directly on the crossing point of two tubes to act as a gluing element between the tubes (Fig. 1.1).

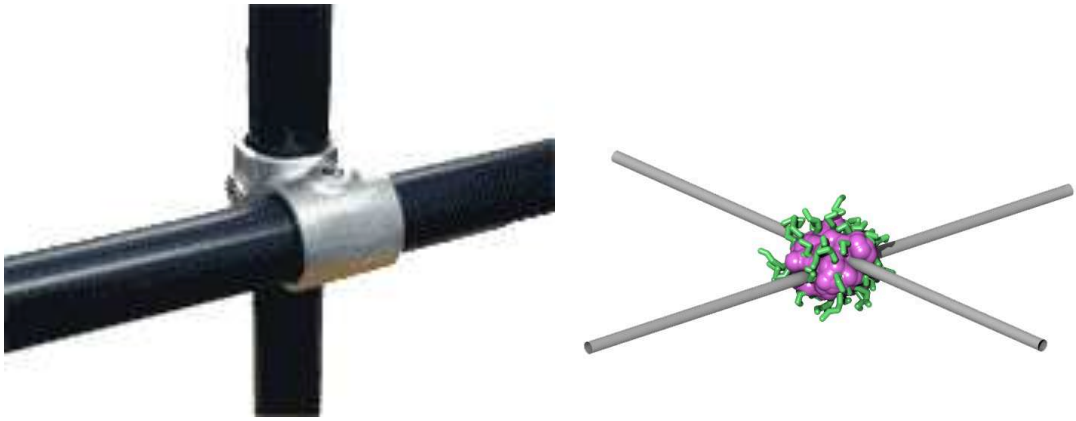

(a) Scaffolding clamp holding together two construction site tubes

(b) Surfactant micelle acting as ”glue” between crossing cNT

Figure 1.1: (a) Macrospopic analogue-solution. Tubes are clamped together with a scaffolding clamp, preventing them from sliding away. (b) Nanoscale analogue-surfactant micelle self assembled at a CNT junction acting as a localized ”glue”.

Ideally, this material would only cover that point and not fully extend onto the entire surface area of the tubes, as that would be unnecessary as it does not contribute to the strengthening might also impair certain functions. Surfactant molecules and amphiphilic polymeric molecules that self-assemble into well defined macromolecular entities, seem a perfect candidate for directed self assembly at the CNT/CNT crossing point. The deposited material on the junction would hinder CNT/CNT sliding away from each other as now many extra surfactant bonds would need to be broken. One could also polymerize the adsorbed structures, making the link between the two tubes even more stable.

In order to exploit the possibility of using SFT as a ”gluing ” agent, one must develop a thorough understanding of the underlying mechanism of directed self-assembly and the resulting structural forces. We have begun to develop this understanding, the results are represented in Chapters 5-8.

1.1.3 Carbon Nanotube dispersions stabilization

All production processes result in a CNT raw material that consist of CNT bundles (Fig.1.2).

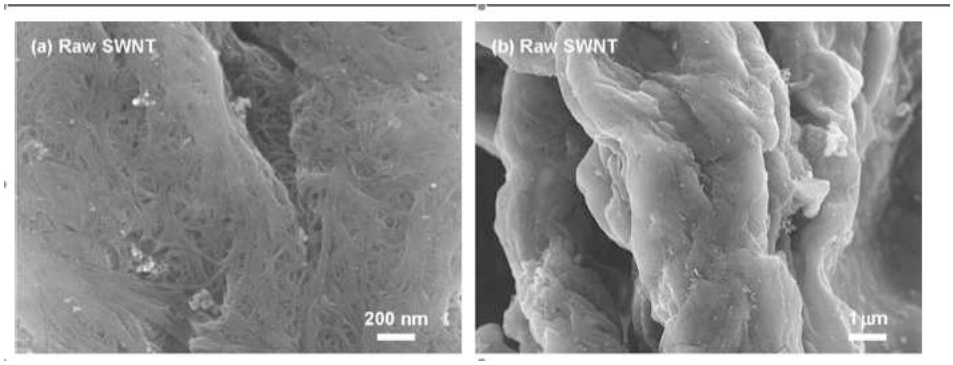

Figure 1.2: **SEM image of raw CNT**. HiPco SWCNT,scanning electron microscopy image taken from [51]

However, in the overwhelming majority of CNT applications like those discussed in section 1.1.1, individual tubes are usually desired for functional [32] or economic reasons. Unfortunately, nanotubes tend to bundle due to van der Waals interactions and in solution also because of hydrophobic interactions. The direct interactions between carbon nanotube are dominated by van der Waals (VdW) interactions if they are in vacuum. Using spectroscopic methods O'Connell et al. [33] experimentally estimated the binding energy for two nanotubes in a bundle to be approximately $500eV$ per micrometer of tube-tube contact. VdW forces between tubes have also been investigated theoretically. Schroder et al.[34] and Kleis et al. [35] have used a DFT-approach to estimate the interaction strength between parallel and concentric nanotubes. Their results suggested that the binding energy is radius dependent with larger tubes having a larger binding energy. For a pair of tubes of radius 1.2 they find a binding energy of approximately $1500eV$ per micron of tube length at a tube/tube separation of $0.552nm$. Girifalco et al, [36] use both DFT and an empirical model to estimate the van der Waals binding energy between tubes and found approximately $1000eV$ per micron of tube/tube contact at room temperature.

As carbon nanotubes are hydrophobic solvent mediated (hydrophobic) forces should be expected in (aqueous) solution[37]. The ratio between VdW and the hydrophobic

contribution, to our knowledge, remains experimentally inaccessible. Walther et al. [38] performed fully atomistic molecular dynamics simulations of single wall carbon nanotubes in SPC-modeled water. They calculate potentials of mean force for the interaction between tubes of radii $0.5 - 0.6nm$. The computed mean force exhibits an attractive maximum at a tube spacing of $0.5nm$ which corresponds to approximately one layer of interstitial water molecules. The authors suggest that the van der Waals attraction between the carbon surfaces is the dominant force by comparing their solution results to simulations of the system in vacuum. The authors estimate a tube/tube binding energy, including both VdW and hydrophobic contributions of $850eV$ per micron at a tube spacing of $0.56nm$.

While these results deviate significantly from each other they indicate that strong interactions between the tubes are rather short ranged. To eliminate bundling and its consequences, a number of methods were devised. Some are based on chemical modification of the tubes which inevitably leads to undesired deterioration of the CNT properties [39, 40]. Alternatively, non-covalent functionalization through amphiphilic self-assembly can be used to stabilize CNTs in aqueous suspensions without affecting their properties [41, 42]. The most common class of stabilizers are amphiphilic molecules such as surfactants and copolymers [41–45]. Initially, debundling is achieved by intense ultrasonication [45] after which surfactants adsorb on the CNTs and cover their surface [46]. The hydrophilic head groups of the surfactant molecules provide a steric (or electrostatic) repulsive barrier hindering or ideally preventing rebundling [47].

In the search for an optimized dispersion process, experimental studies have been conducted by various groups. The impact of surfactant concentration and the surfactants molecular structure on the number of isolated tubes in solution has been systematically investigated in a number of phenomenological studies e.g [48, 49]. However, as the interplay between surfactants and CNTs is complex and the number of potential control parameters is large, thorough undersanding and detailed insight is inevitable for successful optimization. To develop this understanding Matarredona et al.[50] and Utsumia et al.[51] measured adsorption isotherms of the surfactant NaDDBS (Sodium dodecylsulfonate benzene) on CNTs. The isotherms reveal a two-step adsorption process where the first step was attributed to adsorption on bundles and the second to exfoliation of bundles and subsequent surfactant adsorption on individual tubes. The

authors argue that at high concentrations a monolayer is formed on the tubes[50]. Similar observations were made by Xiao et al. [52] studying adsorption of the surfactant CTAB on CNTs. In this case adsorption also follows a two-step mechanism.

In all the above studies, surfactant adsorption was not directly measured and the adsorbed structures could not be observed.

Determination of the actual surfactant concentration is very challenging too, due to surfactant adsorption on all kinds of interfaces in the system, including the CNTs, the container surfaces and liquid/gas interfaces and due to the current inability to measure the adsorbed surfactant concentration directly . At concentrations below the cmc the proportion of adsorbed molecules in the system can be significant, as the cmc is usually low. An additional complication can be that the surface area of the container walls maybe of the same order-of-magnitude as the total surface area of CNTs in the sample due to the usually low CNT concentrations. An example of the ambiguity that exists in SFT/CNT adsorption isotherm measurements can be easily seen in the bulk measurements of NaDDBS adsorption on CNTs , in Refs [50] and [51]. The differences between the measured adsorbed quantity around the cmc reported in the two references are about an order of magnitude,

Computer simulations do not suffer from the problems. Here the actual concentration, the adsorbed amount and the adsorbed structures are directly accessible. A number of methods, usually using a coarse-grained description, have successfully been employed to study adsorbed structures of amphiphilic and non-amphiphilic organic molecules on CNTs and other surfaces.

1.2 Simulating carbon nanotube surfactant interactions

Wallace et al. [53, 54] used Coarse Grained Molecular Dynamics (CGMD) to investigate adsorption of DPPC lipids and two detergents, DHPC and LPC on CNTs. Depending on the type of amphiphile as well as the number of surfactant molecules in the simulation box they found a variety of adsorbed structures including randomly arranged surfactant molecules and encapsulation by spherical micelles.

Shvartzman-Cohen et al. [55, 56] used CGMD to study adsorption of amphiphilic block-copolymers on CNTs and found adsorption with no specific ordering of the adsorbed molecules. Unfortunately, the bulk properties of the model used, do not allow safe conclusions to be drawn.

Qiao et al. [57] used Molecular Dynamics to investigate the dependence of adsorbed structures on the bulk concentration and calculated the average orientation of the surfactant molecules with respect to the CNT-axis to characterize the structures. His findings support that surfactants adsorb randomly on CNT. One must note that a limited number of surfactant molecules were used in this study simulating a relatively low adsorbed density.

Düren et al. [58] used Grand Canonical Monte Carlo simulations to study gas adsorption of Methane inside CNTs. She studied the correlation between the increase in the adsorbed quantity of ethane and methane inside the CNT and the increased interaction strength between the molecules and the tubes.

Canonical Monte Carlo has been used to investigate the wrapping of polymers around CNTs in the work of Gurevitcha et al. [59]. Nativ et al. [56] used classical Molecular Dynamics to study adsorption and aggregation of amphiphilic molecules on a single wall carbon nanotube (SWCNT).

Computer simulations have also been successfully used for a detailed analysis of the system at the atomic level. Tummala et al. [60] used fully atomistic MD to study adsorption of Na-dodecyl sulphate (SDS) molecules on SWCNTs from aqueous solution. They show that the morphology of adsorbed SDS structures is influenced by the tube diameter, its chirality and by the number of SDS molecules placed in the simulation box. A variation of structures has been observed when the number of molecules in the simulation box was altered. At low coverages SDS molecules form “rings” with the SDS molecules lying flat on the tube surfaces and parallel to the tube axis. High coverages favor the formation of adsorbed micelles with disordered internal structure. Unfortunately, the high computational cost still prevents the large system sizes needed for concentration control.

Using atomistic molecular dynamics Xu et al. [61] observed a reduction of the surfactant induced tube/tube potential of mean force with decreasing SDS coverage of a

pair of parallel tubes. Uddin et al. [62] also used atomistic MD to decouple the forces between SDS-decorated parallel carbon nanotubes between surfactant mediated and direct CNT/CNT interactions. They found that adsorbed SDS molecules induce a repulsion between neighboring surfactant-decorated CNT.

Atomistic simulations offer a more detailed representation of the system. The slow characteristic time-scale for adsorption and aggregation phenomena compared with the atomistic motion makes fully atomistic MD computationally inefficient. The inability to simulate a coexistence between a bulk/ adsorption system does not allow to establish a link to experimental work via the bulk concentration. Moreover the fully atomistic models used in these works have not been tested for their bulk properties, therefore it is unknown whether they represent accurately SDS aggregation behavior. Coarse grained simulations do not suffer from this problems, as they are computationally much less demanding.

One must note that results from the above atomistic simulations do not overlap with the work presented here as the time scales studied are different, and also the system configuration differs. Furthermore our generic models retain their quantitative validity for any surfactant molecule, while these studies are limited to one specific. It is interesting though that certain findings of the fully atomistic MD corroborate our results.

1.3 Conclusions-Future Work

The work within this thesis contributes significantly towards an understanding of the complex interactions of amphiphilic molecules with CNT. More specifically, the morphology of the adsorbed layer of SFT onto CNT has been studied and its relation to bulk concentration quantified. Key differences have been found in the adsorbed layers on SWCNT and on a bundle of SWCNT. Langmuir type adsorption seems to be prevalent on the bundle cases, whereas a much more cooperative adsorption type has been found for single tubes.

Equipped with a solid understanding of the adsorbed layers, we found a way to direct self-assemble SFTs on the junctions of crossing NT. This technique gives valuable

insight to experimentalists in their efforts to create a novel strong CNT composite material. This is possible, as we have shown that surfactant have solely a gluing effect on solubilized CNT at low bulk concentrations below the CMC.

Furthermore, we have investigated the missing link, i.e the link between the adsorbed amphiphile structured and the dispersive forces that SFTs induce when adsorbed between solubilized CNT in close contact. This allowed us to state rational arguments , extremely valuable to experimentalists, on the surfactant choice optimization of CNT dispersions stabilization.

Future directions already include an almost complete guideline on predicting and linking the SFT adsorbed structure based solely on the bulk properties. Thus, sole knowledge of the bulk properties and knowledge of the tube size will be needed to anticipate the outcome and nature of the SFT interaction with the tube.

Furthermore, the fact that surfactants form well defined structures when adsorbed on CNT, allows for a higher level self assembly process, where now we are interested in possible architectures that involve many tubes interconnected into a weekly connecting network of cylindrical micelles. Such networks can greatly enhance as an example the out-coming material electronic properties, as the percolation threshold is greatly lowered.

At this point we must address the limitations of the model we have used. Most importantly, the surfactants model we used allows only for qualitative results, as all the length scales have been coarse-grained out. That is, our model does not represent one specific real surfactant, it rather emulates the generic self assembly behavior of aggregating surfactants. Most importantly, the interactions between the species in our model are effective, as a result of its coarse grained character. Tuning these interactions can result in quite a plethora of adsorbed morphologies. We have robustly determined our force field with the help of experimental results in the literature, and also tried to cross-validate our results with experimental ones, with reasonable success. The model is however sensitive in the force field set-up, as in most molecular simulations.

Rather than introduce specific improvements on the bead and spring model such as rigid beads by introducing torsional forces, future work should also point towards the choice of a specific real life set of surfactants, acquire a specific coarse grained model,

and try to work with it on a largely parallel code. This will greatly help to overcome any ambiguity in the effective interactions between the species.

As a result of using a specific SFT in the future in our simulations, the CNT model would immediately benefit, since it would be now possible to introduce flexible, buckling-able tubes in the simulations. The tubes in our simulations so far have been fixed and not allowed to move throughout the simulation. A possible buckling of the tube due to a higher temperature would change the local curvature of the tube, and thus the local potential around that point, with possible effects on the adsorbed morphology.

Furthermore, it would be advantageous during the force measurement simulations to be able to separate between effects happening due to different time scales. Surfactant self-assembly and adsorption are much faster than the diffuse thermal motion of the tubes. However, had there been any correlation between the motion of the tubes and the changes in the adsorbed morphology that would destabilize the system and lead it to a different equlibrium point would become visible in the case of movable non-fixed CNTs.

Finally it would be interesting to study the differences in self assembly of spherical nanoparticles of sizes comparable to the micelles when immersed and stabilized in different surfactant solutions. This once again would require movable objects.

1.4 Thesis outline

In Chapter 2 the model used for the surfactants and the CNTs and the computational method employed are presented.

Before embarking onto the surfactant adsorption studies, the bulk behavior of the model surfactants is analyzed in Chapter 3.

Then, in Chapter 4 we will present a thorough study of surfactant adsorption of SFT on CNT and on their bundles. This chapter has appeared in [63].

In Chapter 5, having studied the adsorption mechanism of SFTs on CNT, we investigate the directed self-assembly of surfactants onto a CNT junction formed by a pair of crossing CNT, using the bulk surfactant concentration as the sole control parameter.

The chapter has appeared in [20].

In Chapter 6 the correlation between the surfactant mediated tube/tube force and the structures of the adsorbed and self assembled structures is analyzed. The chapter has appeared in [64].

In Chapter 7 we reveals details of the mechanism by which surfactants stabilize dispersions, and examine the influence of the SFT head group on the dispersion stability. This chapter is under review for publication [65] .

In Chapter 8 we contribute to understanding experimental results of our experimental collegues at University of Edinburgh, regarding the individualization of CNT below the CMC. The chapter has appeared in [46] and is appended at the end of the thesis.

CHAPTER 2

Methodology

In this chapter the methodology used in this work is described and the creation, validation and reasoning for the model used are presented. The concepts and systems introduced in the previous chapter are described in the context of molecular modelling and simulations. We first address the surfactant and CNT model used throughout this work. A discussion regarding the validity and creation of our model, more specifically the determination of the surfactant/carbon nanotube interaction follows. Subsequently we focus on the computational method used to simulate our model, more specifically DPD-thermostated molecular dynamics. The key concepts of dissipative particle dynamics will be introduced, as well as some specific details regarding the computational implementation.

2.1 Description of the model

2.1.1 Surfactants

Surfactants are molecules of amphiphilic character. This means that the same molecule has a hydrophilic part as well as a hydrophobic one. In our simulations surfactant molecules are represented by a chain of beads (H_xT_y) consisting of a block of x hydrophilic head (H) beads and a block of y hydrophobic tail (T) beads (Fig. 2.1).

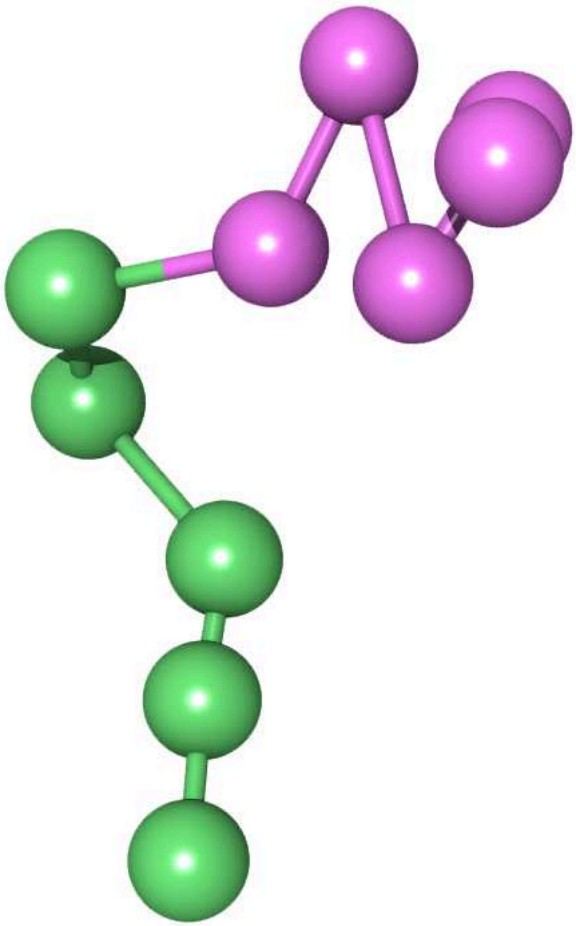

Figure 2.1: **Surfactant bead and spring model**. Snapshot of a single H_5T_5 surfactant chain. Hydrophilic heads are shown in green, hydrophobic tails in purple. Bonds between all beads are harmonic with the same spring constant. No bond torsion forces or angular forces are applied to the chains.

In molecular simulations the computational cost scales at best linearly with the num-

ber of interaction centers simulated. In solvent/solute simulations at low solute concentrations, solvent interaction centers constitute the overwhelming majority. As an average estimation, the ratio of solvent/solute interactions dominate the computational cost. The great computational cost of all atom solvent simulations, makes events like aggregation and adsorption even with modern supercomputers difficult to study due to the great separation between the characteristic time scales of the effects studied and the time scale of the motion of atoms. Therefore an implicit treatment of the solvent is used. Rather than simulating its individual molecules, the solvent effects will be incorporated as pairwise-forces acting between the solute particles.

The implicit treatment of the solvent causes the beads to interact via effective potentials. In the present case we employ a common bead-spring empirical model (Fig. 2.1) where the interactions between a pair of hydrophobic beads is attractive, while all other bead/bead interactions are repulsive.

Attractive interactions between beads i and j are represented by the pair potential $\phi(r_{ij})$ which is based on the force shifted Lennard-Jones (LJ)(12,6) potential

$$\phi_{\mathrm{LJ}}(r_{ij}) = 4\epsilon \left[\left(\frac{\sigma}{r_{ij}} \right)^{12} - \left(\frac{\sigma}{(r_{ij})} \right)^{6} \right] \tag{2.1}$$

$$\phi(r_{ij}) = \begin{cases} \phi_{\mathrm{LJ}}(r_{ij}) - \phi'_{\mathrm{LJ}}(r_{\mathrm{cut}}) r_{ij} - \phi_{\mathrm{LJ}}(r_{\mathrm{cut}}) & r_{ij} < r_{\mathrm{cut}} \\ 0 & r_{ij} \geq r_{\mathrm{cut}}, \end{cases} \tag{2.2}$$

where $\phi'_{\mathrm{LJ}}(r) = d\phi_{\mathrm{LJ}}(r)/dr$ and r_{cut} is the cut-off-radius. In eq.(2.1) $r_{ij} = \|\mathbf{r}_{ij}\|$, $\mathbf{r}_{ij} = \mathbf{r}_j - \mathbf{r}_i$ and $\mathbf{r}_i$ and $\mathbf{r}_j$ are the positions of beads i and j, respectively; ϵ is the well depth and σ the length parameter of the LJ potential. The potential is presented in figure 2.2.

Repulsive interactions are represented by the Weeks-Chandler-Anderson (WCA) potential given by eq.(2.2) with $r_{\mathrm{cut}} = 2^{1/6}$. For simplicity, these interactions are assumed to be present between all pairs of beads regardless whether they are bonded or not. In addition, in order to describe the structure of a molecule, two beads k and l which are nearest neighbors in a single surfactant chain interact via the harmonic bond potential

$$\phi_{\mathrm{bond}}(r_{kl}) = \epsilon_{\mathrm{bond}}(r_{kl} - r_{\mathrm{bond}})^2, \tag{2.3}$$

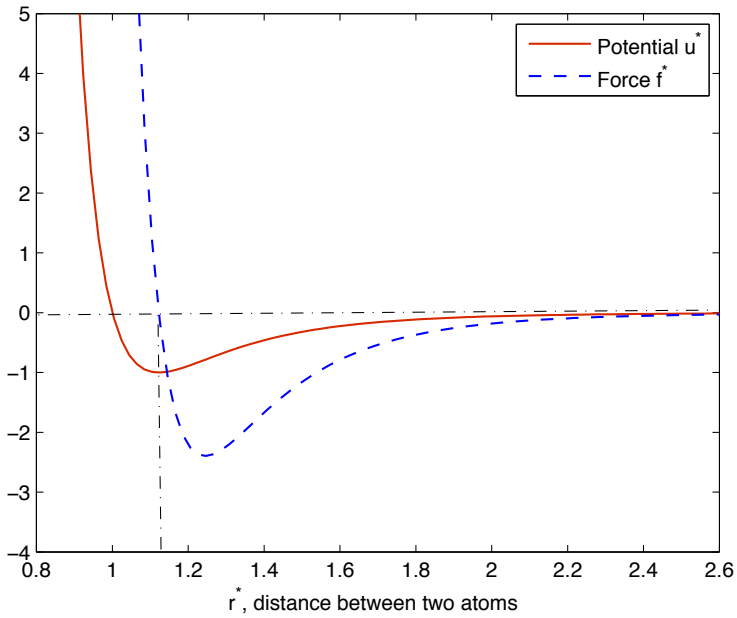

Figure 2.2: Lennard-Jones (12,6) pair potential and pair force in reduced units. See section 2.1.1.1.

where ϵ_{bond} is the depth of the potential well and r_{bond} the bond length.

Superposition of the nonbonding interaction and the harmonic bond potential with $\epsilon_{\text{bond}} = 4\epsilon$ and $r_{\text{bond}} = 1.2\sigma$ leads to an average nearest neighbor H/H distance of 1.35σ and a T/T distance of 1.26σ. Thus, surfactant molecules are represented by a not too loose chain of beads.

2.1.1.1 Reduced Units

Throughout the thesis, we use reduced quantities: lengths are given in units of the LJ length parameter σ, the energy is scaled with the well depth of the LJ interaction ϵ, the temperature scale is given in terms of ϵ/k_B and time is represented in units of $\sqrt{m\sigma^2/\epsilon}$, where m is the mass of a bead. Concentrations are defined as molecular number densities and given in units of $1/\sigma^3$.

2.1.2 CNT/surfactants

At the length scale of the coarse-grained surfactant beads the atomistic structure of the nanotubes becomes (essentially) irrelevant and surfactant beads interact with the mean-field of the nanotube. Therefore we model the nanotubes as smooth cylinders. They interact with the hydrophobic surfactant beads via the force shifted Lennard-Jones (12,6) potential in eq.(2.2) which is also shifted to the surface of the nanotubes

$$\phi_{\mathrm{CNT}}(r_i) = \frac{\epsilon_{\mathrm{CNT}}}{\epsilon}\phi(r_i - r_{\mathrm{CNT}}) \tag{2.4}$$

where r_i is the shortest distance between bead i and the nanotube axis (for the formula see e.g. Ref.[66]) and r_{CNT} is the radius of the nanotube. Interactions of the hydrophilic head beads with the nanotubes are modeled using the WCA potential, i.e. $\phi_{\mathrm{CNT}}(r_i)$ with $r_{\mathrm{cut}} = 2^{1/6}$.

2.1.3 Model justification

While the present model has been widely used two specific features, i.e.the form and especially the well depth of the interaction between surfactant beads and the nanotubes, deserve a more detailed discussion. For this interaction we assume a LJ (12,6) potential because of its simple mathematical form and because it describes the actual physical situation well. Single wall carbon nanotubes consist of a single layer of carbon atoms located on the surface of a cylinder. Mean-field approximation for the interaction of a single LJ particle with a single planar layer of LJ particles leads to a (10,4) potential [67]. Because of the curvature of the cylinder the mean-field potential is slightly steeper in the case of CNTs (see [68] for the formal prove and [69] for an approximation). Thus, the resulting potential is very similar to a LJ (12,6) potential. Moreover, Patel et al. have fitted an LJ (12,6) potential to the potential of mean force between a carbon nanotube and methane (CH_4) molecules in water obtained from MD simulations and found excellent agreement [70]. The latter result is of particular relevance as it includes also the hydrophobic interaction. Thus, at the level of detail considered here the LJ (12,6) potential is a very reasonable choice.

As the focus of this work is to investigate adsorption and aggregation of surfactant molecules on CNTs it is important to use a value for the ratio $\epsilon_{\mathrm{CNT}}/\epsilon$ that is realis-

tic and could be reproduced experimentally. The bead/bead interaction consists of at least two parts: the van der Waals interaction and the (effective) hydrophobic interaction, and is usually vastly dominated by the hydrophobic part. Calculations using the potential form of Ref. [69] reveal that for typical single wall carbon nanotubes with radii of a few nm the well depth of the van der Waals bead/nanotube interaction is approximately 2.7 times deeper than that of the bead/bead interaction. To estimate the ratio of the strength of the hydrophobic part of the bead/nanotube and that of the bead/bead interaction we estimate the ratio of the excluded surface areas. As a crude approximation it can be assumed that the strength of the hydrophobic interaction between two hydrophobic particles depends linearly on the size of the surface area that becomes unavailable to the solvent upon contact of the particles [71]. In the present case of spherical beads and cylindrical nanotubes we find a ratio of the bead/nanotube to the bead/bead hydrophobic interaction of approximately 1.37.

This calculation is done as follows: As a crude estimate it can be assumed that the surface energy of the interface between a hydrophobic solute and a hydrophilic solvent scales linearly with the solvent accessible surface area (sasa), that is the surface area that is available to the solvent (e.g. water). If two hydrophobic solute particles come near each other the sasa decreases, resulting in a free energy reduction of the system which causes the effective attraction we call "hydrophobic interaction". If we further assume that the surface energy is dominated by water and depends little on the specific hydrophobic surface, the strength of the hydrophobic interaction between two hydrophobic solutes is roughly proportional to the reduction in the sasa upon their contact.

For the present study we need to determine the ratio between the hydrophobic bead/bead interaction and hydrophobic bead/CNT . According to the discussion above this ratio is identical to the ratio of the excluded solvent accessible surface areas (xsasa). In order to calculate this we need to specify some of the length scales in the system. For the present estimate we assume a single wall CNT with a diameter of 1nm and water molecules to have a radius of 0.16nm. The diameter of a surfactant bead in our model (table 4.1) is half the diameter of the nanotubes, thus, 0.5nm. The xsasa for two spherical surfactant beads can be calculated analytically [72], while we obtain the xsasa of the bead/nanotube contact via Monte Carlo integration. From these calculations we

estimate the ratio of the hydrophobic bead/bead and the hydrophobic bead/nanotube interactions to be approximately 1.37.

If we now assume that the hydrophobic interaction contributes 90% of the total interaction ([73]) we find $\epsilon_{CNT}/\epsilon \approx 1.5$. On the other hand Walther et al. [38] performing united atoms MD, measured that the hydrophobic interaction between two CNT only has a contribution on the range of the total potential, making it slighter longer ranged, with the Van der Waals forces being dominant over the total interaction magnitude. Assuming that vdW interactions are dominating the SFT/CNT interaction, we result in $\epsilon_{CNT}/\epsilon \approx 2.7$. This strong interaction can be also achieved by surfactants that have aromatic rings like pyrine in the end of their tail which result in $\pi - \pi$ stacking interactions with the CNT. Thus, our choice of $\epsilon_{CNT}/\epsilon \approx 2.5$ is based on moderately strongly adsorbing surfactants on CNT.

Our model, which is empirical and contains no fitted parameter, is also validated by comparison with experiments. The model predicts that the ratio between the critical surface aggregation concentration and the cmc $C_{csac}/C_{cmc} \approx 0.3$. Matarredona et al. have measured NaDDBs adsorption on CNTs from aqueous solution and find $C_{csac}/C_{cmc} \approx 0.1$ [50] which is in reasonable agreement with our results. It is also important to realize that one has some control over the strength of the van der Waals and the hydrophobic interaction in practice. The van der Waals interactions can be altered by altering the chemistry of the surfactants while the hydrophilicity of the solvent can be controlled using cosolvents (see e.g. Ref. [74]).

2.2 Molecular dynamics

Having defined our model system in the previous section, we now describe the simulation method chosen. One of the most extensively used methods in computer simulations of membranes, peptides, lipids, nanoparticles and other nano scale systems is *molecular dynamics* (MD). MD has been particularly useful for simulating systems at the atomic level that are often difficult to study experimentally due to nanoscopic length and time scales associated with molecular structures and motions (Figure 2.3).

Although molecular dynamics (MD) simulations can be complicated, the main concept

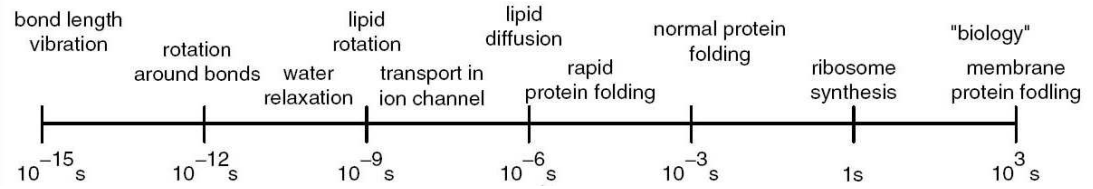

Figure 2.3: **Timescales in biomolecular systems**. With the recent developments in molecular modelling and parallel computing, it is possible to simulate on a microsecond scale. Figure adapted from [75].

behind MD is simple. Given a system of N atoms or molecules, by calculating the forces on each of these particles at a particular time, one can obtain a trajectory that specifies the positions and the velocities of the particles as a function of time, by using Newton's law of motion,

$$\mathbf{F_i} = m_i \frac{d^2\mathbf{r_i}}{dt^2},\ i = 1, 2, \ldots, N \tag{2.5}$$

where $\mathbf{F_i}$ is the force acting on particle i, m_i its mass and $\mathbf{r_i}$ its position. The force $\mathbf{F_i}$ is the negative derivative of the interaction potential V between the particles i and all other particles $\sum_i \phi(r_{ij})$,

$$\mathbf{F_i} = -\frac{dV(\mathbf{r_1}, \ldots, \mathbf{r_N})}{d\mathbf{r_i}}. \tag{2.6}$$

Once the forces are computed, equation (2.5) is integrated numerically in order to produce the new positions and new velocities of each particle of the system. The new coordinates and velocities are used to calculate the potential energy again (see Figure 2.4). Successive configurations of the system are generated in the same way, resulting in a trajectory that specifies the positions and the velocities of the particles of the system as a function of time. Therefore, molecular dynamics is a deterministic technique: with a set of initial positions and velocities given as input, one can *in principle* determine the evolution of a system.

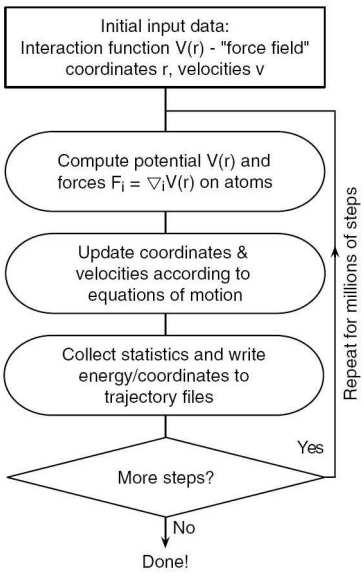

Figure 2.4: **Molecular dynamics flowchart**. Given an initial configuration of a system of N atoms or molecules, by calculating the forces on each of these particles at a particular time, one can obtain a trajectory that specifies the positions and the velocities of the particles as a function of time, by using the Newton's law of motion. A typical time step can be on the order of 1 or 2 fs for fully atomistic simulations. Figure adapted from [75].

2.3 Dissipative Particle Dynamics

In order for our simulations to be qualitatively comparable with real experiments, we want to keep some of the system parameters constant. One very important parameter is temperature (T). There are many different methods to keep the temperature constant during an MD simulation, a review of which can be found in Ref [76]. Dissipative Particle Dynamics (DPD) is one possibility to do this as the DPD simulations produce a canonical ensemble (NVT) as opposed to the microcanonical enseble (NVE) generated by standard MD . Since we have already defined our model, including all interactions , both repulsive and attractive, we will only borrow the original DPD thermostat as it is ideally suited for our bead and spring model and implicit solvent representation.

In the DPD framework, the total force on each bead is due to a combination of direct interactions with other interaction centers and random and dissipative forces. The trajectory of the system is calculated by integrating Langevin's law of motion. System properties can then be defined from its trajectory via time average. In DPD two beads

i and j interact via the pairwise force

$$F_{ij} = F_{ij}^C + F_{ij}^R + F_{ij}^D \tag{2.7}$$

where F_{ij}^C, F_{ij}^R and F_{ij}^D are the conservative, the random and the dissipative force, respectively.

The conservative force acts along the line connecting i and j , $\widehat{\mathbf{r}}_{ij} = \mathbf{r}_{ij}/\|\mathbf{r}_{ij}\|$, and depends only on the distance r_{ij} between i and j. It is given by the first derivative of the interaction potentials discussed above

$$F_{ij}^C = \begin{cases} -\left[\phi'(r_{ij}) + \phi'_{\text{bond}}(r_{ij})\right]\widehat{\mathbf{r}}_{ij} & \text{nearest neighbors} \\ -\phi'(r_{ij})\widehat{\mathbf{r}}_{ij} & \text{else} \end{cases} \tag{2.8}$$

The random force

$$F_{ij}^R = \begin{cases} -\xi\omega^R(r_{ij})\theta_{ij}\widehat{\mathbf{r}}_{ij}\frac{1}{\sqrt{\Delta t}} & r_{ij} \le r_c \\ 0 & r_{ij} > r_c \end{cases} \tag{2.9}$$

represents forces from the (rapidly moving) degrees of freedom which have been coarse-grained out, such as collisions with solvent particles leading to Brownian motion of solutes. In DPD these forces are assumed to be pairwise and random in strength. In eq.(2.9) Δt is the simulation time step, ξ is a parameter determining the maximal strength of the random force, $\omega^R(r_{ij})$ is a weight function characterizing its distance dependence and θ_{ij} is a random variable with limits -1 and 1, zero mean, and unit variance (see [78] for the random number generator we are using for our long trajectories). As the conservative force, the random force acts along the line connecting i and j.

The dissipative force (or drag force)

$$F_{ij}^D = \begin{cases} -\gamma\omega^D(r_{ij})(\widehat{\mathbf{r}}_{ij}\cdot\mathbf{v}_{ij})\widehat{\mathbf{r}}_{ij} & r_{ij} \le r_c \\ 0 & r_{ij} > r_c \end{cases} \tag{2.10}$$

represents the viscous drag mediated by degrees of freedom which have been coarse-grained out. In eq.(2.10) γ is the strength parameter and $\omega^D(r_{ij})$ is the weight function of the dissipative force. It is a pairwise force acting along the line connecting the inter-

acting particles i and j and it reduces the relative velocity (component along $\widehat{\mathbf{r}}_{ij}$) $\widehat{\mathbf{r}}_{ij} \cdot \mathbf{v}_{ij}$, where $\mathbf{v}_{ij} = \mathbf{v}_j - \mathbf{v}_i$ and $\mathbf{v}_i$ and $\mathbf{v}_j$ are the velocities of i and j, respectively.

In the canonical ensemble the dissipative and the random force are not independent but connected by the fluctuation dissipation theorem leading to

$$\begin{aligned} \omega^D(r_{ij}) &= \left[\omega^R(r_{ij})\right]^2 \\ \zeta^2 &= 2\gamma k_B T, \end{aligned} \tag{2.11}$$

where k_B is Botzmann's constant and T is the temperature. Thus, the random and the dissipative forces together constitute the DPD thermostat. Here we use the weight functions originally published in Ref. [79]

$$\omega^D(r_{ij}) = \begin{cases} (1 - r_{ij}/r_{\text{cut}})^2 & r_{ij} < r_{\text{cut}} \\ 0 & r_{ij} > r_{\text{cut}}, \end{cases} \tag{2.12}$$

where we have chosen $\omega^D(r)$ to be of the same range as the attractive conservative force.

In equilibrium, as a result of the DPD thermostat, the instantaneous temperature fluctuates around its mean target value, as seen in figure 2.5. It is worth noticing that the effect of the solvent is retained as faithfully as possible by incorporating the random forces eq.(2.10) to account for uncorrelated solvent contributions and by introducing an empirical potential to account for the influence of the solvent molecules on the solute in our case the surfactant molecules. The stationary solution of the stochastic differential equation that we are now numerically solving is the Boltzmann distribution and hence these simulations produce canonical time averages of the (N, V, T) ensemble.

The Langevin equations of motion are integrated using a modified velocity Verlet algorithm. For a detailed review of different integration methods, one can refer to [80]. We chose the modified Velocity-Verlet algorithm (VV) since it is the computationally cheapest method and its results are sufficiently robust. The modification is required because the force depends upon the velocity, the extra step involves a prediction followed by a correction.

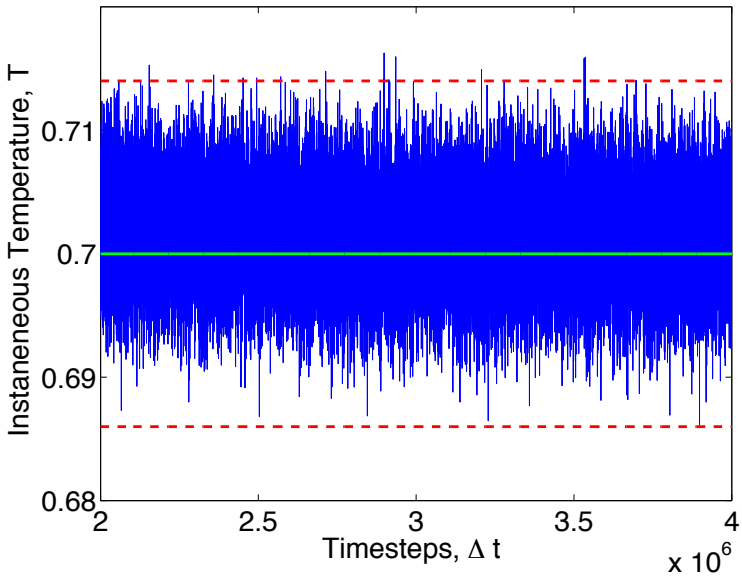

Figure 2.5: **DPD thermostat** / The Fluctuation dissipation theorem links the two DPD non conservative forces, consituting a stochastic thermostat. Its efficiency is illustrated via the 2 percent bounds are shown in red. The target temperature in green. The temperature fluctuates around the target value, and its mean value overshoots insignificantly the pre-set one as described in [77]. Data taken from a run with 2250 H_5T_5 chains over a period of $2 \cdot 10^6 \Delta t$

Some examples of the use of DPD in the field of this thesis is the study by Groot and Madden of the microphase separation of diblock co-polymer melts [79, 81]. DPD-thermostated coarse grained molecular dynamics has been utilized by Pastorino et al. to study polymeric brushes grafted on a wall [82, 83]. They also tested the efficiency of different weight functional forms for entering the DPD thermostat formalism. They noted that a constant weight function thermostats the system more efficiently. Finally, Glotzer et al studied self-assembled mono tethered nanospheres using DPD-thermostated MD [84] .

2.4 Molecular dynamics techniques

2.4.1 Simulation box and periodic boundary conditions

In the majority of the applications of MD simulations, in order to get a realistic view of a phenomenon, one would like to be able to treat the system in a bulk environment, and not in a simulation cell of limited dimensions. In order to achieve this 'bulk'

behaviour of the system, a technique known as *periodic boundary conditions* (PBC) is used. In this technique, the single simulation cell is infinitely replicated in the three[1] cartesian dimensions forming a lattice that completely fills the space. For a rectangular simulation box, if one particle is located at position $\mathbf{r}$, then this particle represents an infinite number of particles at the following positions,

$$\mathbf{r} + k\boldsymbol{\alpha} + l\boldsymbol{\beta} + m\boldsymbol{\gamma}, \qquad k,\ l\ and\ m \in \mathbb{Z} \tag{2.13}$$

where $\boldsymbol{\alpha}$, $\boldsymbol{\beta}$ and $\boldsymbol{\gamma}$ the three vectors representing the dimensions of the simulation cell.

The most important feature of PBC is that every particle can interact not only with the particles that are already in the simulation cell, but also with the ones located in the neighbouring ones. This way, any surface effects due to the finite dimensions of the cell are eliminated. The method is strictly correct only if the smallest dimension of the simulation box is at least twice the length at which two regions in the unreplicated system become independent. If not, the PBC can induct correlations, the so called "finite size effects" (Fig. 2.6).

In all of our simulations we employ the usual periodic boundary conditions. Bulk simulations are carried out in a cubic simulation box while for the adsorption studies it is more convenient to use an elongated box that has the form of a quadratic prism (Fig. 2.7).

This allows us to study the adsorbed phase in equilibrium with a bulk (like) phase in the same system. The nanotubes are placed on one side of the box (Fig. 2.7). They are rigid and their position is fixed. Since the tubes are not allowed to move they interact with the surfactant molecules only via the conservative part of the force.

$$F_i^{\mathrm{CNT}} = \phi'_{\mathrm{CNT}}(r_i) \tag{2.14}$$

We assume that at a distance of 30σ away from the nanotube the solution exhibits bulk properties as no correlations should be longer ranged. This is important as the bulk concentration is the key link to experiments.

[1] there are cases where, depending on the system and phenomenon under study, this replication is done in one or two dimensions.

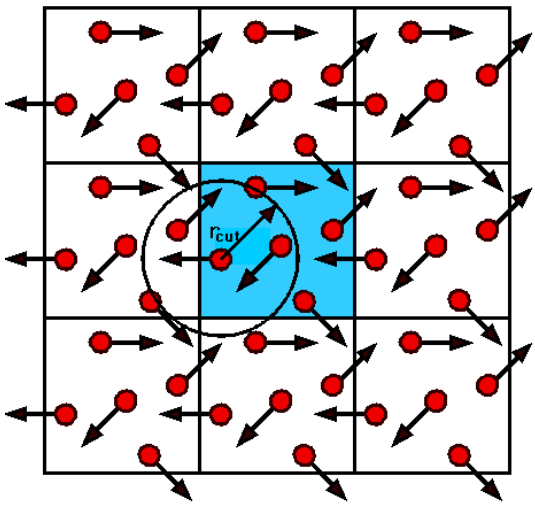

Figure 2.6: **Periodic boundary conditions**. A two dimensional representation of the periodic boundary conditions mechanism. The simulation cell, which is coloured blue, is infinitely replicated in three dimensions (only two are shown here). Once a particle 'leaves' the simulation cell, it reenters from the opposite side and the total number of particles in each cell is constant. The interaction of a particle does not only include particles from the same box, but all the particles located at a distance less than the cut-off. All the particles 'see' the system as a bulk environment (`http://www.compsoc.man.ac.uk/~lucky/Democritus/Pictures/pbc-mi.gif`).

For the adsorption simulations it is convenient to be able to fix the bulk concentration. To achieve this we perform chain insertions and deletions in the bulk-like region during the first half of the equilibration period, while in the second half the system is conventionally equilibrated in the canonical ensemble by standard DPD. Every 300 timesteps insertions or deletions are attempted if the actual concentration deviates from the target concentration by +5% or -5%, respectively. Insertion is accepted if none of the beads of the new molecule interacts with any existing chain. If this is not the case the insertion trial is repeated at different locations until it is successful. The acceptance probability is usually very high since the (bulk) concentration is very low.

2.4.2 Cell Linked List

In order to save time, the *cell linked list* simulation method [85] has been implemented. Cell lists work by subdividing the simulation domain into cells with an edge length greater than or equal to the cut-off radius of the bead/bead interactions, in our case the LJ interaction (Fig. 2.8). The particles are sorted into these cells at every timestep.

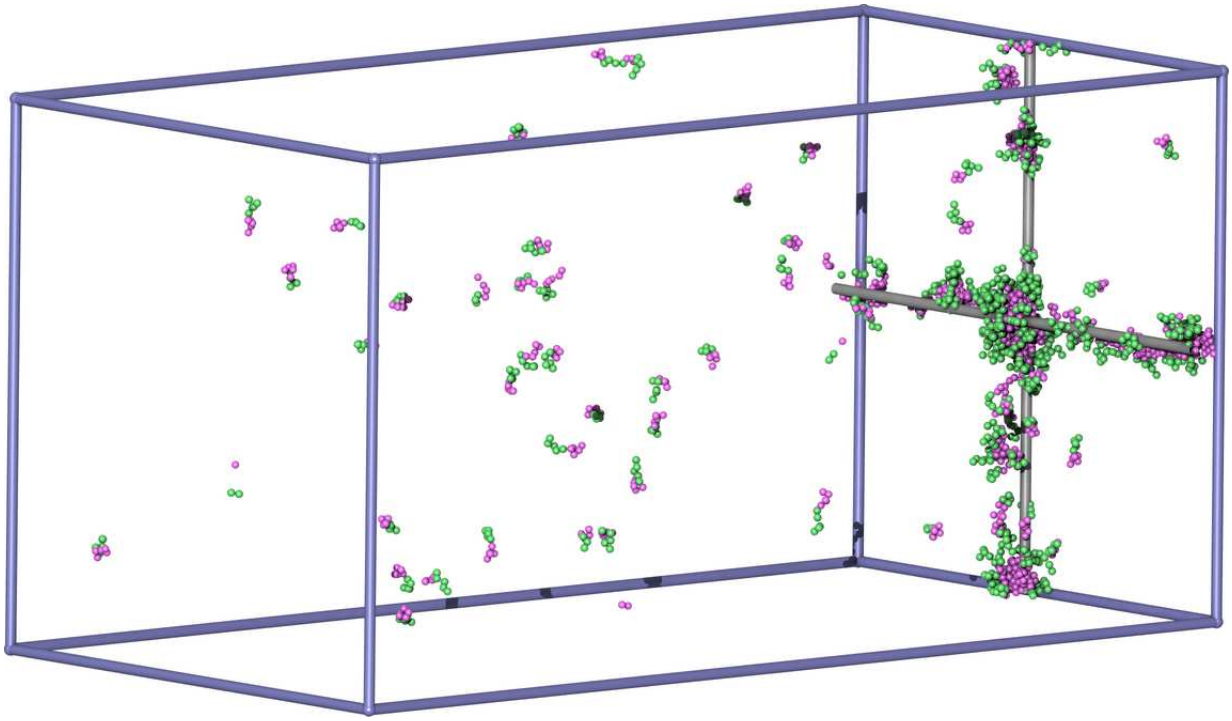

Figure 2.7: Elongated Simulation Box of size $100\sigma \times 100\sigma \times 200\sigma$. The CNTs are positioned on the far right side of the box and are partially covered with surfactant molecules. The usual periodic boundary conditions are applied in all three dimensions. Blue lines demarcate the simulation box. [20]

Potential interactions can only involve particles in neighboring cells resulting in a huge performance boost. Using the cell lists the force evaluations which represent the core of the MD code scale as $O(n \cdot log(n))$ with the number of particles n, whereas in the traditional method of testing all pairs of interaction centers it scales as $O(n^2)$.

It is well known (see e.g [86]) that the chosen size of the cell, has a strong effect on the performance of the code. A further complication arises due to the strong density inhomogeneities in our systems.

In figure 2.9 the performance dependance on the size of the cells is shown for a system containing 1000 interaction centers were used to create, and a rectangular simulation box of size $100x100x200$. If we sticked to the proposed size of just a bit bigger than the cutoff distance r_c, then we would end spending too much computational time. To tackle this problem, an adaptive cell resizing and optimizing routine has been created, which every 5 million timesteps re- adjusts the cell length to its optimum. This occurs

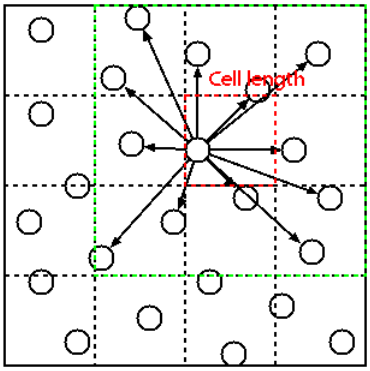

Figure 2.8: **Cell list**. The cells can be rectangular or square (or cubic in 3D). Only the neighbooring cells depicted in green color are scanned for particle-particle interactions. Figure edited from :`http://en.wikipedia.org/wiki/File:CellLists.png`

only during the equilibration period, as aggregation events still take place, changing the inhomogeneity of the system. The routine stops the normal evolution of the system, and runs 500 timesteps starting from the current state with the same seed for the random number generator but with varying the cell sizes by increments of 0.5. The cpu time that elapsed is measured for these test runs, and the cell size that provided the minimum cpu execution time is kept. Normal execution of the program then continues.

2.4.3 Simulation parameters

The simulation parameters used for each part of the study are given in tables at the beggining of each chapter.

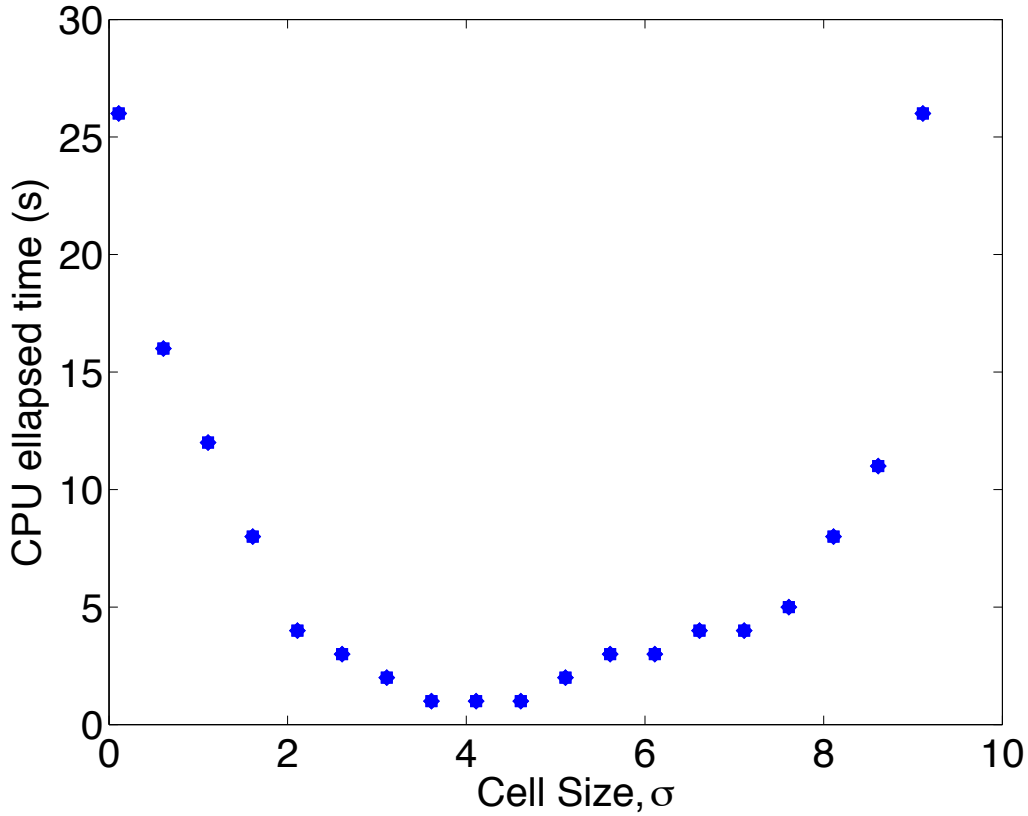

Figure 2.9: **Cell size contribution to code efficiency**. Clearly, a huge difference in the computational time arises purely by the correct choise of the cell list length. Number of particles:1000, $1000\Delta t$.

Part I

Bulk behavior

CHAPTER 3

Surfactants Bulk Behavior

3.1 Critical Micelle Concentration

In bulk solutions surfactant molecules form well defined aggregates at some threshold concentration called *critical micelle concentration* (cmc). The cmc depends on the surfactant and the solvent as well as on the thermodynamic conditions. Since our model is empirical and coarse-grained it does not represent one particular experimental solvent/surfactant combination but it describes the generic behavior of all these systems. In order to link our results to the behavior of a specific surfactant and solvent, thermodynamic reference points are needed. The most relevant reference point for self-assembly is the cmc. Therefore we carefully determine the cmc and relate all other results to it.

Here, the bulk properties of the linear surfactants H_5T_5 and H_5T_{10} are studied. The simulation parameters used are summarised in Table 3.1. Note, that not all systems

Surfactants					
T beads	=	5	H beads	=	$5, 10$
ϵ	=	1.0	σ	=	1.0
ϵ_{bond}	=	4.0	σ_{bond}	=	1.2
Simulation					
T	=	0.7	Δt	=	0.005
attractive: r_{cut}	=	2.5	repulsive: r_{cut}	=	$2^{1/6}$
non-conservative: r_{cut}	=	2.5	DPD:ξ	=	1.0
Simulation Bulk					
chains	=	$500(H_5T_5)\|800(H_{10}T_5)$	cubic box	=	variable dimensions
equilibration	=	$1 \cdot 10^8 \Delta t$	production	=	$0.5 \cdot 10^8 \Delta t$

Table 3.1: Model and simulation parameters in reduced units. Note that for $H_{10}T_5$ a larger bulk system has been used [87].

start from the same initial configuration on a lattice. This is done in order to ensure the correctnes of our method, since one should always obtain the same equilibrium properties irrespective of the starting configuration.

Some systems have been simulated by using equilibrated micellar systems simulated at a higher concentration as their initial configuration. For these runs, the box size has been increased to match the target C_{bulk}. The effects were immediate, with micelles quickly breaking up into smaller aggregates and free chains, we obtained the same equilibrium properties as for the corresponding systems that started from a lattice conformation .

During the simulation, we define that two molecules belong to the same cluster if any inter molecular tail-tail distance is smaller than 1.5σ, i.e the hydrophobic parts of the molecules are in close proximity. To identify all clusters a Depth-First-Search (DFS) algorithm is used (See e.g [88]).

The cmc indicates the surfactant concentration at which aggregation becomes relevant in the system. We can determine the cmc by plotting the concentration of free surfactant molecules C_1 as a function of the total surfactant concentration C (figure 3.1). At low concentrations no aggregates are formed and, thus, $C_1 = C$. When micelles appear the concentration of free surfactant molecules must be smaller than the total concentration as some surfactant molecules are now bound in micelles. At this point $C_1(C)$ falls below the line $C_1 = C$. After a certain "transition region" one usually observes

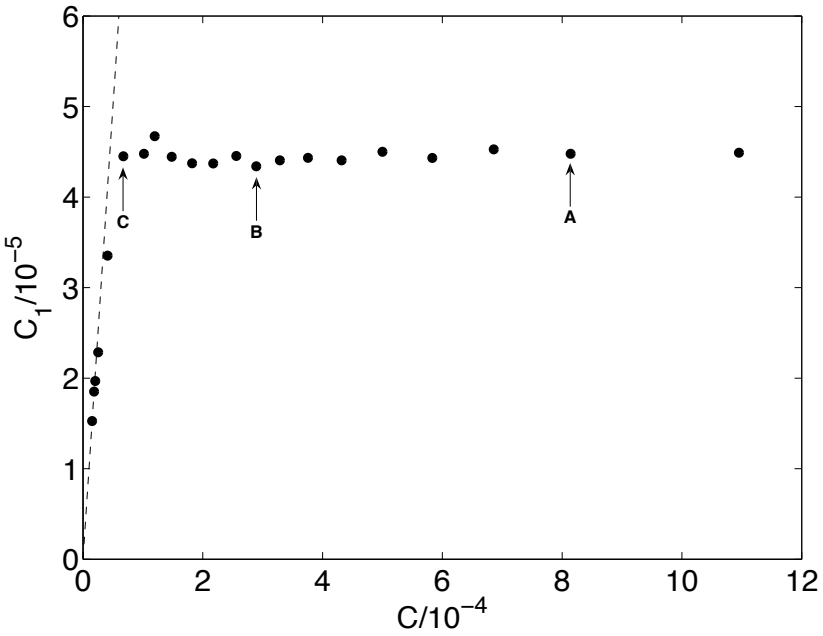

Concentration of free surfactant molecules C_1 versus the total concentration of surfactant molecules C. The dashed line demarcates $C_1 = C$ and the arrows indicate data points for which aggregation number distributions are shown in figure 3.4.

Figure 3.1: .

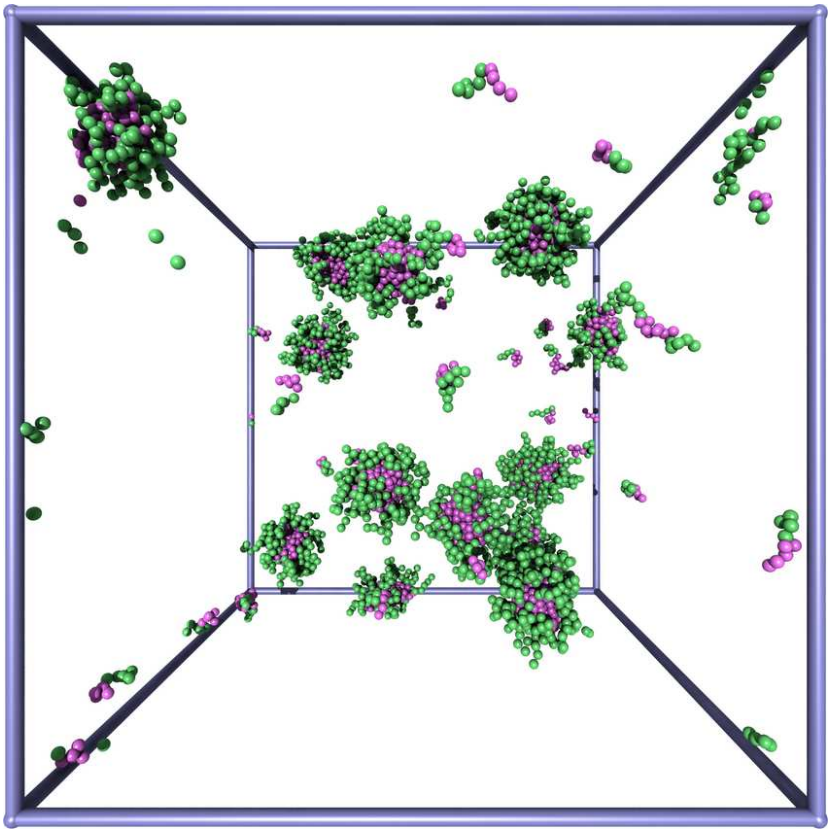

Figure 3.2: Snapshot of the H_5T_5 surfactant at $C = 8.2 \times 10^{-4} \approx 16 \times C_{\text{cmc}}$. Hydrophilic beads are shown in green while hydrophobic beads are colored purple. As the C is high, the system contains mostly micelles and only very few free surfactant molecules. The blue frame indicates the simulation box.[20]

$C_1 \approx$ const. This is easily observed in figure 3.1.

As micelle formation is a continuous process there is some arbitrariness in the definition of the cmc. Here we define the cmc as the center between the last data point which approximately follows $C_1 = C$ and the first point which belongs to the group of points for which $C_1 \approx$ const. Thus for the present system we find $CMC_{H_5T_5} = 5.2 \cdot 10^{-5}$ and $CMC_{H_{10}T_5} = 1.2 \cdot 10^{-4}$ (Data taken from [87]). $CMC_{H_5T_5} < CMC_{H_{10}T_5}$ is expected since a smaller head makes the surfactant less hydrophilic.

The snapshot in figure 3.2 gives an impression of the system at $C = 8.2 \times 10^{-4}$ which is well above the cmc.

The length of the DPD runs for collecting statistical average data is heavily relying

on the equilibration period for each chain density. The minimum simulation length was 10^8 timesteps. However, as it is obvious from the free chains evolution (Fig. 3.3), equilibration times can vary significantly . This is because the driving force for micelle formation is strong far above the CMC but becomes very low if the concentration is much more weaker when the system is close to the CMC.

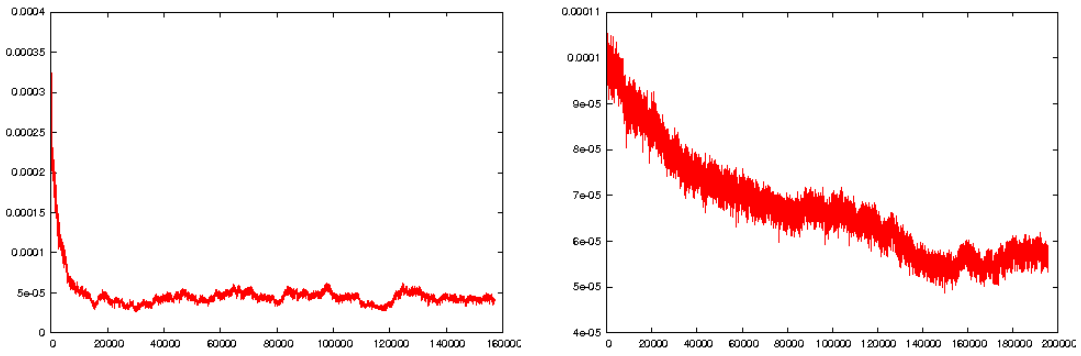

(a) $C \approx 0.75 \cdot CMC$ (b) $C \approx 0.15 \cdot CMC$

Figure 3.3: Free chains evolution vs sampling time (1 sampling period=300ΔT) for two different concentrations, one far below the CMC and one near the CMC

3.2 Geometry of the Micelles

The two simulated surfactants aggregated into micelles of approximately spherical shape in the concentration range of $CMC - 15 \cdot CMC$. Existing theory [89]states that the shape of a surfactant aggregate can be predicted by a single dimensionless parameter, called the *packing parameter* (a_p) which is defined as the ratio of the volume occupied by the surfactant tail group (V_T) over the product of the area requirement (A_H) of the surfactants head group times the length (L_T) of the tail goup.

$$a_p = \frac{V_T}{A_T \cdot L_T} \tag{3.1}$$

Increasing values of the packing parameter predict a transition from spherical aggregates ($a_p \approx 0.33 - 0.50$), to cylindrical ones ($a_p \approx 0.50 - 0.80$) and eventually monolayer and bilayer formation.

The physical size of the micelles is very similar for all concentrations simulated above the cmc. The observation of similar physical size of the micelles is corroborated by the aggregation number distributions shown in figure 3.4 where we plot the "probability mass function"

$$M(N) = \left\langle \frac{N n_N}{\sum_{N=1}^{\infty} N n_N} \right\rangle, \tag{3.2}$$

where N is the aggregation number of a cluster, n_N is the number of clusters of size N in the system and $\langle \cdots \rangle$ denotes the canonical ensemble average. $M(N)$ can be interpreted as the probability of finding a surfactant molecule in a cluster of aggregation number N.

As can be inferred from the distributions in figure 3.4, the aggregation numbers fluctuate around a mean value $\overline{N} = 40$ and, although the distributions have been obtained at significantly different concentrations, they all are relatively narrow and strikingly similar (except in magnitude). This indicates that the system clearly prefers spherical micelles consisting of approximately 40 surfactant molecules at all concentrations shown in figure 3.4.

In the case of the $H_{10}T_5$ surfactant, longer head groups are expected to induce a smaller hydrophobic core due to the extra head area requirements [90]. The aggregation number for $H_{10}T_5$ around the CMC is $\overline{N}_{H_{10}T_5} = 30$

Figure 3.5 shows a typical micelle formed by the surfactants at $C \approx CMC$. It is clear that both surfactants (H_5T_5, $H_{10}T_5$) form spherical micelles in bulk solution at concentrations beyond the respective CMCs.

Since length scales between the various species in our system play an important role, we need to estimate the average diameter of a micelle. In order to do this, radial density profiles of bulk micelles are defined as [91]

$$\rho_r(r) = \left\langle \sum_{i=1}^{N^{mic}} \delta\left(r - r_i\right) \right\rangle, \tag{3.3}$$

where N^{mic} is the number of hydrophobic beads and r_i is the distance between bead i belonging to the micelle to the center-of-mass of the hydrophobic core. As commonly done [92] we define the micellar radius r^{mic}, by the inflection point in the radial density profile of the tails beads eq. (3.3) (Fig. 3.6). We find $r^{mic}_{H_5T_5} \approx 3.650$, and $r^{mic}_{H_{10}T_5} \approx 3.125$.

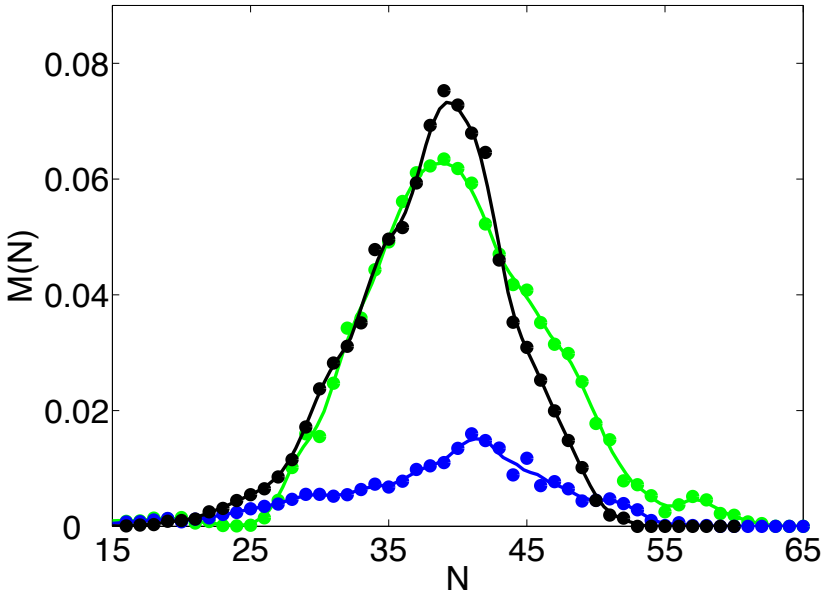

Figure 3.4: Cluster size distributions as probability mass functions for three surfactant concentrations $C = 6.70 \cdot 10^{-5}$ (blue), $C = 2.89 \cdot 10^{-4}$ (green), and $C = 8.12 \times 10^{-4}$ (black); labelled in Fig. 3.1 as C, B, and A, respectively. While the number of aggregates in the system increases with increasing concentration the mean aggregation number remains constant.[20]

The smaller core radius of $H_{10}T_5$ is consistent with the expected stronger steric repulsion between the longer head groups, requiring aggregates with a larger curvature. The mean cluster size of a H_5T_5 bulk micelle was found to be $\overline{N} = 40$, whereas for a $H_{10}T_5$ is $\overline{N} = 30$.

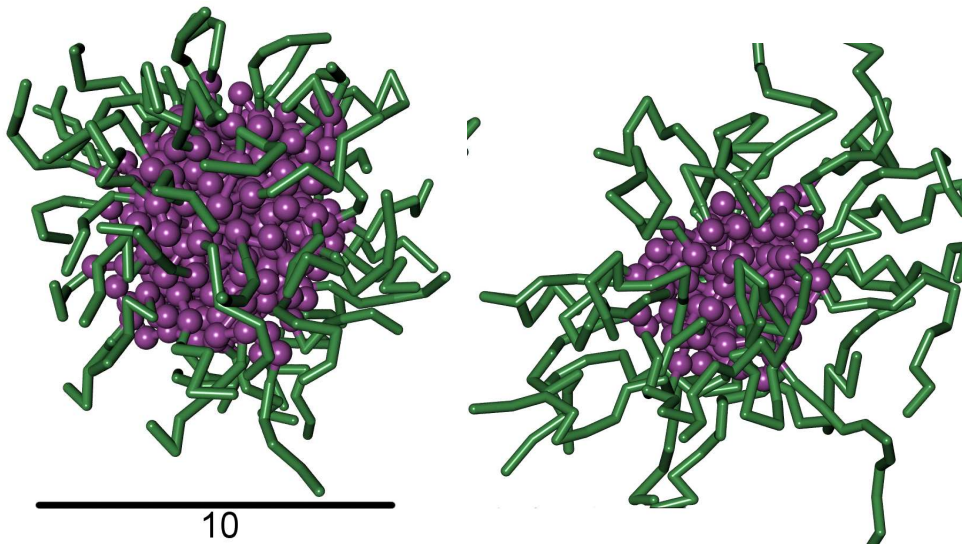

(a) (b)

Figure 3.5: Spherical micelles formed by the surfactants at $C \approx CMC$. (a) H_5T_5 and (b) $H_{10}T_5$. The longer head groups of $H_{10}T_5$ cause micellar cores to be smaller in size. Hydrophobic tails are shown in purple and hydrophilic heads are are shown in green. The scale bar below Fig. 3.5 (a) is 10σ and applied to both subfigures

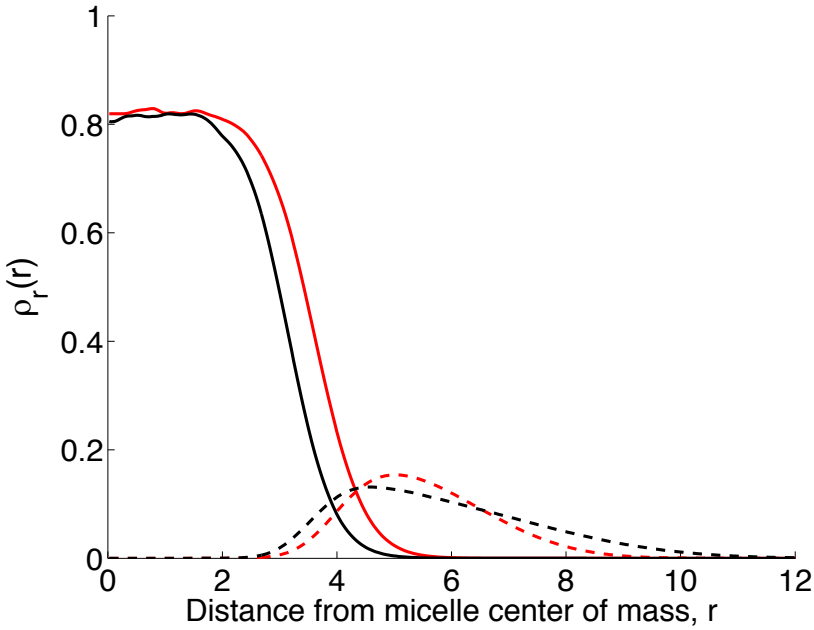

Figure 3.6: The structure of spherical bulk micelles of H_5T_5 (red) and $H_{10}T_5$ (black) at $C \approx CMC$ shown as the radial density of head (dashed lines) and tail beads (solid lines) as a function of the distances from the center of mass. $H_{10}T_5$, the surfactant with longer head group has a smaller core but a larger corona of head groups. Only micelles with sizes deviating by less than 25% from the mean aggregation number are considered.[65]

Part II

Adsorption studies

CHAPTER 4

The differences between surfactant adsorption on CNT and CNT bundles

This paper appeared as:

4.1 Introduction

Carbon nanotubes (CNT) and CNT materials enjoy widespread interest in research and increasing industrial attention. Their unique set of extraordinary properties enables a number of advanced applications ranging from the medical sciences[5–7], device manufacturing [16], acoustics engineering [17], electronics [18], to composite materials [19–21]. In these applications individual tubes are usually desired for functional[32] or economic reasons. Unfortunately, nanotubes tend to bundle due to van der Waals interactions and in solution also because of hydrophobic interactions. Since

tubes are very long a relatively large energy is required to separate a tube from a bundle making it very difficult to suspend or disperse the tubes[36].

To eliminate bundling and its consequences, a number of methods were devised. Some are based on chemical modification of the tubes which inevitably leads to undesired deterioration of the CNT properties [39, 40]. Alternatively, non-covalent functionalization through amphiphilic self-assembly can be used to stabilize CNTs in aqueous suspensions without affecting their properties [41, 42]. Initially, debundling is achieved by intense ultrasonication [45] after which surfactants adsorb on the CNTs and cover their surface [46]. The hydrophilic head groups of the surfactant molecules provide a steric (or electrostatic) repulsive barrier hindering or ideally preventing rebundling [47].

In the search for an optimized dispersion process, experimental studies have been conducted by various groups. The impact of surfactant concentration and the surfactants molecular structure on the number of isolated tubes in solution has been systematically investigated in a number of phenomenological studies e.g [48, 49]. However, as the interplay between surfactants and CNTs is complex and the number of potential control parameters is large, thorough undersanding and detailed insight is inevitable for successful optimization. To develop this understanding Matarredona et al.[50] and Utsumia et al.[51] measured adsorption isotherms of NaDDBS on CNTs using Raman spectroscopy. The isotherms reveal a two-step adsorption process where the first step was attributed to adsorption on bundles and the second to exfoliation of bundles (via sonication) and subsequent surfactant adsorption on individual tubes. The authors argue that at high concentrations a monolayer is formed on the tubes[50]. Similar observations were made by Xiao et al. [52] studying adsorption of CTAB on CNTs. In this case adsorption also follows a two-step mechanism.

In all these studies adsorption was not directly measured and the adsorbed structures could not be observed. It can also be difficult to determine the actual surfactant concentration, if it is not measured directly, due to surfactant adsorption on all kinds of interfaces in the system, including the CNTs, the container surfaces and liquid/gas interfaces. At concentrations below the cmc the proportion of adsorbed molecules in the system can be significant, as the cmc is usually low. An additional complication can be that the surface area of the container walls maybe of the same order-of-magnitude

as the total surface area of CNTs in the sample due to the usually low CNT concentrations.

Computer simulations do not suffer from these problems. Here the actual concentration, the adsorbed amount and the adsorbed structures are directly accessible. The potential of molecular simulations to study amphiphilic adsorption on CNTs is demonstrated by a number of recent studies. Wallace et al. [53, 54] used Coarse Grained Molecular Dynamics (CGMD) to investigate adsorption of DPPC lipids and two detergents, DHPC and LPC on CNTs. Depending on the type of amphiphile as well as the number of surfactant molecules in the simulation box they found a variety of adsorbed structures including randomly arranged surfactant molecules and encapsulation by spherical and cylindrical micelles. Shvartzman-Cohen et al. [55, 56] used CGMD to study adsorption of amphiphilic block-copolymers on CNTs and found adsorption with no specific ordering of the adsorbed molecules

Computer simulations have also been successfully used for a detailed analysis of the system at the atomic level. Tummala et al. [60] used fully atomistic MD to study adsorption of Na-dodecyl sulphate (SDS) molecules on SWCNTs from aqueous solution. They show that the morphology of adsorbed SDS structures is influenced by the tube diameter,its chirality and by the number of SDS molecules placed in the simulation box. A variation of structures has been observed when the number of molecules in the simulation box was increased. At low coverages SDS molecules form “rings” with the SDS molecules lying flat on the tube surfaces and parallel to the tube axis. High coverages favor the the formation of adsorbed micelles with disordered internal structure. Unfortunately, the high computational cost still prevents the large system sizes needed for concentration control.

Beyond dispersion, surfactant adsorption on CNT bundles is interesting from a more fundamental perspective. On one hand bundles have larger overall diameters than individual tubes but on the other hand the local curvature of its surfaces is that of the constituting tubes. Moreover, neighboring tubes form grooves where the adsorption energy is higher due to the ability of adsorbed molecules to interact with two surfaces. Simultaneously, the grooves create a degree of confinement. Thus, CNT bundles are heterogeneous adsorbents with a number of important length scales.

Heterogeneous surfaces are known to have a strong impact on adsorption isotherms and the morphologies of adsorbed phases [93–95]. The substrate can be chemically [96, 97] or geometrically structured [98, 99]. In many cases these heterogeneities lead to phase transitions on surfaces and in confinement and, thus, originate new phases with no bulk equivalent.

The length scales of the adsorbent heterogeneities are particularly important if the adsorbing molecules self-assemble and the length scales of the self-assembled aggregates and those of the adsorbent are of the same order-of-magnitude [100, 101]. In the case of amphiphilic self-assembly it has been found, that adsorbed and bulk aggregates have similar length scales [102–104]. Thus, as strong influence on the adsorption of amphiphilic molecules on CNTs and their bundles must be expected when the overall diameter or the heterogeneities reach the size of the self-assembled aggregates.

In this study we begin to elucidate surfactant adsorption on individual CNTs and on CNT bundles. We find major differences in the mechanisms of surfactant adsorption in CNT bundles compared to individual tubes. These differences originate form the heterogeneous surfaces of nanotube bundles and their larger diameter.

In our study we use DPD simulation of a mesoscale model which allows us to control the bulk surfactant concentration.

4.2 Model and Simulation

In this paper we employ computer simulations to study self-assembly of amphiphilic molecules on three different carbon nanotubes systems: An individual single wall carbon nanotube, a bundle consisting of three nanotubes and a bundle consisting of seven nanotubes (4.1). Our results might be extrapolated to larger symmetric bundles as their surface interaction potential is very similar to that of a bundle consisting of seven tubes. The only differece is that in larger bundles the potential will be marginally more attractive and longer ranged due to the larger number of tubes in the bundle.

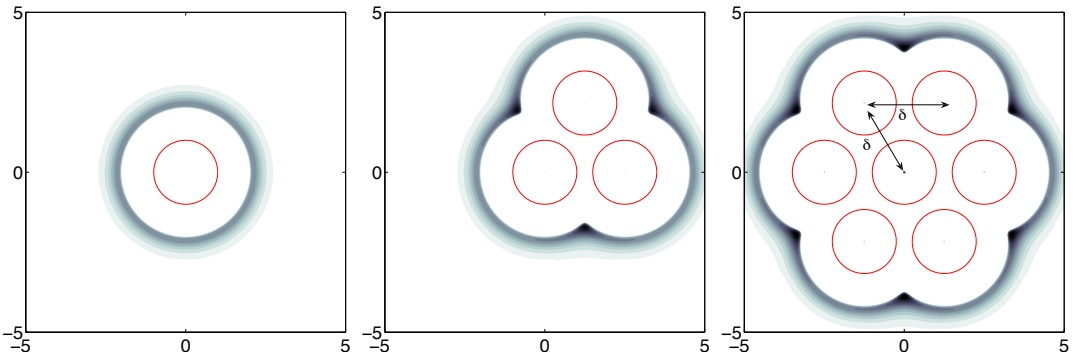

Figure 4.1: Attractive part of the CNT/hydrophobic-bead potential projected into a plane perpendicular to the tube axis. The distance between the axis of neighboting tubes in bundles is $\delta = 2.5$. Although the minimum of the potential in (b) and (c) is -5, the gray scale is linear from 0 to -3 to optically emphasize the grooves.

4.2.1 Model

In the simulations surfactant molecules are represented by a chain of beads (H_5T_5) consisting of a block of five hydrophilic head (H) beads and a block of five hydrophobic tail (T) beads while the solvent is considered implicitly. The implicit treatment of the solvent as well as the coarse-grained character of the surfactant beads causes the beads to interact via effective potentials. In the present case we employ a common empirical model, which we have used previously [20], where the interactions between a pair of hydrophobic beads is attractive, while all other bead/bead interactions are repulsive. Attractive interactions between beads i and j are represented by the pair potential $\phi(r_{ij})$ which is based on the force shifted Lennard-Jones (LJ)(12,6) potential

$$\phi_{\mathrm{LJ}}(r_{ij}) = 4\epsilon \left[\left(\frac{\sigma}{r_{ij}} \right)^{12} - \left(\frac{\sigma}{r_{ij}} \right)^{6} \right] \tag{4.1}$$

$$\phi(r_{ij}) = \begin{cases} \phi_{\mathrm{LJ}}(r_{ij}) - \phi'_{\mathrm{LJ}}(r_{\mathrm{cut}})(r_{ij} - r_{\mathrm{cut}}) - \phi^{\mathrm{LJ}}(r_{\mathrm{cut}}) & r_{ij} < r_{\mathrm{cut}} \\ 0 & r_{ij} \geq r_{\mathrm{cut}}, \end{cases} \tag{4.2}$$

where $\phi'_{\mathrm{LJ}}(r) = d\phi_{\mathrm{LJ}}(r)/dr$ and r_{cut} is the cut-off-radius. In eq.(4.1) $r_{ij} = \|\mathbf{r}_{ij}\|$, $\mathbf{r}_{ij} = \mathbf{r}_j - \mathbf{r}_i$ and $\mathbf{r}_i$ and $\mathbf{r}_j$ are the positions of i and j, respectively; ϵ is the well depth and σ the length parameter of the LJ potential. Repulsive interactions are represented by the WCA potential, given by eq.(4.2) with $r_{\mathrm{cut}} = 2^{1/6}$. For simplicity, these interactions are

Surfactants					
T beads	=	5	H beads	=	5
ϵ	=	1.0	σ	=	1.0
ϵ_{bond}	=	4.0	σ_{bond}	=	1.2
Nanotubes					
r_{CNT}	=	1.0	ϵ_{CNT}	=	2.5
δ	=	2.5			
Simulation					
T	=	0.7	Δt	=	0.005
attractive: r_{cut}	=	2.5	repulsive: r_{cut}	=	$2^{1/6}$
non-conservative: r_{cut}	=	2.5	ξ	=	1.0
production	=	$0.5 \cdot 10^8 \Delta t$	equilibration	=	$(1\ up\ to\ 2) \cdot 10^8 \Delta t$

Table 4.1: Model and simulation parameters in reduced units: δ is the distance between neighbooring nanotubes.

assumed to be present between all pairs of beads regardless whether they are bonded or not. In addition, two beads k and l which are nearest neighbors in a single surfactant chain interact via the harmonic bond potential, $\phi_{\text{bond}}(r_{kl}) = \epsilon_{\text{bond}}(r_{kl} - r_{\text{bond}})^2$, where ϵ_{bond} is the depth of the potential well and r_{bond} the bond length.

The length scale of the coarse-grained surfactant beads renders the atomic structure of a nanotubes (essentially) irrelevant, enabling us to model the nanotubes as smooth cylinders. They interact with the hydrophobic surfactant beads via the force shifted Lennard-Jones (12,6) potential in eq.(4.2) which is also shifted to the surface of the nanotubes

$$\phi_{\text{CNT}}(r_i) = \frac{\epsilon_{\text{CNT}}}{\epsilon}\phi(r_i - r_{\text{CNT}}) \tag{4.3}$$

where r_i is the shortest distance between bead i and the nanotube axis (for the formula see e.g. Ref.[66]) and r_{CNT} is the radius of the nanotube. Interactions of the hydrophilic head beads with the nanotubes are modeled using the WCA potential, i.e. $\phi_{\text{CNT}}(r_i)$ with $r_{\text{cut}} = 2^{1/6}$. All potential parameters can be found in table I.

In 4.1 the attractive part of the CNT/hydrophobic bead potential is plotted to visualize the heterogeneity of the potentials of the bundles. Clearly visible are sites with large interaction potential along grooves formed by two neighbouring tubes. The distance between these groves is larger in the triplet compared to the septet. We note that, because of our choice of $r_{\text{cut}} = 2.5$, groove sites in the triplet and the septet are identical.

Simulation

We investigate the system in the canonical ensemble using the dissipative particle dynamics (DPD) method [79]. In DPD any two particles i and j interact via the pairwise force $F_{ij} = F_{ij}^C + F_{ij}^R + F_{ij}^D$, where F_{ij}^C, F_{ij}^R and F_{ij}^D are the conservative, the random and the dissipative force, respectively.

The conservative force acts along the line connecting i and j , given by $\widehat{\mathbf{r}}_{ij} = \mathbf{r}_{ij}/\|\mathbf{r}_{ij}\|$, and depends only on the distance r_{ij} between i and j. It is given by the first derivative of the interaction potentials discussed above.

The random force

$$F_{ij}^R = \begin{cases} -\xi\omega^R(r_{ij})\theta_{ij}\widehat{\mathbf{r}}_{ij} & r_{ij} \leq r_{\text{cut}} \\ 0 & r_{ij} > r_{\text{cut}} \end{cases} \tag{4.4}$$

represents forces from the (rapidly moving) degrees of freedom which have been coarse-grained out, such as collisions with solvent particles leading to Brownian motion of solutes. In DPD these forces are assumed to be pairwise and random in strength. In eq.(4.4) ξ is a parameter determining the strength of the random force, whereas $\omega^R(r_{ij})$ is a weight function characterizing its distance dependence and θ_{ij} is a random variable with limits -1 and 1, and zero mean (see [105] for reasoning to use uniform random numbers and [78] for the random number generator we are using for our long trajectories). As the conservative force does, the random force acts along the line connecting i and j.

The dissipative force (or drag force)

$$F_{ij}^D = \begin{cases} -\gamma\omega^D(r_{ij})(\widehat{\mathbf{r}}_{ij} \cdot \mathbf{v}_{ij})\widehat{\mathbf{r}}_{ij} & r_{ij} < r_{\text{cut}} \\ 0 & r_{ij} > r_{\text{cut}} \end{cases} \tag{4.5}$$

represents the viscous drag mediated by degrees of freedom which have been coarse-grained out. In eq.(4.5) γ is the strength parameter. $\omega^D(r_{ij}) = \left[\omega^R(r_{ij})\right]^2$ is the weight function of the dissipative force. Here we use the weight functions originally published in Ref. [79]

$$\omega^D(r_{ij}) = \begin{cases} (1 - r_{ij}/r_{\text{cut}})^2 & r_{ij} \leq r_{\text{cut}} \\ 0 & r_{ij} > r_{\text{cut}}, \end{cases} \tag{4.6}$$

where we have chosen $\omega^D(r)$ to be of the same range as the attractive conservative

force.

The simulation box is rectangular and periodic boundary conditions are applied in all three dimensions. CNTs are placed in the box such that their axis are parallel to the long dimension of the box. This allows the determination of the bulk surfactant concentration in regions which are more than 25σ away from the tube surface and are considered bulk-like. Accessibility of the actual bulk surfactant concentration is key to our study and is not easily achieved experimentally. To maintain the surfactant concentration within 5% of its target value, surfactant molecules have been created and deleted in the bulk-like region during the initial part of the equilibration period [20].

Definition of Important Quantities

Throughout the paper we use reduced quantities: units of length are given with respect to the LJ length parameter σ, the energy scale is given in units of the well depth of the bead/bead LJ interaction ϵ, the temperature scale is given in terms of ϵ/k_B where k_B is the Boltzmann constant, and time is represented in units of $\sqrt{m\sigma^2/\epsilon}$, where m is the mass of a bead. Concentrations C are defined as molecular number densities and given in units of $1/\sigma^3$.

For normalization of the adsorbed amount, computation of the surface area available for adsorption is necessary. Here we define the surface area A as the legth of the tubes multiplied by the arclength ℓ of the contour line corresponding to the potential isovalue of -2.5 (4.1). In the case of an individual tube this is the contour of the potential minimum with $\ell_1 = 2\pi(1 + 2^{1/6}) = 13.34$. For the bundles we numerically follow the outer contour which is very close to the potential minimum and obtain $\ell_3 = 18.02$ and $\ell_7 = 27.01$.

Two dimensional density maps have been calculated for the hydrophobic tails. These have been generated by a projection of the coordinates of the hydrophobic beads along the nanotube axis onto a square lattice of granularity 0.1. Densities are averaged over the equilibrium part of the simulation by taking samples every 5000 time steps.

The cluster size distribution for adsorbed surfactant clusters is defined here as the

(canonical ensemble average of the) probability mass function

$$P(N) = \left\langle \frac{N \cdot n_N}{\sum_{N=1}^{\infty} N \cdot n_N} \right\rangle, \tag{4.7}$$

where n_N is the instantaneous number of adsorbed clusters of size N. and $\langle \cdots \rangle$ denotes the canonical enseble average.

4.3 Results and Discussion

We investigate surfactant adsorption on individual carbon nanotubes and small bundles consisting of 3 and 7 nanotubes. The model surfactant used in this study has a CMC value of $5.2 \cdot 10^{-5}$ and forms spherical micelles of approximately 41 molecules in bulk solution[20]. The diameter of the hydrophobic core of the micelles was estimated at approximately 5 [20].

4.3.1 Adsorption of surfactants on individual carbon nanotubes

Surfactant adsorption on an individual carbon nanotube was studied in a previous publication [46]. Since this case represents an important reference for adsorption on bundles we review key findings and supplement them with relevant additional information.

At low surfactant concentrations $C \lesssim 0.6 \cdot 10^{-5}$, well below the CMC, the areal density of adsorbed surfactant molecules $\frac{N_{\text{ads}}}{A}$ increases linearly with the surfactant concentration (4.2(b)). In this regime only very few molecules are adsorbed. Thus, they only very rarely interact with each other creating an ideal gas type system. Such as system follows Henry's law

$$N_{\text{ads}} = CA \left\langle e^{-\frac{f}{k_B T}} \right\rangle \tag{4.8}$$

where f is the free energy of adsorption per molecule. As all molecules are identical $f = \text{const.}$ leading to the observed linear regime.

As the bulk concentration increases beyond $C \approx 0.8 \cdot 10^{-5}$ the adsorbed amount increases superlinearly. This is a sign of cooperative effects contributing to the adsorption mechanism. Upon adsorption, molecules interact with each other and form small

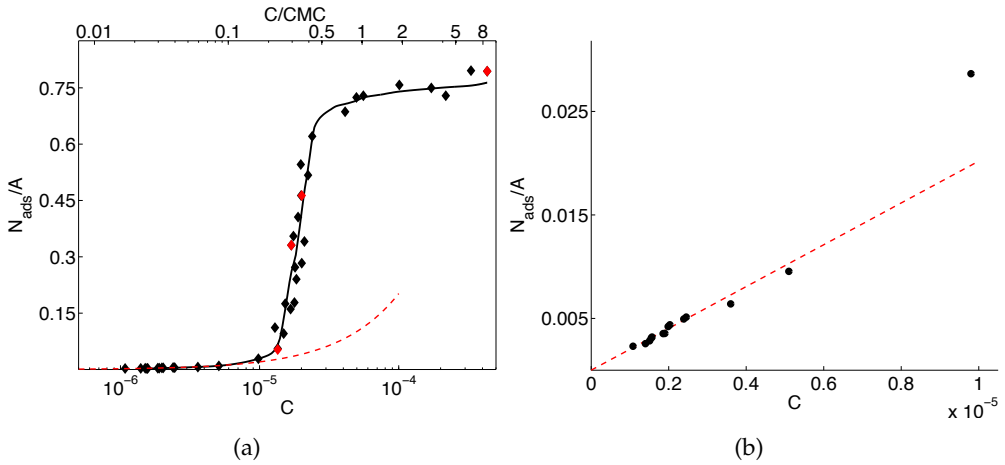

Figure 4.2: Adsorption isotherms as the areal density of adsorbed surfactant molecules $\frac{N_{\text{ads}}}{A}$ versus (bulk) concentration C: (a) for the entire concentration range and (b) for the linear regime at small concentrations. The solid line in part (a) provides a guide to the eye while the dashed line is a linear fit to data points at $C < 0.6 \cdot 10^{-5}$. Red symbols represent points for which snapshots are shown in 4.3. Data taken from [46].

clusters. The energy of these intermolecular interactions contributes to the free energy of adsorption, leading to the observed superlinear increase in the adsorbed amount. The loss in entropy due to clustering is much harder to quantify but does not appear to dominate adsorption in the present case. The presence of small adsorbed clusters is evident in the simulation snapshot in figure 4.3(a) taken at $C = 1.35 \cdot 10^{-5}$ and in the respective cluster size distribution in figure 4.4(a). Clusters in this regime have no preferred size, thus, $P_1(N)$ decreases exponentially fast and clusters grow in size with increasing concentration.

At a surfactant concentration of $C = 1.49 \cdot 10^{-5}$ a local maximum at $N \approx 13$ is visible in the cluster size distribution in 4.4 (a). Such a maximum is evidence for the formation of clusters of a preferred size and, thus, for surface aggregation. The smallest concentration where surface aggregation occurs is called the Critical Surface Aggregation Concentration (CSAC). Here we estimate $C_{\text{CSAC}} = 1.50 \cdot 10^{-5} \approx \frac{1}{3} C_{\text{CMC}}$. As the concentration increases from the CSAC to approximately $30 C_{\text{CSAC}} \approx 10 C_{\text{CMC}}$ adsorbed aggregates grow from $N \approx 13$ to $N \approx 55$ while the aggregation number of bulk micelles is constant at approximately 41 in the concentration range between C_{CMC} and $10 C_{\text{CMC}}$ (4.3, 4.4)[20]. It is interesting to note that we did not observe any change in the number of adsorbed aggregates at concentrations beyond the CSAC.

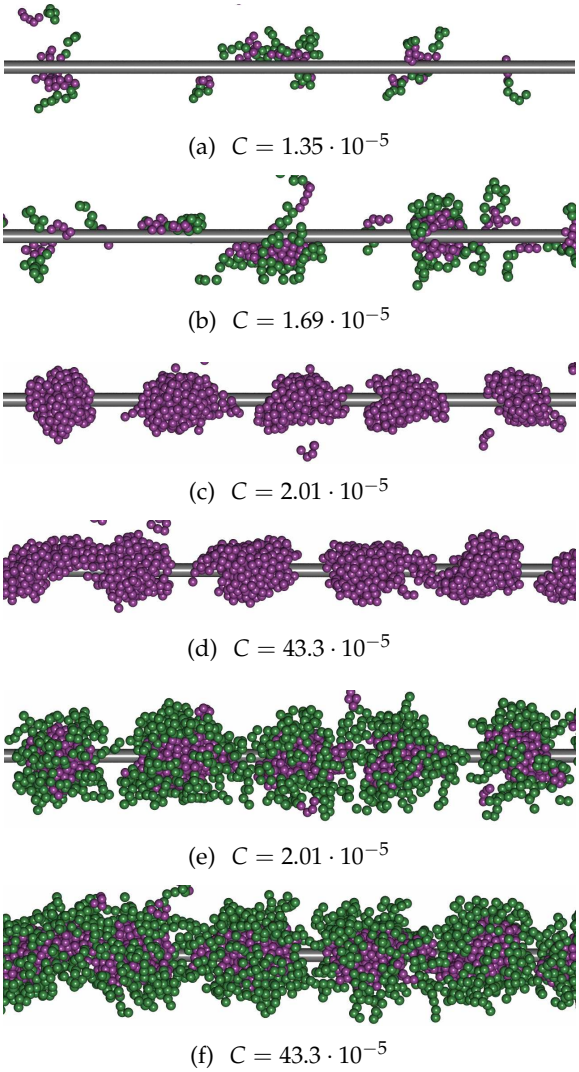

(a) $C = 1.35 \cdot 10^{-5}$

(b) $C = 1.69 \cdot 10^{-5}$

(c) $C = 2.01 \cdot 10^{-5}$

(d) $C = 43.3 \cdot 10^{-5}$

(e) $C = 2.01 \cdot 10^{-5}$

(f) $C = 43.3 \cdot 10^{-5}$

Figure 4.3: Simulation snapshots at different bulk concentrations as indicated in the figure and highlighted in 4.2(a): (a), (b), (e),(f) depicting the hydrophilic surfactant head beads in green and the hydrophobic tail beads in purple and (c), (d) showing only the hydrophobic tails.

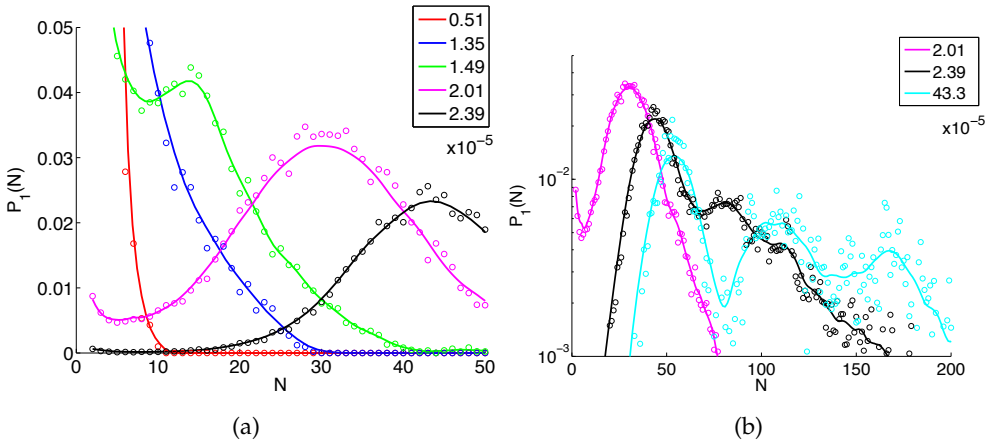

Figure 4.4: Cluster Size Distributions $P_1(N)$ for surfactant adsorption on an individual CNT at various concentrations as indicated in the figure: (a) linear N-scale and (b) logarithmic N-scale to emphasize the tails at large N. Data for $C/10^{-5} = 0.51, 1.35, 1.49, 2.01, 43.3$ taken from [46].

Associated with surface aggregation is a steep increase in the adsorbed amount (4.2). This increase is caused by growth of the adsorbed aggregates. As the bulk concentration increases to $C \approx 2.39 \cdot 10^{-5}$, the aggregate size increases quickly up to approximately 45 which is very similar to the aggregation number of bulk micelles. Any further increase in the concentration leads to only a slight increase in the average aggregate size (4.4(b)). Simultaneously, the adsorbed amount levels-off. (Observe the logarithmic concentration scale in 4.2 (a)). Thus, adsorption is nearly complete at a concentration significantly smaller than the CMC, i.e. around $C \approx \frac{1}{2}C_{\mathrm{CMC}}$.

The shape of adsorbed aggregates just after the CMC is close to that of hemi-micelles, i.e. aggregates attach to the side of the tubes rather than engulfing it concentrically (4.3(b) and 4.5 (a)-(c)). After the steep part of the adsorption isotherm at $C \gtrsim \frac{1}{2}C_{CMC}$ adsorbed aggregates enclose the nanotube concentrically but are slightly elongated along the tubes (4.5 (d)-(f)). The diameter of the hydrophobic core of these micelles $d \approx 8$ is somewhat larger that that of a bulk micelle $d \approx 5$. However, the micelles do not seem to be perturbed too much by the presence of the tube. Thus, they remain intact also in the adsorbed state. Their diameter is difficult to judge from snapshots but can be estimated to $d \approx 5$ to 6 with the CNT replacing the "missing" half. As well as the full micelles, also the hemimicelles are elongated along the tube. These observations indicate that the morphology of the absorbed aggregates is a result of maximizing the

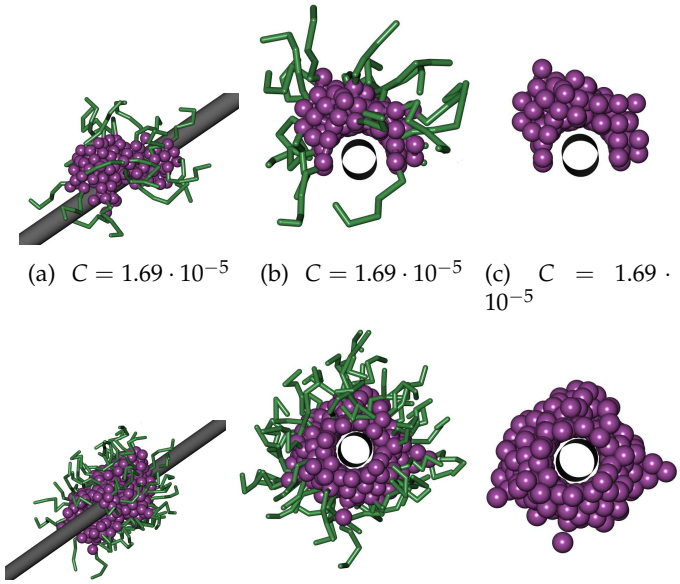

(a) $C = 1.69 \cdot 10^{-5}$ (b) $C = 1.69 \cdot 10^{-5}$ (c) $C = 1.69 \cdot 10^{-5}$

(d) $C = 17.15 \cdot 10^{-5}$ (e) $C = 17.15 \cdot 10^{-5}$ (f) $C = 17.15 \cdot 10^{-5}$

Figure 4.5: Simulation snapshots at two concentrations: upper panel $C = 1.69 \cdot 10^{-5}$ presenting a hemimicelle and lower panel $C = 17.15 \cdot 10^{-5}$ presenting a full micelle. Hydrophilic surfactant head groups are shown in green and hydrophobic tails in purple. In parts (c) and (f) head groups are omitted for clarity.

interaction with the CNT while simultaneously maintaining their preferred curvature.

At concentrations beyond $C \approx 2 \cdot 10^{-5}$ cluster size distributions have a tail at large cluster sizes which is caused by temporary connection between two or more clusters. At the highest concentrations this tail shows maxima at integer multiples of the position of the maximum of the first peak implying the connection of two or more adsorbed aggregates(4.4(b) and (4.3(d)). This also implies that at concentrations below $C \approx 2 \cdot 10^{-5}$ adsorbed clusters are well separated along the tubes (4.3(c)).

4.3.2 Surfactant Adsorption on CNT Bundles

On first sight, it is obvious that the isotherms for surfactant adsorption on bundles are very different compared to the isotherm we have obtained for an individual tube (4.6(a)). The most significant difference is the lower slope in the steep part of the adsorption isotherms of the bundles. While we have already shown that adsorption of individual small diameter CNTs is cooperative and dominated by aggregation, the isotherms for the bundles resemble Langmuir-type isotherms, suggesting a different adsorption mechanism.

This is not entirely surprising. Above we have seen that adsorbed micelles are not very much bigger than bulk micelles, which is consistent with several reports in the literature [20, 53, 106]. Since the over all diameter of the bundles is much larger than that of a bulk micelle, adsorption of concentric micelles on the CNT bundles is not possible. Thus, adsorption must follow a different mechanism.

Additionally, surfactant adsorption on the bundles starts at much lower concentrations and the adsorbed amount levels off at a slightly lower concentration compared to individual tubes . Interestingly, at the highest concentrations, after the "levelling-off" point, the areal density of surfactant molecules adsorbed on the bundles is always slightly lower compared to the single tube case.

The most important difference between bundles and individual tubes is that the outer surface of bundles is heterogeneous because bundles consists of several tubes. Most significantly, their surface has grooves where surfactant beads can interact with two tubes simultaneously (4.1). It is important to notice that the grooves in the case of the

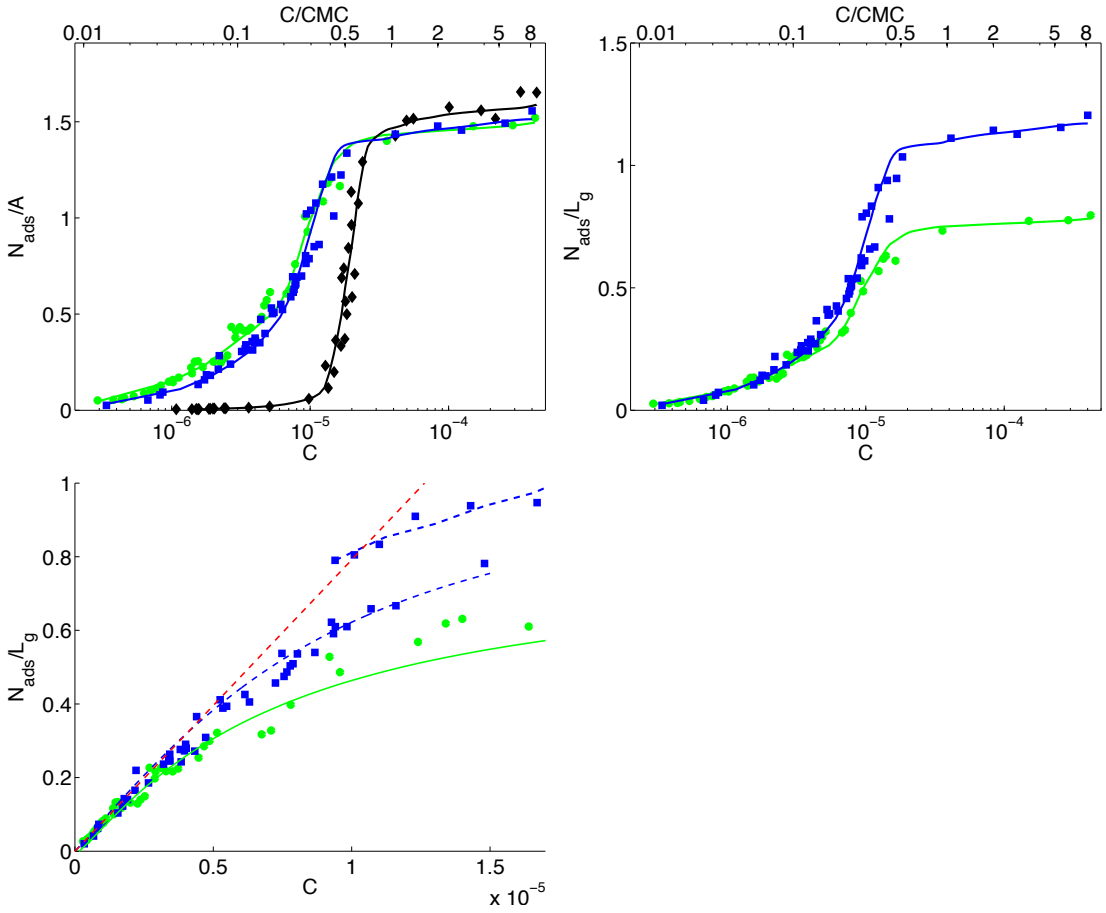

Figure 4.6: Adsorption isotherms as: (a) the areal density of adsorbed surfactant molecules $\frac{N_{ads}}{A}$ versus concentration and (b),(c) number of adsorbed surfactant molecules normalized by the total length of grooves $\frac{N_{ads}}{L_g}$; for adsorption on a single tube (black ♦), on a triplet (blue, ■) and on a septet (green, •). Solid lines are guides to the eye. Dashed blue lines in (c) indicate adsorption/desoption branches. Adsorption on bundles is very different compared to adsorption on single tubes. Visible is also the transition from groove dominated adsorption ($C \lesssim 0.3 \cdot 10^{-5}$) to surface dominated adsorption ($C \gtrsim 1.0 \cdot 10^{-5}$).

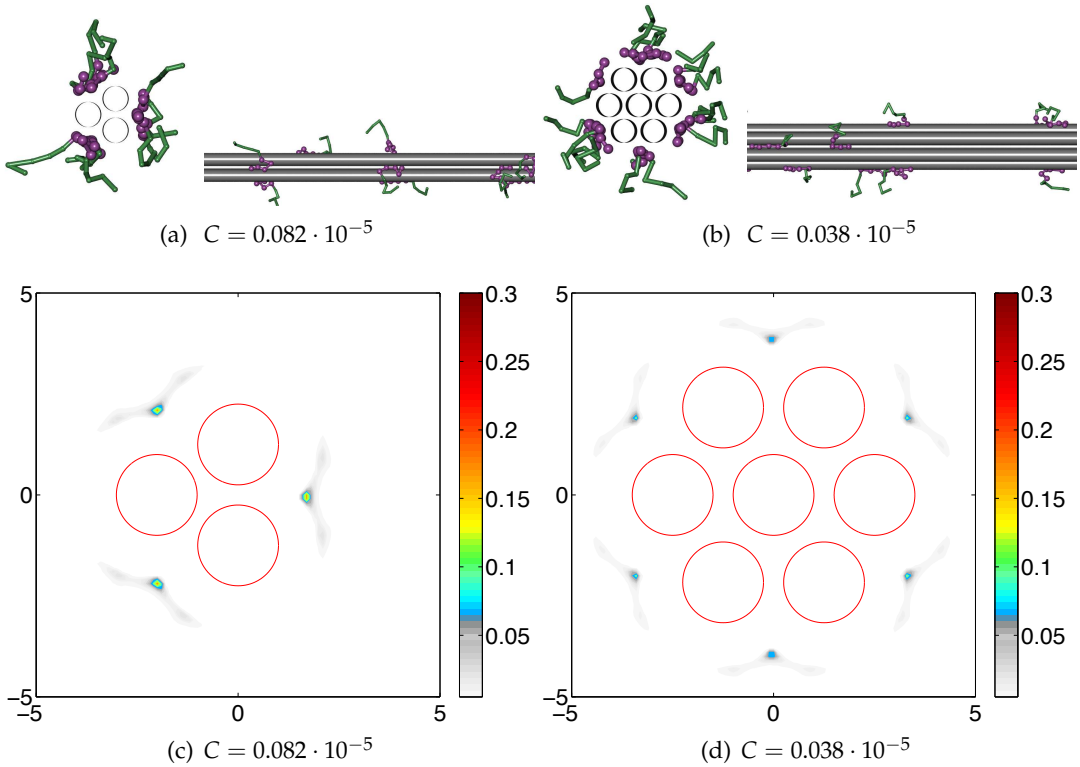

(a) $C = 0.082 \cdot 10^{-5}$ (b) $C = 0.038 \cdot 10^{-5}$

(c) $C = 0.082 \cdot 10^{-5}$ (d) $C = 0.038 \cdot 10^{-5}$

Figure 4.7: Simulation snapshots and corresponding local densities of the hydrophobic tail beads of adsorbed surfactant molecules for systems in the Henry's law regime: (a),(c) triplet at $C = 0.082 \cdot 10^{-5}$ and (b),(d) septet at $C = 0.038 \cdot 10^{-5}$. The snapshots depict hydrophilic surfactant head groups in green and the hydrophobic tails in purple. In both cases individual molecules are adsorbed in the grooves.

triplet and the septet and in fact, all other bundles, are almost identical. The differences are caused by tubes which are not directly constituting the groove. These tubes are relatively far away and only render the total bundle/adsorbent interaction sightly more attractive and longer ranged. In our model this minor difference is ignored, such that all grooves are identical.

The similarity of the grooves suggests to represent the isotherms as the number of adsorbed surfactant molecules normalized by the total groove length. Thus, in 4.6(b) the number of adsorbed surfactant molecules per unit length of groove $\frac{N_{\text{ads}}}{L_{\text{g}}}$ is show. As expected, we observe perfect overlap of the isotherms at low concentrations.

Magnification of this low concentration region reveals a linear regime for concentrations $C \lesssim 0.30 \cdot 10^{-5}$. This is expected as adsorption in the grooves should initially follow Henry's law (4.8) with a lower (negative) free energy of adsorption f compared to individual tubes. It is important to note that adsorption is accompanied by a significant loss in internal and translational entropy. This loss is even larger in the case of the one-dimensional grooves. However, the larger slope of the adsorption isotherms and, equivalently, the larger adsorbed amount at the lowest concentrations in the case of the bundles compared to the individual tube in 4.6(a), suggests, that the stronger interaction in the grooves is not fully compensated by the higher entropy loss.

The domination of the adsorbed phase by individual molecules in this regime is evident in the respective clusters size distributions in Supplemental Information (SI) . The local densities shown in 4.7(c) and (d) clearly indicate that the most probable location of beads of these adsorbed molecules is in the grooves. It is also interesting to inspect the snapshots in 4.7(a) and (b). While they corroborate the previous results, they also indicate that surfactant molecules do not lay flat in the grooves most of the time as significant densities are observed in the outer groove areas, indicating the significance of configurational entropy for our model molecules.

At concentrations above the Henry's law regime adsorption isotherms fall below the linear limit. This sublinear behavior is very different compared to the superlinear increase observed for individual tubes. A Sublinear increase of the adsorbed amount is typical for non-cooperative Langmuir type adsorption. In the Langmuir case the sublinearity results from the increasingly larger entropy loss of the entire adsorbed phase

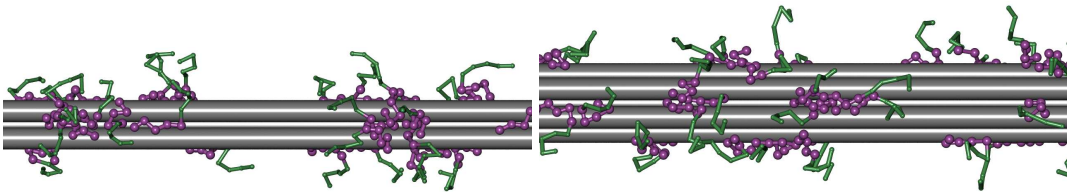

(a) Triplet $C = 0.21 \cdot 10^{-5}$ (b) Septet $C = 0.20 \cdot 10^{-5}$

Figure 4.8: Simulation snapshots to show small clusters adsorbed on the grooves: (a) triplet at $C = 0.21 \cdot 10^{-5}$ and (b) septet at $C = 0.20 \cdot 10^{-5}$. Hydrophilic surfactant head groups are shown in green and hydrophobic tails in purple. Clusters are centered at the grooves but spread out onto the nanotube surfaces to some extent.

upon adsorption of additional molecules at progressively higher surface coverages.

Hypothetizing Langmuir adsorption one expects adsorption of individual molecules. Contrarily, cluster size distributions $P_7(N)$ (Figure SI.1(c),(d)) indicate that the adsorbed phase is dominated by small (random) clusters. However, the additional intermolecular interactions in these clusters should lead to some level of cooperativity and superlinear adsorption as in the case of individual tubes.

The snapshot in 4.8(b) indicates that clusters are located along the grooves and stretched in the direction of the grooves. Otherwise the clusters are "blobby" in structure and reach out onto the tube surface where surfactant beads interact with only one tube. This becomes even more apparent in the local densities in 4.9(b). As a consequence the average adsorption energy per molecule reduces. The sublinear increase in the adsorbed amount suggests that this reduction is not fully compensated by the intermolecular interactions within the clusters.

In the case of the triplet of tubes adsorption follows a similar trend. Although clusters reach out onto the tubes, adsorption is still dominated by the grooves, i.e. there is no independent adsorption outside the grooves. Thus the adsorbed amount still scales with the groove length.

The triplet of tubes follows a similar tendency. Interestingly, however, cluster size distributions indicate a slight tendency for aggregation (Figure SI.1 (a),(b) $P_3(N)$ for $C \gtrsim 0.22 \cdot 10^{-5}$). These aggregates are very small and grow with concentration. As all other clusters, aggregates are located along the grooves and reach out onto the tube

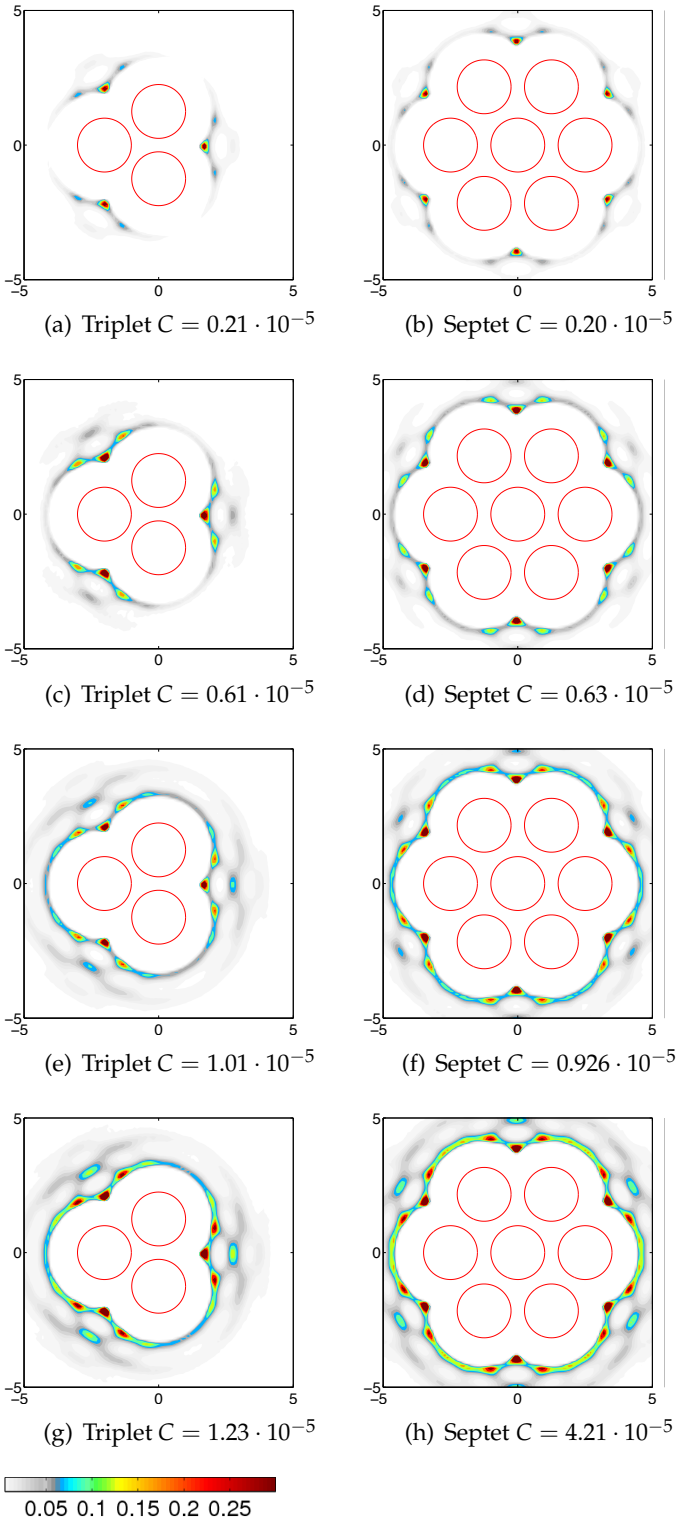

(a) Triplet $C = 0.21 \cdot 10^{-5}$ (b) Septet $C = 0.20 \cdot 10^{-5}$

(c) Triplet $C = 0.61 \cdot 10^{-5}$ (d) Septet $C = 0.63 \cdot 10^{-5}$

(e) Triplet $C = 1.01 \cdot 10^{-5}$ (f) Septet $C = 0.926 \cdot 10^{-5}$

(g) Triplet $C = 1.23 \cdot 10^{-5}$ (h) Septet $C = 4.21 \cdot 10^{-5}$

Figure 4.9: Local densities of hydrophobic tail beads of adsorbed surfactant molecules for the triplet and the septet at various concentrations as indicated in the figure. Clearly visible is the formation of "2nd order channels" in (c),(d) as well as beginning adsorption between the grooves. Filling of the gap between the grooves appears to be discontinuous. Local densities in (d)/(f) and (c)/(e) illustrate the two states, although the shown densities do not belog to corresponding states.

surfaces (4.8(a), 4.9(a)). Although noticeable even at high concentrations, aggregation remains a minor effect and does not appear to influence the adsorbed amount significantly.

At $C \approx 0.3 \cdot 10^{-5}$ $\frac{N_{\text{ads}}}{L_{\text{g}}}$ of the triplet and the septet of tubes shown in 4.6(b),(c) start to deviate from each other indicating that adsorption is no longer dominated by the grooves. Comparing the local densities in 4.9(c) and (d) with the respective density plots at lower concentrations shown in 4.9(a) and (b), one notices that surfactant molecules now adsorb everywhere on the bundle surface. As the surface area per groove is larger in the triplet compared to the septet and interaction potentials along the tube surfaces are the same in both cases, the triplet isotherm in 4.6(b) should lay above that of the septet as it does.

In the region above the Henry's law regime up to the levelling-off point data points appear to scatter rather significantly, although the statistical errors are very small. For all points in this region the 99% confidence interval is smaller than 1% because of the long production runs. However, some scattering is expected in this region since on one hand the adsorbed amount changes strongly with concentration and on the other there are usually many more molecules adsorbed compared to the number of molecules in the bulk. Bulk sizes are limited to keep the computational cost at bay. As a consequence, a fluctuation in the bulk concentration might trigger adsorption or desorption of many molecules which can change the concentration more than the initial fluctuation. Thus one has to balance between system stability and computational cost.

However, in some regions, e.g. at $C \approx 1 \cdot 10^{-5}$ for the triplet, "scattering" is too large and systematic to originate from computational errors. Closer inspection of 4.6(c) reveals two distinct branches in the adsorption isotherm. Such a behavior is typical for bistability and hysteresis, found for example near discontinuous phase transitions. Comparing the density plots in 4.9(e) and (g) reveals that the difference between the lower and the upper branch of the isotherms is filling of the gap between the structures adsorbed along the grooves. Detailed analysis of similar systems has proven that such "filling" can indeed be first order in the case of simple fluids [107].

Density plots at $C = 0.63 \cdot 10^{-5}$ and $C = 0.92 \cdot 10^{-5}$ presented in 4.9(d) and (f) and the splitting of the adsorption isotherm into two branches indicate the existence of the

same type of transition in the case of the septet around $C \approx 0.7 \cdot 10^{-5}$. It is expected that on septets this transition occurs at a lower concentration compared to triples as on septets the gap between grooves on septets is smaller.

At even lower concentrations our results hint the existence of additional bistabilities which resemble of the wetting transitions in simpler systems; e.g. at $C \approx 0.4 \cdot 10^{-5}$ the second order maxima in the groves seem to be filled which has also been observed in numerous other systems [108, 109]. As detailed investigation of these effects is beyond the scope of this manuscript we present some additional local density plots in the supplemental information. In general, all these seemingly cooperative transition are only minor effects and do not significantly affect the general adsorption behavior.

After filling of the surfaces, cluster size distributions indicate complete connection of the adsorbed phase (Figure SI.1). Although the adsorbed phase is fully connected, molecules are not completely evenly distributed and snapshots (not shown) show that the adsorbed layer has many defects. However, density plots at high concentrations shown in 4.9(g) and (h) indicate that surfactant molecules are adsorbed everywhere on the surface. In this regime the grooves should play only a minor role and ,as expected, adsorption scales with the surface area (4.6(a)). The leveling-off is not as sharp as for individual tubes which is expected due to the marginal cooperativity. The absence of aggregation could also be the reason why adsorption on the bundles levels off at slightly lower areal densities.

4.4 Conclusions

In this manuscript we study adsorption of surfactant molecules on small-diameter CNTs and their bundles using a coarse-grained model in DPD simulations.

Our results demonstrate major differences between adsorption on individual tubes and bundles. Adsorption on individual small-diameter tubes is dominated by aggregation. Adsorbed micelles are formed which resemble spherical bulk micelles. When fully developed, micelles engulf the tube concentrically and are slightly elongated along the tube axis. Most of the adsorption occurs quickly after the critical surface aggregation concentration trough growth of the adsorbed micelles.

Adsorption on the bundles is largely non-cooperative and, consequently, isotherms have a lower slope in the steep part. On the other hand, adsorption on bundles starts at much lower concentration due to the grooves along the surface of the bundles where surfactant molecules can simultaneously interact with two tubes. These grooves are almost identical for all bundles and dominate adsorption at low coverages. At higher concentration adsorption is progressively dominated by the total surface area of the bundle.

As a consequence of these differences in the adsorption mechanisms a crossover point exists where the areal density of surfactant molecules adsorbed on individual tubes exceeds that of the bundles.

4.5 Supplemental Information

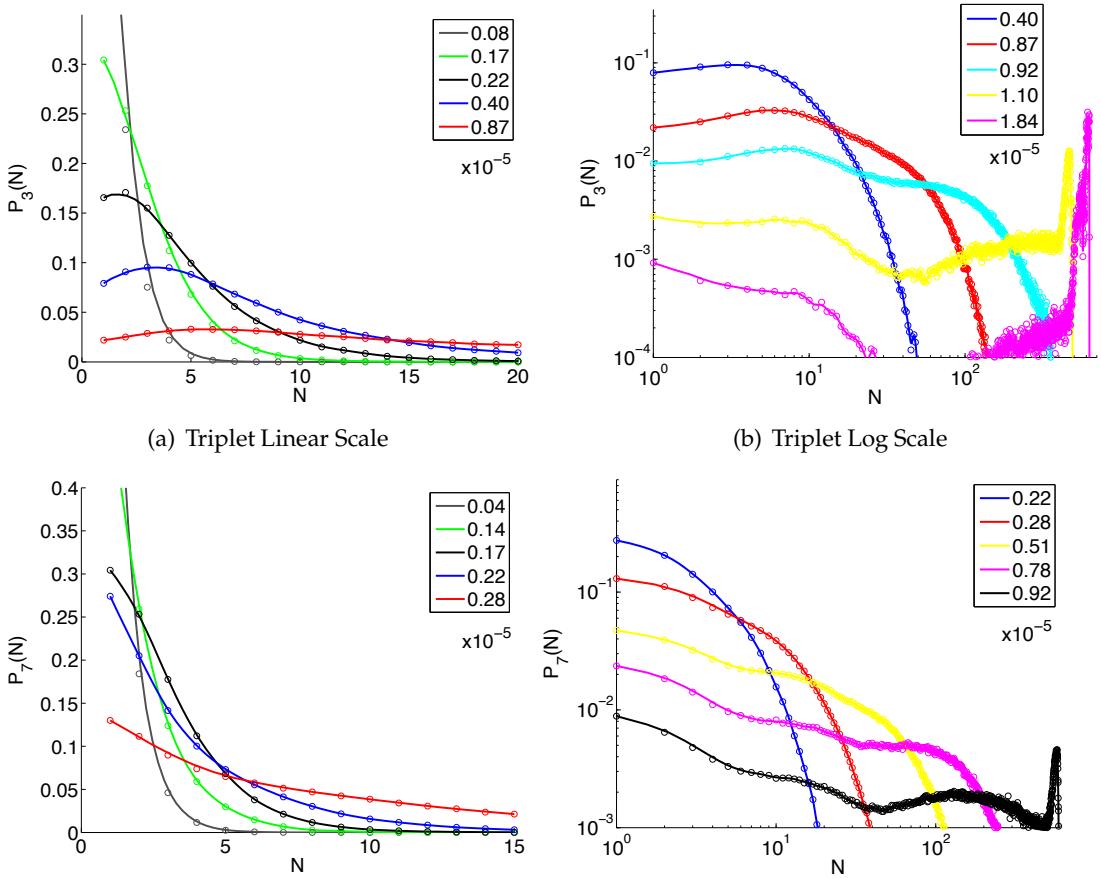

(a) Triplet Linear Scale

(b) Triplet Log Scale

(c) Septet Linear Scale

(d) Septet Log Scale

Figure 4.10: Cluster Size Distributions as the probability mass function versus aggregation number $P(N)$ for: (a),(b) the triplet of tubes and (c),(d) the septet at various concentrations as indicated in the figures. Surfactant molecules adsorbed on the triplet of tubes form small self-assembled aggregates at not too low concentrations as indicated by the maximum in the distributions. With increasing concentartion clusters and aggregates grow in size and form more and more connections to other clusters and aggregates until at the highest concentrations the adsorbed phase is almost completely connected.

CHAPTER 5

Directed Self-assembly on CNT junctions

5.1 Introduction

Because of their exceptional set of properties carbon nanotubes (CNTs) have been proposed for a large range of applications ranging from high-strength materials usefull e.g. as bone scaffolds to highly efficient and flexible field emitters and nanoelectronics. Although CNTs are central to all these applications, usually they are accompanied by other materials for structural or functional reasons.

For example, although individual nanotubes are strong CNT materials are typically much weaker [22–25]. The weakest materials are those with a random arrangement of nanotubes such as sheets or papers [26, 27]. Their weakness is caused by the 'smoothness' of the CNTs, their weak mutual interaction and the small contact area. Deposition of material, usually polymers, between the nanotubes can improve material strength significantly [28, 29].

Additives can also enhance function: e.g. the selectivity of CNT sensors can be enhanced by coating the nanotubes with organic molecules [30]. This coating then acts as a filter letting only certain molecular species pass while blocking others. In CNT-biosensors, on the other hand, the coating might be endowed with receptors making it part of the transducer [31]. Amphiphilic molecules are often used for coatings as they can be applied conveniently from solution.

In these applications as well as in many others involving CNTs or other nanoscale building blocks it is essential that we can control the material's nanoscale structure, e.g. incomplete coating will reduce the sensors selectivity while an unnecessary thick coating might reduce sensitivity and increase response times. It is generally accepted that efficient structural control at the nanoscale can only be achieved by 'bottom-up' methods and that self-assembly processes will play a key role. Self-assembly processes are attractive as they allow us to control nanoscale features via convenient macroscopic control parameters such as concentration and temperature without direct intervention at the nanoscale.

Experimental investigation of the details of adsorption and self-assembly of amphiphilic molecules on CNTs is challenging and only a limited number of systematic stydies are available in the literature. For example, Utsumia et al. [51] and Matarredona et al. [50] studied adsorption of NaDDBS on single wall carbon nanotubes. Their experiments show that adsorption follows a two-step mechanism which is due to debundling of the CNTs. Detailed interpretation of the results are, however, difficult as no direct evidence of the adsorbed structures was available. Transmission electron microscopy was used by Richard et al. [106] to study aggregation of different surfactants on various CNT samples. They observed a wide range of adsorbed structures which were strongly dependent on the thermodynamic conditions. Shvartzamn et al. [55] used high sensitivity differential scanning calorimetry to study self assembly of surfactants on CNTs. They found that the nanotube diameter has a great influence on the structure of the adsorbed phase.

Computer simulations are convenient tools to study amphiphilic self assembly on CNTs as they allow us to investigate the thermodynamics of self-assembly as well as the structure of the adsorbed phase within the same simulation framework, thus, avoiding the intrinsic experimental problem of observing the adsorbed structures. A

number of methods, usually using a coarse-grained description, have successfully been employed to study adsorbed structures of amphiphilic and non-amphiphilic organic molecules on CNTs and other surfaces. Düren et al. [58] used Grand Canonical Monte Carlo simulations to study the adsorption of Methane inside CNTs. Canonical Monte Carlo has been used to investigate the wrapping of polymers around CNTs in the work of Gurevitcha et al. [59]. Nativ et al. [56] used classical Molecular Dynamics to study adsorption and aggregation of amphiphilic molecules on a single wall carbon nanotube (SWCNT). They found that adsorbed surfactant molecules cause a long ranged repulsive force between the nanotubes. This creates a repulsive barrier hindering rebundling of nanotubes. Qiao et al. [57] and Wallace et al. [53] used Molecular Dynamics to investigate the dependence of adsorbed structures on the bulk concentration and calculated the average orientation of the surfactant molecules with respect to the CNT-axis to characterize the structures. Dissipative Particle Dynamics (DPD) has successfully been used by Pastorino et al. [83] to investigate the properties of polymer brushes on planar surfaces.

In this paper we employ dissipative particle dynamics (DPD) simulations to study surfactant self-assembly from solution onto crossing single wall CNTs to understand self-assembly processes in materials comprising randomly arranged CNTs as the fundamental building blocks. We find that (i) self assembly is directed to the nanotube/nanotube crossings due to a concentration of hydrophobic forces in these regions and (ii) self-assembly can be controlled efficiently by the concentration of the amphiphiles.

Model and Simulation

Model

In this paper we employ computer simulations to study self-assembly of amphiphilic molecules in bulk solution and on carbon nanotubes. In the simulations surfactant molecules are represented by a chain of beads (H_5T_5) consisting of a block of five hydrophilic head (H) beads and a block of five hydrophobic tail (T) beads while the solvent is considered implicitly. The implicit treatment of the solvent as well as the coarse-grained character of the surfactant beads causes the beads to interact via effective potentials. In the present case we employ a common empirical model where the inter-

actions between a pair of hydrophobic beads is attractive, while all other bead/bead interactions are repulsive. Attractive interactions between beads i and j are represented by the pair potential $\phi(r_{ij})$ which is based on the force shifted Lennard-Jones (LJ)(12,6) potential

$$\phi_{\mathrm{LJ}}(r_{ij}) = 4\epsilon \left[\left(\frac{\sigma}{r_{ij}} \right)^{12} - \left(\frac{\sigma}{(r_{ij} - r_{cut})} \right)^{6} \right] \tag{5.1}$$

$$\phi(r_{ij}) = \begin{cases} \phi_{\mathrm{LJ}}(r_{ij}) - \phi'_{\mathrm{LJ}}(r_{\mathrm{cut}}) r_{ij} - \phi_{\mathrm{LJ}}(r_{\mathrm{cut}}) & r_{ij} < r_{\mathrm{cut}} \\ 0 & r_{ij} \geq r_{\mathrm{cut}}, \end{cases} \tag{5.2}$$

where $\phi'_{\mathrm{LJ}}(r) = d\phi_{\mathrm{LJ}}(r)/dr$ and r_{cut} is the cut-off-radius. In eq.(5.1) $r_{ij} = \|\mathbf{r}_{ij}\|$, $\mathbf{r}_{ij} = \mathbf{r}_j - \mathbf{r}_i$ and $\mathbf{r}_i$ and $\mathbf{r}_j$ are the positions of i and j, respectively; ϵ is the well depth and σ the length parameter of the LJ potential. Repulsive interactions are represented by the Weeks-Chandler-Anderson (WCA) potential given by eq.(5.2) with $r_{\mathrm{cut}} = 2^{1/6}$. For simplicity, these interactions are assumed to be present between all pairs of beads regardless whether they are bonded or not. In addition, two beads k and l which are nearest neighbors in a single surfactant chain interact via the harmonic bond potential

$$\phi_{\mathrm{bond}}(r_{kl}) = \epsilon_{\mathrm{bond}}(r_{kl} - r_{\mathrm{bond}})^2, \tag{5.3}$$

where ϵ_{bond} is the depth of the potential well and r_{bond} the bond length. Superposition of the nonbonding interaction and the harmonic bond potential with $\epsilon_{\mathrm{bond}} = 4\epsilon$ and $r_{\mathrm{bond}} = 1.2\sigma$ (table 5.1) leads to an average nearest neighbor H/H distance of 1.35σ and a T/T distance of 1.26σ. Thus, surfactant molecules are represented by a not too loose chain of beads.

At the length scale of the coarse-grained surfactant beads the atomistic structure of the nanotubes becomes (essentially) irrelevant and surfactant beads interact with the mean-field of the nanotube. Therefore we model the nanotubes as smooth cylinders. They interact with the hydrophobic surfactant beads via the force shifted Lennard-Jones (12,6) potential in eq.(5.2) which is also shifted to the surface of the nanotubes

$$\phi_{\mathrm{CNT}}(r_i) = \frac{\epsilon_{\mathrm{CNT}}}{\epsilon} \phi(r_i - r_{\mathrm{CNT}}) \tag{5.4}$$

where r_i is the shortest distance between bead i and the nanotube axis (for the formula

see e.g. Ref.[66]) and r_{CNT} is the radius of the nanotube. Interactions of the hydrophilic head beads with the nanotubes are modeled using the WCA potential, i.e. $\phi_{\mathrm{CNT}}(r_i)$ with $r_{\mathrm{cut}} = 2^{1/6}$. All potential parameters can be found in table 5.1.

While the present model has been widely used two specific features, i.e.the form and especially the well depth of the interaction between surfactant beads and the nanotubes, deserve a more detailed discussion. For this interaction we assume a LJ (12,6) potential because of its simple mathematical form and because it describes the actual physical situation well. Single wall carbon nanotubes consist of a single layer of carbon atoms located on the surface of a cylinder. Mean-field approximation for the interaction of a single LJ particle with a single planar layer of LJ particles leads to a (10,4) potential [67]. Because of the curvature of the cylinder the mean-field potential is slightly steeper in the case of CNTs (see [68] for the formal prove and [69] for an approximation). Thus, the resulting potential is very similar to a LJ (12,6) potential. Moreover, Patel et al. have fitted an LJ (12,6) potential to the potential of mean force between a carbon nanotube and methane (CH_4) molecules obtained from MD simulations and found excellent agreement [70]. The latter result is of particular relevance as it includes also the hydrophobic interaction. Thus, at the level of detail considered here the LJ (12,6) potential is a very reasonable choice.

As the focus of this paper is to investigate adsorption and aggregation of surfactant molecules on CNTs it is important to use a value for the ratio $\epsilon_{\mathrm{CNT}}/\epsilon$ that is realistic and could be reproduced experimentally. The bead/bead interaction consists of at least two parts: the van der Waals interaction and the (effective) hydrophobic interaction, and is usually vastly dominated by the hydrophobic part. Calculations using the potential form of Ref. [69] reveal that for typical single wall carbon nanotubes with radii of a few nm the well depth of the van der Waals bead/nanotube interaction is approximately 2.7 times deeper than that of the bead/bead interaction. To estimate the ratio of the strength of the hydrophobic part of the bead/nanotube and that of the bead/bead interaction we estimate the ratio of the excluded surface areas. As a crude approximation it can be assumed that the strength of the hydrophobic interaction between two hydrophobic particles depends linearly on the size of the surface area that becomes unavailable to the solvent upon contact of the particles [71]. In the present case of spherical beads and cylindrical nanotubes we find a ratio of the bead/nanotube

to the bead/bead hydrophobic interaction of approximately 1.37(see appendix). If we assume that the hydrophobic interaction contributes 90% of the total interaction ([73]) we find $\epsilon_{\mathrm{CNT}}/\epsilon \approx 1.5$.

Our model, which is empirical and contains no fitted parameter, is also validated by comparison with experiments. The model predicts that the ratio between the critical surface aggregation concentration and the cmc $C_{\mathrm{csac}}/C_{\mathrm{cmc}} \approx 0.3$. Matarredona et al. have measured NaDDBs adsorption on CNTs from aqueous solution and find $C_{\mathrm{csac}}/C_{\mathrm{cmc}} \approx 0.1$ [50] which is in reasonable agreement with our results. It is also important to realize that one has some control over the strength of the van der Waals and the hydrophobic interaction in practise. The van der Waals interactions can be altered by altering the chemistry of the surfactants while the hydrophilicity of the solvent can be controlled using cosolvents (see e.g. Ref. [74]).

Simulation

We investigate the system in the canonical ensemble using the dissipative particle dynamics (DPD) method [79]. In DPD two particles i and j interact via the pairwise force

$$F_{ij} = F_{ij}^C + F_{ij}^R + F_{ij}^D \tag{5.5}$$

where F_{ij}^C, F_{ij}^R and F_{ij}^D are the conservative, the random and the dissipative force, respectively.

The conservative force acts along the line connecting i and j , $\widehat{\mathbf{r}}_{ij} = \mathbf{r}_{ij}/\|\mathbf{r}_{ij}\|$, and depends only on the distance r_{ij} between i and j. It is given by the first derivative of the interaction potentials discussed above

$$F_{ij}^C = \begin{cases} -\left[\phi'(r_{ij}) + \phi'_{\mathrm{bond}}(r_{ij})\right]\widehat{\mathbf{r}}_{ij} & \text{nearest neighbors} \\ -\phi'(r_{ij})\widehat{\mathbf{r}}_{ij} & \text{else} \end{cases} \tag{5.6}$$

The random force

$$F_{ij}^R = \begin{cases} -\xi\omega^R(r_{ij})\theta_{ij}\widehat{\mathbf{r}}_{ij}\frac{1}{\sqrt{\Delta t}} & r_{ij} \le r_c \\ 0 & r_{ij} > r_c \end{cases} \tag{5.7}$$

represents forces from the (rapidly moving) degrees of freedom which have been coarse-

grained out, such as collisions with solvent particles leading to Brownian motion of solutes. In DPD these forces are assumed to be pairwise and random in strength. In eq.(5.7) Δt is the simulation time step, ξ is a parameter determining the maximal strength of the random force, $\omega^R(r_{ij})$ is a weight function characterizing its distance dependence and θ_{ij} is a random variable with limits -1 and 1, zero mean, and unit variance (see [78] for the random number generator we are using for our long trajectories). As the conservative force, the random force acts along the line connecting i and j.

The dissipative force (or drag force)

$$F_{ij}^D = \begin{cases} -\gamma\omega^D(r_{ij})(\widehat{\mathbf{r}}_{ij}\cdot\mathbf{v}_{ij})\widehat{\mathbf{r}}_{ij} & r_{ij} < r_c \\ 0 & r_{ij} > r_c \end{cases} \tag{5.8}$$

represents the viscous drag mediated by degrees of freedom which have been coarse-grained out. In eq.(5.8) γ is the strength parameter and $\omega^D(r_{ij})$ is the weight function of the dissipative force. It is a pairwise force acting along the line connecting the interacting particles i and j and it reduces the relative velocity (component along $\widehat{\mathbf{r}}_{ij}$) $\widehat{\mathbf{r}}_{ij}\cdot\mathbf{v}_{ij}$, where $\mathbf{v}_{ij} = \mathbf{v}_j - \mathbf{v}_i$ and $\mathbf{v}_i$ and $\mathbf{v}_j$ are the velocities of i and j, respectively.

In the canonical ensemble the dissipative and the random force are not independent but connected by the fluctuation dissipation theorem leading to

$$\begin{aligned} \omega^D(r_{ij}) &= \left[\omega^R(r_{ij})\right]^2 \\ \xi^2 &= 2\gamma k_B T, \end{aligned} \tag{5.9}$$

where k_B is Botzmann's constant and T is the temperature. Thus, the random and the dissipative forces together constitute the DPD thermostat. Here we use the weight functions originally published in Ref. [79]

$$\omega^D(r_{ij}) = \begin{cases} (1 - r_{ij}/r_{\text{cut}})^2 & r_{ij} < r_{\text{cut}} \\ 0 & r_{ij} > r_{\text{cut}}, \end{cases} \tag{5.10}$$

where we have chosen $\omega^D(r)$ to be of the same range as the attractive conservative force.

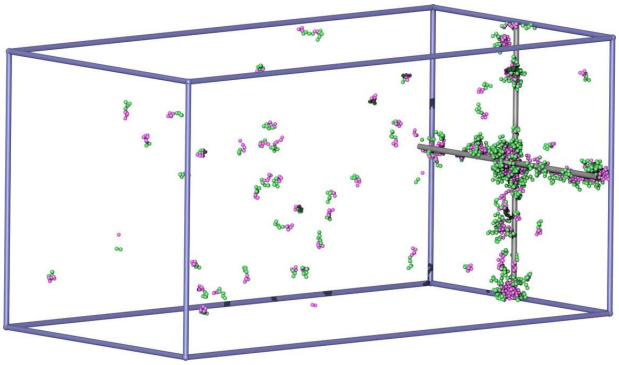

Figure 5.1: Elongated Simulation Box of size $100\sigma \times 100\sigma \times 200\sigma$. The CNTs are positioned on the far right side of the box and are partially covered with surfactant molecules. The usual periodic boundary conditions are applied in all three dimensions. Blue lines demarcate the simulation box.

In all simulations we employ the usual periodic boundary conditions. Bulk simulations are carried out in a cubic simulation box while for the adsorption studies it is more convenient to use an elongated box that has the form of a quadratic prism (figure 5.1). This allows us to study the adsorbed phase in equilibrium with a bulk (like) phase in the same system. We assume that at a distance of 30σ away from the nanotube the solution exhibits bulk properties as no correlations should be longer ranged. This is important as the bulk concentration is the key link to experiments.

For the adsorption simulations it is convenient to be able to fix the bulk concentration. To achieve this we perform chain insertions and deletions in the bulk-like region during the first half of the equilibration period, while in the second half the system is conventionally equilibrated in the canonical ensemble by standard DPD. Every 300 timesteps insertions or deletions are attempted if the actual concentration deviates from the target concentration by +5% or -5%, respectively. Insertion is accepted if none of the beads of the new molecule interacts with any existing chain. If this is not the case the insertion trial is repeated at different locations until it is successful. The acceptance probability is usually very high since the (bulk) concentration is very low.

The nanotubes are placed on one side of the box (figure 5.1). They are rigid and their position is fixed. Since the tubes are not allowed to move they interact with the surfactant molecules only via the conservative part of the force.

$$F_i^{\mathrm{CNT}} = \phi'_{\mathrm{CNT}}(r_i) \tag{5.11}$$

Surfactants					
T beads	=	5	H beads	=	5
ϵ	=	1.0	σ	=	1.0
ϵ_{bond}	=	4.0	σ_{bond}	=	1.2
Nanotubes					
r_{CNT}	=	1.0	d_{CNT}	=	3.0
θ_{CNT}	=	$\pi/2$	ϵ_{CNT}	=	1.5
Simulation					
T	=	0.7	Δt	=	0.005
attractive: r_{cut}	=	2.5	repulsive: r_{cut}	=	$2^{1/6}$
non-conservative: r_{cut}	=	2.5	DPD:ξ	=	1.0
Simulation Bulk					
chains	=	500	cubic box	=	variable dimensions
equilibration	=	$1 \cdot 10^8 \Delta t$	production	=	$0.5 \cdot 10^8 \Delta t$
Simulation Adsorption					
chains	=	variable	elongated box	=	$100 \times 100 \times 200$
equilibration	=	$(1-2) \cdot 10^8 \Delta t$	production	=	$0.5 \cdot 10^8 \Delta t$

Table 5.1: Model and simulation parameters in reduced units: d_{CNT} is the distance and θ_{CNT} the angle between nanotubes.

Simulations are very long $\geq 10^8$ timesteps. The equilibration period of each simulation is determined individually by visual inspection of the evolution of relevant data, such as the concentration of free chains, the number of adsorbed chains etc. This is necessary as equilibration times can vary significantly around the cmc and the csac. Equilibration periods are typically $1 - 2 \cdot 10^8$ time steps in the bulk and 10^8 steps for adsorption studies, while production runs are generally $0.5 \cdot 10^8$ time steps.

In the bulk as well as on surfaces surfactant molecules self-assemble into clusters and aggregates (e.g. micelles). We define that two molecules belong to the same cluster if any inter molecular tail-tail distance is smaller than 1.5σ, i.e the hydrophobic parts of the molecules are in close proximity. To identify all clusters a Depth-First-Search (DFS) algorithm is used (See e.g [88]). We define a molecule as adsorbed if the distance between any of its tail beads and the axis of the nanotube is smaller than $1.5\sigma + r_{\text{CNT}}$.

Reduced Units

Throughout we use reduced quantities: all length are given in units of the LJ length parameter σ, the energy scale is given in units of the well depth of the bead/bead LJ interaction ϵ, the temperature scale is given in terms of ϵ/k_B where k_B is the Boltzmann constant, and time is represented in units of $\sqrt{m\sigma^2/\epsilon}$, where m is the mass of a bead. Concentrations are defined as number (of molecules) densities and given in units of $1/\sigma^3$.

5.2 Results and Discussion

5.2.1 The Bulk Solution

In bulk solutions surfactant molecules form well defined aggregates at some threshold concentration called *critical micelle concentration* (cmc). The cmc depends on the surfactant and the solvent as well as on the thermodynamic conditions. Since our model is empirical and coarse-grained it does not represent one particular experimental solvent/surfactant combination but it describes the generic behavior of all these systems. In order to link our results to the behavior of a specific surfactant and solvent, thermodynamic reference points are needed. The most relevant reference point for self-assembly is the cmc. Therefore we carefully determine the cmc and relate all other results to it.

The cmc indicates the surfactant concentration at which aggregation becomes relevant in the system. We can determine the cmc by plotting the concentration of free surfactant molecules C_1 as a function of the total surfactant concentration C (figure 5.2). At low concentrations no aggregates are formed and, thus, $C_1 = C$. When micelles appear the concentration of free surfactant molecules must be smaller than the total concentration as some surfactant molecules are now bound in micelles. At this point $C_1(C)$ falls below the line $C_1 = C$. After a certain "transition region" one usually observes $C_1 \approx$ const. This is easily observed in figure 5.2.

As micelle formation is a continuous process there is some arbitrariness in the definition of the cmc. Here we define the cmc as the center between the last data point which

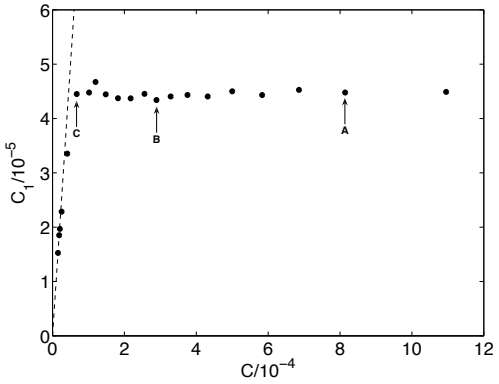

Figure 5.2: Concentration of free surfactant molecules C_1 versus the total concentration of surfactant molecules C. The dashed line demarcates $C_1 = C$ and the arrows indicate data points for which aggregation number distributions are shown in figure 5.4.

approximately follows $C_1 = C$ and the first point which belongs to the group of points for which $C_1 \approx$ const. Thus for the present system we find $C_{\text{cmc}} = 5.2 \times 10^{-5}$.

The snapshot in figure 5.3 gives an impression of the system at $C = 8.2 \times 10^{-4}$ which is well above the cmc. As expected, at this concentration the system is dominated by micelles of approximately spherical shape which are similar in their physical size. From detailed inspection of the snapshots we can obtain a crude estimate of the diameter d of the hydrophobic core of the micelles. At the present concentration $C = 8.2 \times 10^{-4}$ we find $d \approx 4.8$. We have also checked that the physical size of the micelles is very similar for all concentrations above the cmc used in this study.

The observation of similar physical size of the micelles is corroborated by the aggregation number distributions shown in figure 5.4 where we plot the "robability mass function"

$$M(N) = \left\langle \frac{N n_N}{\sum_{N=0}^{\infty} N n_N} \right\rangle , \tag{5.12}$$

where N is the aggregation number of a cluster, n_N is the number of clusters of size N in the system and $\langle \cdots \rangle$ denotes the canonical ensemble average. $M(N)$ can be interpreted as the probability of finding a surfactant molecule in a cluster of aggregation number N. As can be inferred from the distributions in figure 5.4, the aggregation numbers fluctuate around a mean value $\overline{N} = 40$ and, although the distributions have been obtained at significantly different concentrations, they all are relatively narrow and strikingly similar (except in magnitude). This indicates that the system clearly

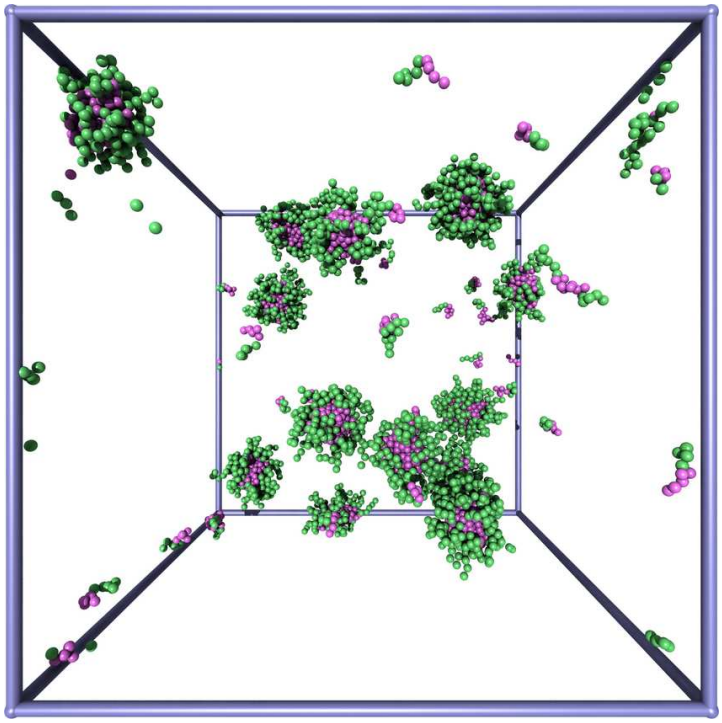

Figure 5.3: Snapshot of the system at $C = 8.2 \times 10^{-4} \approx 16 \times C_{\text{cmc}}$. Hydrophilic beads are shown in purple while hydrophobic beads are colored green. The system contains mostly micelles and only very few free surfactant molecules. The blue frame indicates the simulation box.

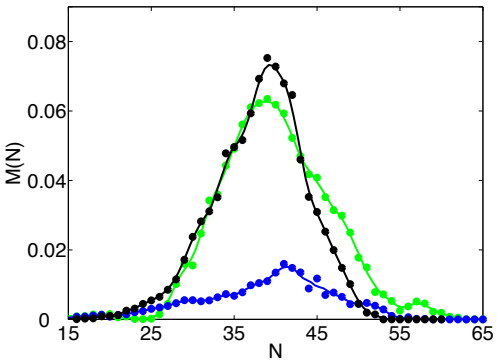

Figure 5.4: Cluster size distributions as probability mass functions for three surfactant concentrations $C = 6.70 \cdot 10^{-5}$ (blue), $C = 2.89 \cdot 10^{-4}$ (green), and $C = 8.12 \times 10^{-4}$ (black) labelled in Fig. 5.2 as A, B, and C, respectively. While the number of aggregates in the system increases with increasing concentration the mean aggregation number remains constant.

prefers spherical micelles consisting of approximately 40 surfactant molecules at all concentrations shown in figure 5.4.

5.2.2 Surfactant Adsorption and Aggregation on Crossing Carbon Nanotubes

The central goal of this work is to investigate how surfactant molecules adsorb and aggregate in the heterogeneous environment formed by crossing carbon nanotubes and to what extent this can be controlled by the (bulk) surfactant concentration. In the snapshot taken at a concentration of $C = 1.59 \cdot 10^{-5}$ and presented in figures 5.5(a) and (b) we observe a number of adsorbed molecules, small clusters and larger clusters which appear to be self-assembled aggregates. One aggregate, which we call the "central aggregate", is located at the nanotube crossing. It seems to be slightly larger in size and to contain more molecules than the others. It also appears to be symmetric, winding around the crossing rather than covering it completely. The other aggregates on the nanotubes seem to be radially asymmetric (with respect to the tube axis) and attach to the nanotubes sidewise rather than enclosing them. This closely resembles hemimicelles which are known to form on planar hydrophobic surfaces [110].

More detailed information is provided by the cluster size distributions presented in figure 5.6. Here the cluster size distribution is defined as the (canonical ensemble av-

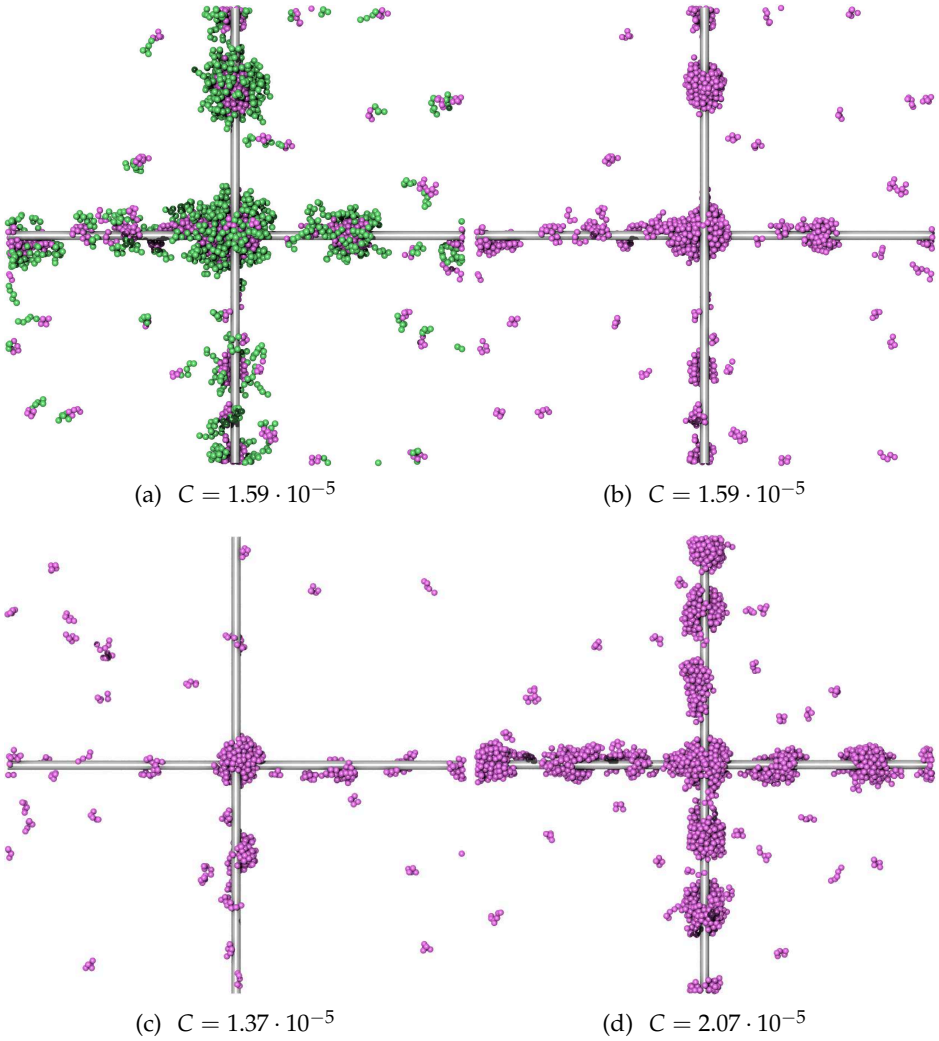

(a) $C = 1.59 \cdot 10^{-5}$ (b) $C = 1.59 \cdot 10^{-5}$

(c) $C = 1.37 \cdot 10^{-5}$ (d) $C = 2.07 \cdot 10^{-5}$

Figure 5.5: Simulation snapshots at various concentrations as indicated in the figure: (a) depicting the hydrophilic surfactant head groups in green and the hydrophobic tails in purple and (b)-(d) showing only the hydrophobic tails. In snapshot (d) the central aggregate is connected to the aggregate below and on the right via only very few molecules.

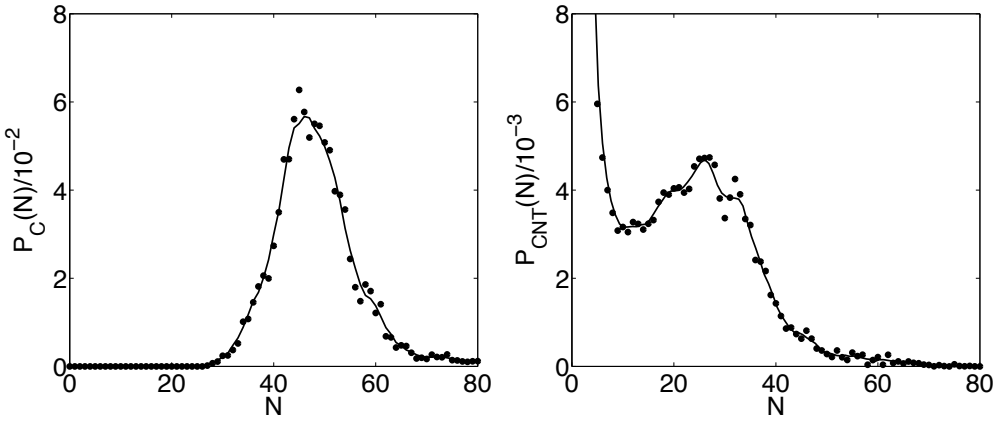

Figure 5.6: Cluster size distributions at $C = 1.59 \cdot 10^{-5}$: (a) for the central aggregate $P_c(N)$ and (b) for all adsorbed clusters excluding the central aggregate $P_{\mathrm{CNT}}(N)$.

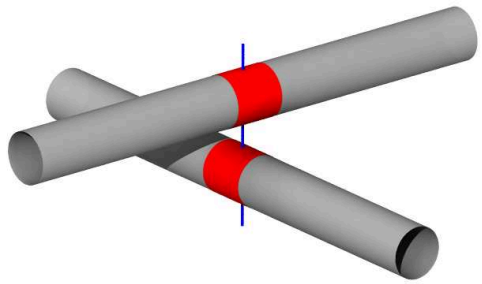

Figure 5.7: A cluster is defined to be adsorbed at the nanotube crossing if one of its molecules is adsorbed within the 1.0σ long nanotube section (indicated in red) which is centered at the center of the crossing (demarcated by the blue line).

erage of the) probability that a certain *adsorbed* cluster has an aggregation number N

$$P(N) = \left\langle \frac{n_N}{\sum_{N=0}^{\infty} n_N} \right\rangle . \tag{5.13}$$

Note that this is different compared to the probability mass function used in figure 5.4. To compute the cluster size distribution of the central aggregate $P_c(N)$ we define a cluster to be adsorbed at the nanotube crossing if at least one of its molecules is adsorbed on one of the nanotubes no further than 0.5σ away from the crossing (figure 5.7).

As the plot in figure 5.6(a) shows, $P_c(N)$ is approximately bell shaped with a maximum at $N_c^{\max} \approx 48$ and, due to the symmetry of $P_c(N)$, the average aggregation number $\overline{N}_c = 48$, which is about 20% larger than the average size of a micelle in the bulk solution (above the cmc). Adsorption energy seems to stabilize the larger aggregate. However, there appears to be a limit to the possible size increase. It is at first surprising that the crossing is not fully enclosed by the central aggregate (figure 5.5(c)) although full enclosement would increase the adsorption energy. On the other hand it is well known that the size (and shape) of micelles in bulk solution is determined by the curvature of the interface between the hydrophobic micellar core and its hydrophilic surrounding. This preferred curvature originates from the space requirements of the surfactant tails and heads. These distinct space requirements also exist in the case where surfactant molecules are adsorbed although altered by the interaction with the substrate(s). Even in the present case of adsorption and aggregation at the nanotube crossing with its large surface area and its very heterogeneous interaction potential the size of the aggregate seems to be largely determined by the surfactants rather than by the surface. This observation indicates that size and shape of adsorbed surfactant aggregates might be predictable based on their bulk counterparts which would represent an important tool for the rational design of nanostructured materials.

The cluster size distribution $P_{\mathrm{CNT}}(N)$ of aggregates adsorbed along the nanotubes (not including the central aggregate) presented in figure 5.6(b) is distinctly different compared to the central aggregate. We observe adsorption of single molecules and small clusters. Their probability decreases quickly with increasing size. Before the probability reaches zero, however, we observe a pronounced shoulder with a weak maximum indicative of surface aggregation. This behavior resembles the bulk solution, although

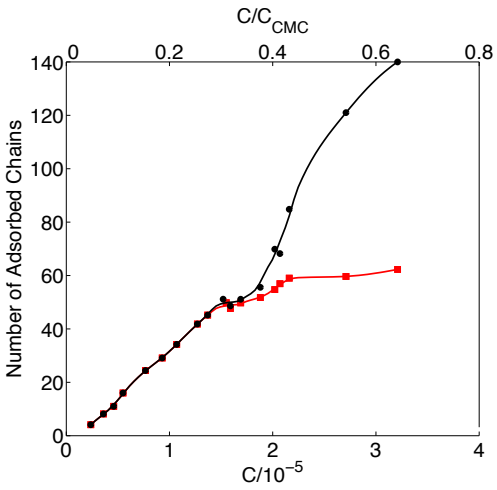

Figure 5.8: Number of surfactant molecules adsorbed at the CNT crossing $\overline{N}_c'$ (•) and the number of chains in the central aggregate defined via the first peak of the cluster size distribution $\overline{N}_c$ (■) as a function of (bulk) concentration. See text for details.

in the adsorbed case $\overline{N}_{\mathrm{CNT}} \approx 28$ is approximately 30% smaller than the average aggregation number in the bulk $\overline{N} = 40$ and the separation of small clusters from micelles is not as pronounced as in the bulk case, i.e. $P_{\mathrm{CNT}}(N) > 0 \quad \text{for all} \quad N < \overline{N}_{\mathrm{CNT}}$.

5.2.2.1 The Central Aggregate

In the case discussed above the central aggregate covers the nanotube crossing well while the rest of the tubes is not fully covered. This suggests that the higher hydrophobic potential at the nanotube crossing directs adsorption and self-assembly towards the crossing. This might offer the opportunity to control self-assembly in CNT materials.

The simplest control parameter known to influence adsorption from solution is the (bulk) concentration of surfactant molecules. As expected, the average number of surfactant molecules in the central aggregate $\overline{N}_c'$ increases with increasing (bulk) concentration (figure 5.8). Furthermore, one immediately recognizes three distinct regions in $\overline{N}_c'(C)$: for $C \leq 1.5 \cdot 10^{-5}$ the aggregation number of the central aggregate increases (essentially) linearly, while in the concentration interval $1.5 \cdot 10^{-5} < C < 2.0 \cdot 10^{-5}$ we find only a weak increase. For $C \geq 2.0 \cdot 10^{-5}$ $\overline{N}_c'(C)$ again increases steeply.

To investigate the origin of this behavior we plot cluster size distributions for the central aggregate $P_c(N)$ at four different concentrations $C = 1.08 \cdot 10^{-5}, 1.59 \cdot 10^{-5}, 2.07 \cdot 10^{-5}$, and $2.71 \cdot 10^{-5}$ in figure 5.9. It is striking that all cluster size distributions pre-

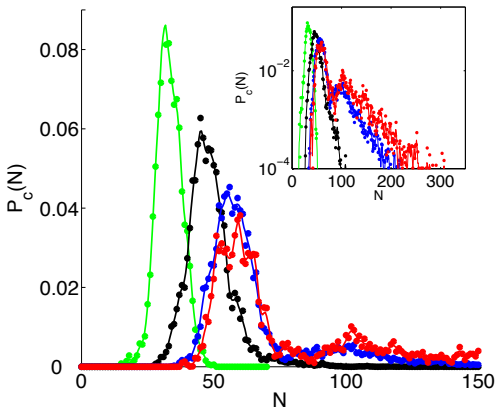

Figure 5.9: Cluster size distributions for the central aggregate $P_c(N)$ for four different concentrations $C = 1.08 \cdot 10^{-5}$ (green), $1.59 \cdot 10^{-5}$ (black), $2.07 \cdot 10^{-5}$ (blue), and $2.71 \cdot 10^{-5}$ (red). To emphasize the tails at large N we replot the functions in a semilogarithmic plot in the inset.

sented in figure 5.9 reveal that the probability of finding a central aggregate of size $N = 0$, i.e. no central aggregate, is zero, from which we draw the important conclusion that the central aggregate is always present and only fluctuates in shape and size but never leaves the nanotube crossing. This is the case for all concentrations in figure 5.8 except the two lowest $C = 0.24 \cdot 10^{-5}$ and $C = 0.36 \cdot 10^{-5}$ ($P_c(N)$ not shown).

At $C = 1.08 \cdot 10^{-5}$ $P_c(N)$ has a relatively sharp peak with $N_c^{\max} \approx 31$ representing the central aggregate and is almost symmetric with the tendency of a slightly higher probability for clusters with $N > N_c^{\max}$. This is consistent with the average cluster size of $\overline{N}_c' \approx 34$ (figure 5.8) which is slightly larger than $N_c^{\max}$.

As C increases the first peak in $P_c(N)$ shifts to larger aggregation numbers until $N_c^{\max} \approx 55$ at which point any further increase of the concentration does not lead to any increase of $N_c^{\max}$ suggesting that the central aggregate does not grow beyond approximately 55 molecules. However, for $C > 1.59 \cdot 10^{-5}$ a new feature appears in $P_c(N)$, that is all cluster size distributions have a "tail". In the case of the two highest concentrations $2.07 \cdot 10^{-5}$ and $2.71 \cdot 10^{-5}$ this tail is very pronounced and shows a peak at $N \approx 100$. This peak is caused by aggregates (of approximately 45 molecules) which *temporarily connect* to the central aggregate rather than being incorporated. As all the concentrations in figure 5.9 are well below the cmc, connecting clusters can not be located in the surrounding (bulk) solution but must be absorbed at the nanotube surfaces. Such a case is shown in the snapshot in figure 5.5(d) (see also supplemental

information).

According to our technical definition of the central aggregate, clusters temporarily connected to the central aggregate by even a single molecule are considered part of it leading to the large tail of $P_c(N)$ and $\overline{N}_c' > 55$. It seems, however, more sensible to redefine the central aggregate to be represented by the first peak of $P_c(N)$. This new definition leads to the mean aggregation number of the central aggregate $\overline{N}_c$ presented in figure 5.8. Up to a concentration of $C \approx 1.5 \cdot 10^{-5}$ both $\overline{N}_c'$ and $\overline{N}_c$ coincide. At higher concentrations, where cluster size distributions show a tail, $\overline{N}_c$ falls below $\overline{N}_c'$ and shows little further increase. $\overline{N}_c$ levels off at approximately 55 molecules indicating that the central aggregate has reached a size limit beyond which it can not grow. This is caused by the tendency of the surfactant molecules to form spherical aggregates under the present thermodynamic conditions. The maximal mean aggregation number of the central aggregate $\overline{N_c}^{\max} = 55$ is considerably larger than the average size of bulk micelles (beyond the cmc) $\overline{N}_{\text{bulk}} = 40$ but it appears that the adsorbed aggregate can not be very much larger than a bulk micelle. This might be a useful guide to chose a surfactant in practice.

5.2.2.2 Adsorption and Aggregation on the Nanotubes

As the (bulk) surfactant concentration changes, both the amount of surfactant molecules adsorbed on the nanotubes and the structure they are forming change. This is shown in figure 5.5 where we present representative snapshots at three concentrations $C = 1.37 \cdot 10^{-5}, 1.59 \cdot 10^{-5}$, and $2.02 \cdot 10^{-5}$. At the lowest concentration shown ($C = 1.37 \cdot 10^{-5}$) we observe a relatively well developed central aggregate while only single molecules and small clusters are adsorbed elsewhere on the nanotubes. At $C = 1.59 \cdot 10^{-5}$ the adsorbed phase also consists of single molecules and small clusters but is dominated by larger (but still small) clusters of similar size which is indicative of aggregation. At the highest concentration $C = 2.02 \cdot 10^{-5}$ almost exclusively large aggregates are adsorbed, some of which seem to be connected to other aggregates and/or to the central aggregate. Since the aggregates occupy almost the entire nanotube surface there is very little space for movement. Because of the periodicity of the system (through the use of periodic boundary conditions) clusters are confined along the nanotubes by the central aggregate(s). It appears that 5 adsorbed aggregates fit well between the

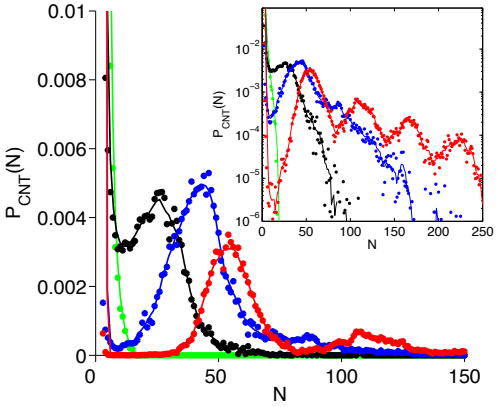

Figure 5.10: Cluster size distributions of adsorbed clusters (excluding the central aggregate) $P_{\mathrm{CNT}}(N)$ for four different concentrations $C = 1.37 \cdot 10^{-5}$ (green), $1.59 \cdot 10^{-5}$ (black), $2.02 \cdot 10^{-5}$ (blue), and $2.98 \cdot 10^{-5}$ (red). To emphasize the tails at large N we replot the functions in a semilogarithmic plot in the inset.

crossings on each nanotube (figure 5.5(d)).

Cluster size distributions of adsorbed clusters (excluding the central aggregate) $P_{\mathrm{CNT}}(N)$ defined according to eq.4.7 and shown in figure 5.10 quantify this observation. The cluster size distributions are distinctly different compared to those of the central aggregate (figure 5.9). At the lowest concentration $C = 1.37 \cdot 10^{-5}$ $P_{\mathrm{CNT}}(N)$ shows that adsorbed molecules occur as individual molecules and small clusters with a quickly decaying probability at increasing size N.

At $C = 1.59 \cdot 10^{-5}$ the cluster size distribution has essentially the same features but it also shows a pronounced shoulder with a weak maximum at $N_{\mathrm{CNT}}^{\mathrm{max}} \approx 25$ which is a clear sign of aggregation.

Similar to the central aggregate, the cluster size distribution of adsorbed clusters shows a small tail with no particular structure. These tails can now be understood considering that $P_{\mathrm{CNT}}(N)$ is largely dominated by (very) small clusters, i.e. adsorbed aggregates are separated along the tubes by individual adsorbed molecules and small clusters. Thus, it is more likely that the aggregates (temporarily) connect to these small clusters rather than to other aggregates. Since the probability of these small clusters decays quickly with increasing size the tail is short and has no maxima.

At all higher concentrations the situation is very different. The adsorbed phase is now clearly dominated by large aggregates. At $C = 2.02 \cdot 10^{-5}$ we find $N_{\mathrm{CNT}}^{\mathrm{max}} \approx 43$ and

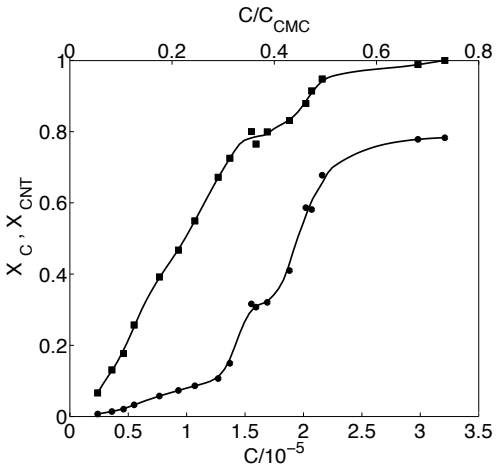

Figure 5.11: Coverage of the nanotube crossing (central aggregate) X_c (•) (obtained from $\overline{N}_c$ in Fig. 5.8) and of the nanotubes not including the central aggregate X_{CNT} (■) as a function of (bulk) concentration.

a second maximum in the tail at $N \approx 85$ while small clusters are almost completely absent. Because of the absence of small clusters aggregates are no longer separated by them and can temporarily connect to each other. At the same time the adsorbed aggregates now also connect to the central aggregate which explains the maximum at $N \approx 100$ in the tail of $P_c(N)$ at $C = 2.07 \cdot 10^{-5}$ shown in figure 5.9. Animations of the system trajectories reveal that for concentrations $C > 2.0 \cdot 10^{-5}$ adsorbed clusters frequently connect and disconnect but rarely loose their identity (supplemental information).

The results discussed above show that surfactant molecules readily adsorb on the nanotubes at concentrations well below the cmc but prefer the nanotube crossing. This is quantified in figure 5.11 where we compare the coverage of the nanotube crossing (central aggregate) X_c and the coverage of the nanotubes (excluding the central aggregate) X_{CNT} as a function of (bulk) concentration. Here coverage is defined as the ratio between the adsorbed amount at concentration C and the amount adsorbed at a reference concentration $C = 7.6 \cdot 10^{-5}$. At this reference state we observe no noticeable increase in adsorption upon further increase of the (bulk) concentration, thus, we regard this state as "fully covered".

As expected, X_c and X_{CNT} increase with increasing concentration. Moreover, the results in figure 5.11 clearly show that adsorption is directed towards the nanotube crossing. Thus, the nanotube crossing reaches full coverage well before the nanotubes are

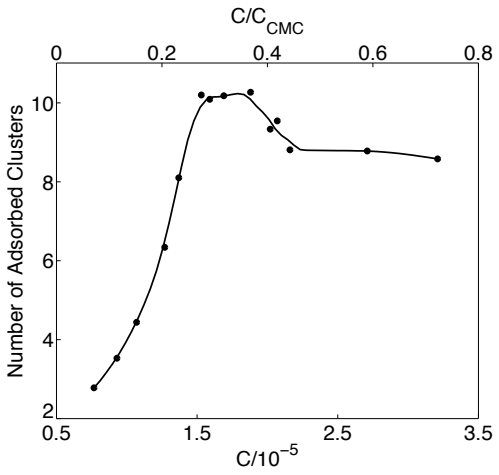

Figure 5.12: Number of adsorbed clusters (excluding the central aggregate) as a function of (bulk) concentration. Here we consider all clusters larger than dimers.

fully covered. This preferential adsorption is caused by the higher hydrophobic potential at the nanotube crossing due to the presence of two hydrophobic surfaces. Due to the preferential adsorption there is a concentration "window" $1.2 \cdot 10^{-5} \lesssim C \lesssim 1.7 \cdot 10^{-5}$ where the central aggregate is well developed while elsewhere the nanotube surfaces are relatively empty. This suggest that we have reasonable control over the adsorbed structures.

Besides these global features our results also provide very interesting insight into the details of the system's behavior. At $C \approx 1.5 \cdot 10^{-5}$ the coverage of the nanotubes X_{CNT} shows a pronounced shoulder, which is also visible in the coverage of the crossing X_c. The steep increase of X_{CNT} preceding the shoulder (figure 5.11) in combination with the appearance of a maximum in the cluster size distributions at all concentrations $C > 1.5 \cdot 10^{-5}$ (figure 5.10) suggest that the *critical surface aggregation concentration* (csac), the concentration where surface aggregation occurs in the system, is located at approximately $1.4 \cdot 10^{-5}$. Surface aggregation causes the coverage to increase quickly until saturation is reached, where it levels off [1]. At the csac aggregates of preferred size are formed (largely on the cost of adsorbed clusters). Thus, the adsorbed amount increases by increasing the *number* of aggregates (of preferred size) until the surface is saturated at which point no new aggregates can be formed.

This interpretation is corroborated by the results in figure 5.12 where we plot the num-

[1] Note that we are well below the cmc thus the "levelling-off" is not related to the bulk cmc as it is in many other cases.

ber of adsorbed clusters (not included in the central aggregate) as a function of (bulk) concentration. Here we consider all clusters which are larger than dimers. The number of adsorbed clusters initially grows with increasing concentration until it reaches a value of 10 at $C \approx 1.5 \cdot 10^{-5}$ just after the csac , thereafter it stays constant at 10. The slight decrease for $C > 2.0 \cdot 10^{-5}$ is caused by connecting clusters.

Increase of the bulk concentration beyond $1.5 \cdot 10^{-5}$ increases the driving force for adsorption. However, because no further aggregate can be adsorbed due to space limitations and because the adsorbed aggregates have already reached their preferred size, X_{CNT} initially increases very little. Upon further increase of C we observe an increase in X_{CNT} (figure 5.11) at a constant number of adsorbed aggregates (figure 5.12). Thus, the increase of the adsorbed amount is due to growth of the aggregates which is corroborated by the cluster size distributions in figure 5.10. This size increase is accompanied by a structural change from hemimicelles to full radially symmetric micelles.

The central aggregate also behaves in an interesting way. Up to $C \approx 1.5 \cdot 10^{-5}$ it grows almost linearly with the (bulk) concentration. Because there is very little adsorption elsewhere on the tubes in this regime the central aggregate is essentially independent. This changes at $C \approx 1.5 \cdot 10^{-5}$, after which the nanotubes are filled and there is exchange between the adsorbed aggregates which is suggested by the tails in the cluster size distributions. Thus, for concentrations larger than $1.5 \cdot 10^{-5}$ the central aggregate is no longer independent but a part of the adsorbed phase. This interpretation is supported by the observation that from this concentration on the behavior of the central aggregate is very similar to that of the other adsorbed aggregates: Initially we observe a range of very little further growth and subsequently all aggregates grow. The only difference is that the central aggregate reaches its maximal size well before the nanotubes are fully covered.

5.3 Conclusions

We have used DPD simulations to study how surfactants adsorb on crossing carbon nanotubes and to what extent this adsorption and the adsorbed structures can be controlled by the bulk surfactant concentration. Computer simulations are well suited for

these investigations as they allow us to study the thermodynamics of surfactant adsorption as well as structural details of the systems within the same simulation framework.

Our key finding is that adsorption is directed to the nanotube crossing due to its higher hydrophobic potential. Adsorbed surfactant molecules form a central aggregate which is somewhat bigger and slightly distorted but otherwise similar to a bulk micelle. In particular, we find that it has a maximal size and can not grow much beyond the size of a bulk micelle. This strongly suggests that the properties of the central aggregate are influenced by the nanotube crossing but are dominated by the aggregation properties of the surfactant molecules. In the present case, bulk micelles are slightly smaller than the crossing, thus, one would expect the central aggregate to cover the crossing only imperfectly which is indeed the case. From these results we draw the conclusion that (i) aggregation is directed to the nanotube crossing and that (ii) it should be possible to estimate the size and shape of the central aggregate from the properties of bulk micelles.

Surfactant molecules also adsorb on the nanotubes outside the central aggregate but the coverage always lags behind that of the crossing, i.e. at lower concentrations the central aggregate forms and at higher concentrations surfactant molecules adsorb everywhere. At the critical surface aggregation concentration (csac) of $C_{\text{csac}} \approx 1.4 \cdot 10^{-5}$ adsorption is associated with surface aggregation. We find that a fixed number of aggregates forms on the nanotubes which does not increase any further upon increase of the bulk concentration. Instead, the surface aggregates grow in aggregation number whereby their shape transforms from hemimicelles to full micelles. From these results we conclude that (iii) we can control the structure of the adsorbed phase (to a certain degree) via the bulk surfactant concentration

5.4 Estimate of the hydrophobic interactions

As a crude estimate it can be assumed that the surface energy of the interface between a hydrophobic solute and a hydrophilic solvent scales linearly with the solvent accessible surface area (sasa), that is the surface area that is available to the solvent (e.g. water). If two hydrophobic solute particles come near each other the sasa decreases,

resulting in a free energy reduction of the system which causes the effective attraction we call ”hydrophobic interaction“. If we further assume that the surface energy is dominated by water and depends little on the specific hydrophobic surface, the strength of the hydrophobic interaction between two hydrophobic solutes is roughly proportional to the reduction in the sasa upon their contact.

For the present study we need to determine the ratio of the hydrophobic interaction between two hydrophobic surfactant beads and that between a hydrophobic bead and a CNT . According to the discussion above this ratio is identical to the ratio of the excluded solvent accessible surface areas (xsasa). In order to calculate this we need to specify some of the length scales in the system. For the present estimate we assume a single wall CNT with a diameter of 1nm and water molecules to have a radius of 0.16nm. The diameter of a surfactant bead in our model (table 5.1) is half the diameter of the nanotubes, thus, 0.5nm. The xsasa for two spherical surfactant beads can be calculated analytically [72], while we obtain the xsasa of the bead/nanotube contact via Monte Carlo integration. From these calculations we estimate the ratio of the hydrophobic bead/bead and the hydrophobic bead/nanotube interactions to be approximately 1.37.

CHAPTER 6

Structural Forces from directed self-assembly

6.1 Introduction

Self-assembly and particularly directed self-assembly of amphiphilic molecules are promising candidates for the bottom-up manufacture of advanced nano-structured materials. Their key advantage is the autonomous formation of a number of nanoscale structures than can be controlled to some extend by macroscopic parameters such as the bulk amphiphile concentration. To use these processes effectively it is necessary that they are well understood.

Surfactant self-assembly has been widely studied in the past experimentally [111, 112], theoretically[113] and using computer simulations[92, 114]. Also, their aggregation behaviour in the presence of solid surfaces [20, 115, 116] and in pores [117–119] has

been investigated. However, for bottom-up techniques understanding of surfactant self-assembly on nanoparticles is critical. Their high mean curvature distincts them from other materials and leads to structures that would not be possible otherwise, e.g. spherical micelles incorporating a thin hydrophobic carbon nanotube [20, 53, 54].

An entirely new aspect comes into play when theses self-assembled structures are to be used to synthesize nanocomposite materials. In this case it is relevant to understand how the self-assembled aggregates influence the material's structure. Thus, knowledge of the surfactant mediated interactions between the other constituents of the material is relevant.

Particularly interesting building blocks are carbon nanotubes (CNTs). The direct interactions between carbon nanotube are dominated by van der Waals (VdW) interactions if they are in vacuum. Using spectroscopic methods O'Connell et al. [33] experimentally estimated the binding energy for two nanotubes in a bundle to be approximately $500eV$ per micrometer of tube-tube contact. VdW forces between tubes have been investigated theoretically. Schroder et al.[34] and Kleis et al. [35] have used a DFT-approach to estimate the interaction strength between parallel and concentric nanotubes. Their results suggested that the binding energy is radius dependent with larger tubes having a larger binding energy per tube. For a pair of tubes of $0.4nm$ they find a binding energy of approximately $1500eV$ per micron of tube length at a tube/tube separation of $0.552nm$. Girifalco et al, [36] use both DFT and an empirical model to estimate the van der Waals binding energy between tubes and found approximately $1000eV$ per micron of tube/tube contact at room temperature.

As carbon nanotubes are hydrophobic solvent mediated (hydrophobic) forces should are expected in (aqueous) solution[37]. The ratio between VdW and the hydrophobic contribution, to our knowledge, remains experimentally inaccessible. Walther et al. [38] performed fully atomistic molecular dynamics simulations of single wall carbon nanotubes in SPC water. They calculate potentials of mean force for the interaction between (16,0) tubes of radii $0.5 - 0.6nm$. The computed mean force exhibits an attractive maximum at a tube spacing of $0.5nm$ which corresponds to approximately one unstable layer of interstitial water molecules. The authors find that the van der Waals attraction between the carbon surfaces is the dominant force by comparing their solution results to simulations of the system in vacuum. The authors estimate a tube/tube

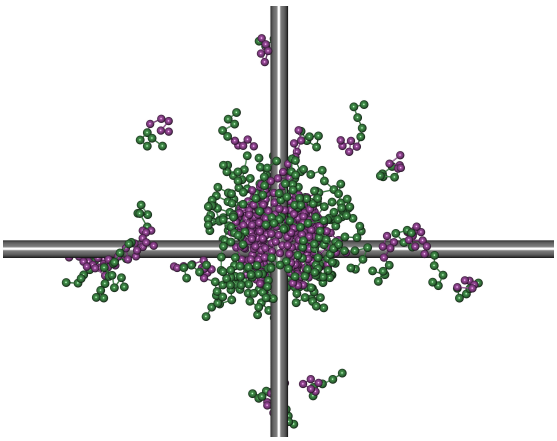

Figure 6.1: Surfactant molecules adsorb and self-assemble into a "central aggregate" at a pair of carbon nanotubes. At the appropriate thermodynamic conditions a central aggregate is formed while most of the tubes' surface area remains empty. Here the distance between the axis of the tubes is $d_{\mathrm{CNT}} = 2.5\sigma$. Hydrophilic beads are shown in purple while hydrophobic beads are colored green.

binding energy, including both VdW and hydrophobic contributions of $850eV$ per micron at a tube spacing of $0.56nm$.

While these results deviate significantly from each other they indicate that strong interactions between the tubes are rather short ranged. They also suggest that the interactions between carbon nanotubes in aqueous solution are dominated by van der Waals interactions.

Here we employ computer simulations to study the forces exerted by surfactant molecules on a pair of crossing carbon nanotubes. The two nanotubes cross at a right angle and a surfactant micelle is formed incorporating the crossing (6.1). This situation can be achieved by adjusting the bulk concentration such that the higher hydrophobic potential at the crossing due to the presence of two surfaces leads to predominant adsorption and self-assembly at the crossing [20]. The distance dependence of the effective force between the tubes generated by the surfactant aggregate is very rich. It is dominated by a large attractive region, i.e. the adsorbed self-assembled surfactant aggregate stabilizes the crossing.

6.2 Model and Simulation

The same model and simulation methodology has been used before[20] therefore we describe it only briefly.

6.2.1 Model

Surfactant molecules (H_5T_5) are represented as a chain of five hydrophilic head (H) beads followed by five hydrophobic tail (T) beads. The solvent is treated implicitly. This and the coarse-grained character of the surfactant beads causes the beads to interact via effective potentials. Here we employ a common empirical model, where the interaction between hydrophobic beads is attractive, while all other bead/bead interactions are repulsive. The force shifted Lennard-Jones (LJ)(12,6) potential $\phi(r_{ij})$ is used to represent attractive interactions between beads i and j

$$\phi_{\mathrm{LJ}}(r_{ij}) = 4\epsilon \left[\left(\frac{\sigma}{r_{ij}} \right)^{12} - \left(\frac{\sigma}{r_{ij}} \right)^{6} \right], \tag{6.1}$$

$$\phi(r_{ij}) = \begin{cases} \phi_{\mathrm{LJ}}(r_{ij}) - \phi'_{\mathrm{LJ}}(r_{\mathrm{cut}})(r_{ij} - r_{\mathrm{cut}}) - \phi^{\mathrm{LJ}}(r_{\mathrm{cut}}) & r_{ij} < r_{\mathrm{cut}} \\ 0 & r_{ij} \geq r_{\mathrm{cut}}, \end{cases} \tag{6.2}$$

where r_{cut} is the cut-off-radius, $\phi'_{\mathrm{LJ}}(r) = d\phi_{\mathrm{LJ}}(r)/dr$, $r_{ij} = \|\mathbf{r}_{ij}\|$, $\mathbf{r}_{ij} = \mathbf{r}_j - \mathbf{r}_i$ and $\mathbf{r}_i$ and $\mathbf{r}_j$ are the positions of i and j, respectively; ϵ is the well depth and σ the length parameter of the LJ potential. Repulsive interactions are modelled using the WCA potential given by eq.(6.2) with $r_{\mathrm{cut}} = 2^{1/6}$. Beads k and l which are nearest neighbours in a chain additionally interact via the harmonic bond potential $\phi_{\mathrm{bond}}(r_{kl}) = \epsilon_{\mathrm{bond}}(r_{kl} - r_{\mathrm{bond}})^2$, where ϵ_{bond} is the depth of the potential well and r_{bond} the bond length.

At the level of coarse graining of the surfactant molecules CNTs are smooth cylinders. Here we model their interactions with hydrophobic surfactant beads via the force shifted Lennard-Jones (12,6) potential in eq.(6.2) which is also shifted to the surface of the nanotubes

$$\phi_{\mathrm{CNT}}(r_i) = \frac{\epsilon_{\mathrm{CNT}}}{\epsilon} \phi(r_i - r_{\mathrm{CNT}}) \tag{6.3}$$

where r_i is the shortest distance[66] between bead i and the nanotube axis and r_{CNT} is the radius of the nanotube. Repulsive interactions with the hydrophilic head beads

Surfactants					
T beads	=	5	H beads	=	5
ϵ	=	1.0	σ	=	1.0
ϵ_{bond}	=	4.0	σ_{bond}	=	1.2
Nanotubes					
r_{CNT}	=	1.0	d_{CNT}	=	$2.0 - 10.0$
			ϵ_{CNT}	=	2.5
Simulation					
T	=	0.7	Δt	=	0.005
attractive: r_{cut}	=	2.5	repulsive: r_{cut}	=	$2^{1/6}$
non-conservative: r_{cut}	=	2.5	DPD:ξ	=	1.0
chains	=	variable	production	=	$0.5 \cdot 10^8 \Delta t$
elongated box	=	$100 \times 100 \times 200$	equilibration	=	$(1-2) \cdot 10^8 \Delta t$

Table 6.1: Model and simulation parameters in reduced units.

are modeled using the WCA potential, i.e. $\phi_{\text{CNT}}(r_i)$ with $r_{\text{cut}} = 2^{1/6}$. All potential parameters can be found in table I.

6.2.2 Simulation

We investigate the system in the canonical ensemble using the dissipative particle dynamics (DPD) method[79]. In DPD any two particles i and j interact via the pairwise force $F_{ij} = F_{ij}^C + F_{ij}^R + F_{ij}^D$, where F_{ij}^C, F_{ij}^R and F_{ij}^D are the conservative, the random and the dissipative force, respectively. The random force is given as

$$F_{ij}^R = \begin{cases} -\xi\omega^R(r_{ij})\theta_{ij}\widehat{\mathbf{r}}_{ij} & r_{ij} \leq r_c \\ 0 & r_{ij} > r_c \end{cases} \tag{6.4}$$

where $\widehat{\mathbf{r}}_{ij} = \mathbf{r}_{ij}/\|\mathbf{r}_{ij}\|$, ξ is the strength parameter and θ_{ij} is a random variable with limits -1 and 1, and zero mean (see Ref.[78] for the utilized random number generator), while the dissipative force is

$$F_{ij}^D = \begin{cases} -\gamma\omega^D(r_{ij})(\widehat{\mathbf{r}}_{ij} \cdot \mathbf{v}_{ij})\widehat{\mathbf{r}}_{ij} & r_{ij} < r_c \\ 0 & r_{ij} > r_c \end{cases} \tag{6.5}$$

where γ is the strength parameter. It is important to recognize that F_{ij}^R is a stochastic force which requires slight modifications of the integration algorithm[79].

In the canonical ensemble the dissipative and the random force are connected by the fluctuation dissipation theorem leading to

$$\begin{aligned} \omega^D(r_{ij}) &= \left[\omega^R(r_{ij})\right]^2 \\ \zeta^2 &= 2\gamma k_B T, \end{aligned} \tag{6.6}$$

where k_B is Boltzmann's constant and T is the temperature. Thus, the random and the dissipative forces together constitute the DPD thermostat. Here we use the weight functions originally published in Ref. [79]

$$\omega^D(r_{ij}) = \begin{cases} (1 - r_{ij}/r_{\text{cut}})^2 & r_{ij} < r_{\text{cut}} \\ 0 & r_{ij} > r_{\text{cut}}, \end{cases} \tag{6.7}$$

where we have chosen $\omega^D(r)$ to be of the same range as the attractive conservative force.

As the bulk surfactant concentration is not one of the natural parameters of the inhomogeneous canonical ensemble it can not be pre-set. Therefore it has been maintained in the initial part of the equilibration period by insertion and deletion of surfactant molecules if the actual concentration in the bulk-like regiondeviates by more than 5% from the target. Because the concentration might change somewhat during the remaining equilibration time, the resulting average concentrations for the individual simulations fluctuate within about 10% of the target value of $C = 1.5 \times 10^{-5}$. This keeps the concentration well in the range where the target structures are expected[20]. We have further confirmed that none of the quantities of interest correlate with the random deviations of the actual concentration.

In all simulations an elongated box is used to provide a bulk-like region for concentration control and the usual periodic boundary conditions are employed. Further details of the simulation protocol can be found in Ref.[20].

6.2.3 Reduced Units

Throughout we use reduced quantities: lengths are given in units of the LJ length parameter σ, the energy is scaled with the well depth of the bead/bead LJ interaction ϵ, the temperature scale is given in terms of ϵ/k_B and time is represented in units of $\sqrt{m\sigma^2/\epsilon}$, where m is the mass of a bead. Concentrations are defined as molecular number densities and given in units of $1/\sigma^3$.

6.3 Results and Discussion

We study the effect of surfactant adsorption on the force between carbon nanotubes. Here we are interested in the situation where two tubes cross at a right angle and the bulk surfactant concentration $C = 1.5 \times 10^{-5} \approx 0.3 C_{CMC}$ is chosen such that adsorption and aggregation occurs predominantly at the crossing[20]. As shown in 6.1, adsorbed surfactant molecules self-assemble into a micelle-like central aggregate.

The surfactants in the central aggregate interact with the tubes which can create a net force acting on each tube. As all forces must be balanced and the two tubes are the only fixed objects in the system, the forces on the tubes must be equal in magnitude and opposite in direction. Thus, surfactants create an effective force between the tubes. It is also possible to view this from a different perspective: If an external force is applied to one of the tubes it is mediated by the surfactants to the other tube.

Because of the symmetry of the crossing the total force exerted by the surfactants on the nanotubes can only act along the direction perpendicular to both tube axes which we define to be the z-direction. Indeed, all simulation results show that the x- and y-components of the average force on the tubes are zero (results not shown). Therefore, only the z-components of the individual bead/CNT interactions contribute to the surfactant generated force between the CNTs

In the canonical ensemble this force between the tubes is defined as

$$F = \left\langle \sum_{i=1}^{N} \sum_{k=1}^{10} f_z(i,k) \right\rangle \tag{6.8}$$

where $f_z(i,k)$ is the z-component of the force exerted by bead k in chain i on the nan-

otube, $\langle \cdots \rangle$ denotes the canonical ensemble average, the first sum runs over all N surfactant molecules and the second over all ten beads in the respective chain.

To analyse the surfactant generated force we simulate a number of independent systems with tube/tube distances from $d_{\mathrm{CNT}} = 2$ to 10 and determine the forces between the tubes. The resulting force-distance curve is presented in 6.2(a). One immediately observes four key features: (i) an initial repulsive region, (ii) decaying oscillations, (iii) an attractive region and (iv) a jump to negligible forces at $d \approx 7.5$.

At $d \approx 7.5$ the central aggregate ruptures leaving only relatively few surfactant molecules adsorbed along the tubes. The majority of the adsorbed molecules form small aggregates on each of the tubes independently (6.3). Therefore the curve representing the aggregation number of the central aggregate, shown in 6.2(b), ends at $d \approx 7.5$. The vanishing of the force between the tubes at $d \gtrsim 7.5$ does, therefore, not surprise. It is also not surprising that the central aggregate disappears at large tube/tube separations. The high hydrophobic potential due to the presence of two hydrophobic surfaces near the crossing leads to the formation of the central aggregate at a concentration where the remaining tube surface can not stabilize large aggregates. As the distance between the tubes is increased beyond $d \approx 7$, the distance between the tube surfaces becomes larger than the average core diameter of the bulk micelles[20] $D \approx 5$. Thus, to significantly benefit from interactions with both tubes the micelle is stretched. Finally, the gap is too large to be bridged by the micelle. At $d \approx 7.5$ the two tubes become independent on the length scale relevant for the studied H_5T_5 surfactant.

To interpret the surfactant/nanotube force at lower distances between the nanotubes it is essential to understand in detail how it is generated. A single independent hydrophobic bead that adsorbs onto a carbon nanotube would be located in the global minimum of the bead/CNT potential. In this situation there are no forces acting on the particle or, equivalently, on the carbon nanotube. If we postulate an "auxiliary" force acting on the bead in the radial direction then the bead will be pushed or pulled out of the bead/nanotube potential minimum until the forces are again balanced. This creates a force between the tube and the bead. If the auxiliary force does not point in the radial direction then there are force components which are not balanced by the interaction with the nanotube.

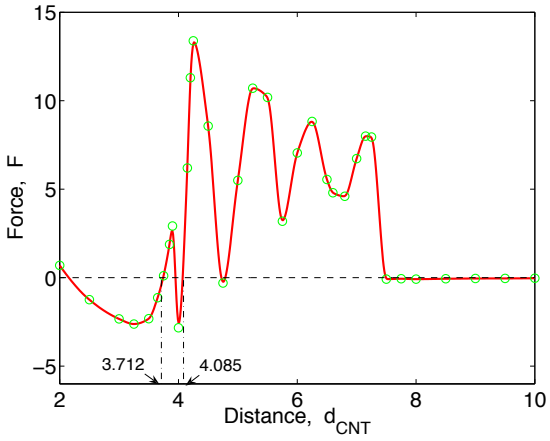

(a)

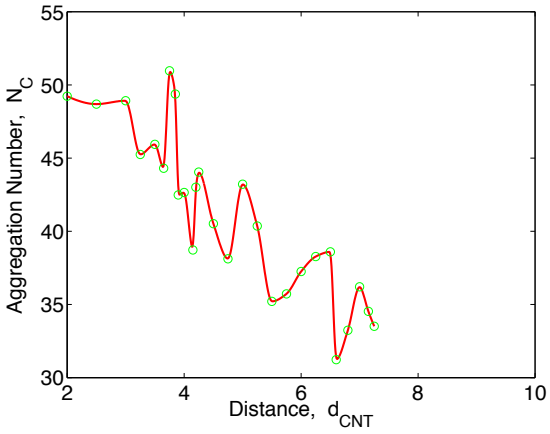

(b)

Figure 6.2: Distance dependence of: (a) the force between the carbon nanotubes generated by the adsorbed surfactant aggregate and (b) the number of surfactant molecules forming the aggregate. The solid lines are guides to the eye. For comparison, the aggregation number of bulk micelles just above the cmc is approximately 41 molecules.

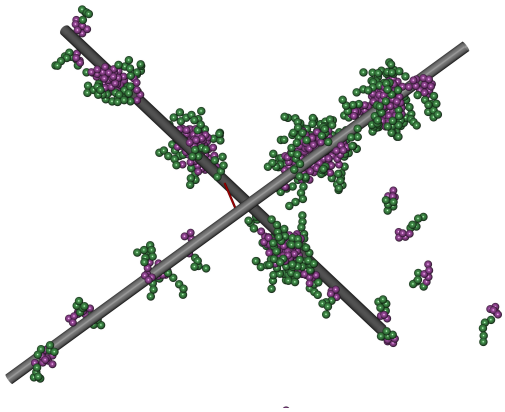

Figure 6.3: At too large tube/tube distances the central aggregate is not formed. Here $d_{\mathrm{CNT}} = 9.0$. The red line indicates the center of the crossing where the central aggregate would be expected to form at smaller distances.

Considering a carbon nanotube positioned such that its axis coincides with the x-axis, one can identify a number of extreme cases. Because of the radial direction of the bead/CNT interaction a particle located in the xy-plane, i.e. $z = 0$ cannot generate a force component in the z-direction. On the other hand, a particle in the xz-plane would have a z-component of the force only. In between these two extreme cases the angle between the z-axis and the bead/tube force vector decreases from $\pi/2$ to 0 as we move from the xy- to the xz-plane and, consequently, the z-component of the force increases.

The forces on a bead interacting with two tubes must be balanced as well. Thus, the force between one tube and the bead must be "relayed" to the other one through other beads or, most importantly, through direct interaction with the second tube. For direct mediation of a force in the z-direction the particle must have a z-component of the force with each of the tubes simultaneously. The rapid decrease of the bead/CNT force with increasing bead/CNT distance prompts to assume that the mediated force is dominated by beads that are simultaneously near both tubes. These are beads located near the global minimum of the bead/CNT potential. We will show later that the density of hydrophobic beads is very high in this region emphasizing its importance.

We now return to the analysis of the force curve. At the smallest tube/tube separations the surfactant generated force between the tubes is repulsive, its magnitude initially

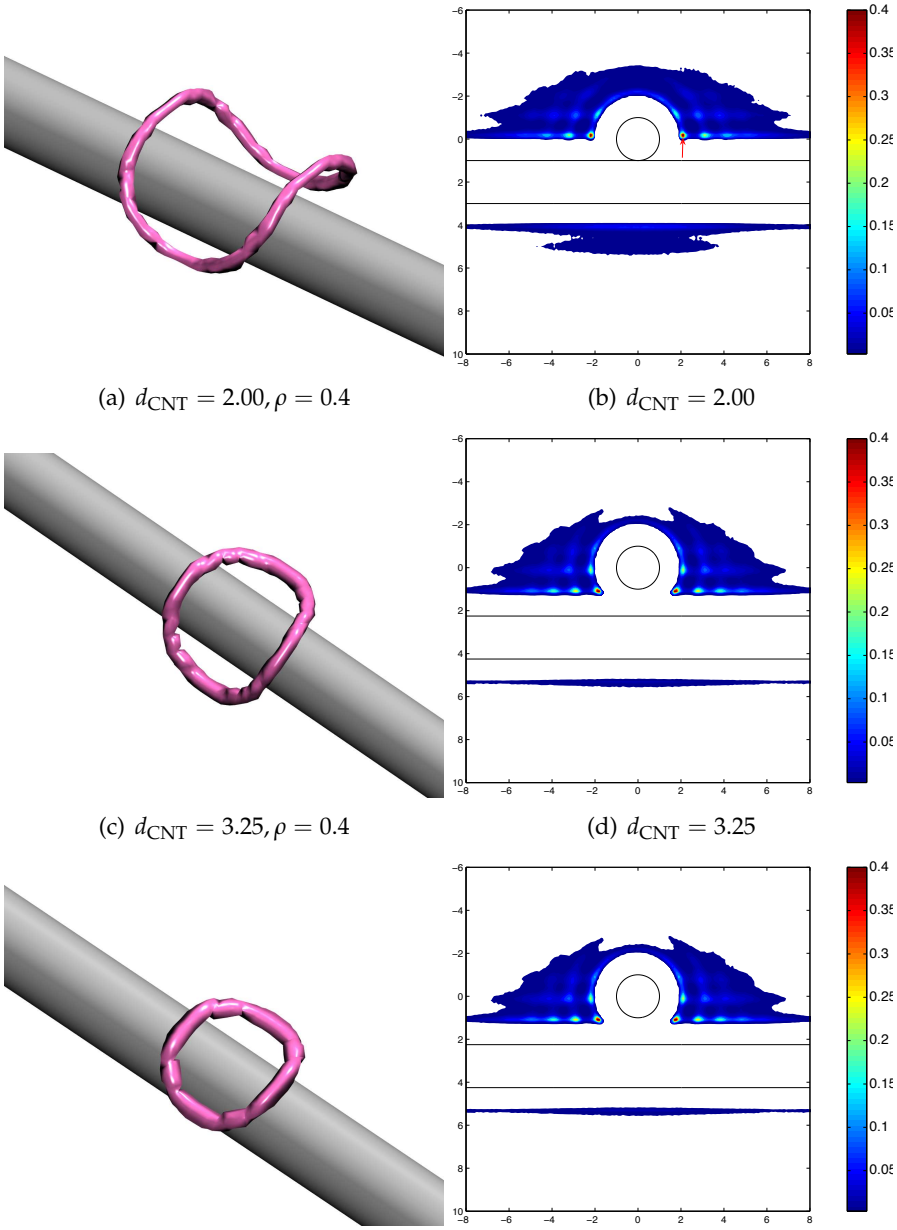

(a) $d_{\mathrm{CNT}} = 2.00, \rho = 0.4$ (b) $d_{\mathrm{CNT}} = 2.00$

(c) $d_{\mathrm{CNT}} = 3.25, \rho = 0.4$ (d) $d_{\mathrm{CNT}} = 3.25$

(e) $d_{\mathrm{CNT}} = 3.75, \rho = 0.4$ (f) $d_{\mathrm{CNT}} = 3.75$

Figure 6.4: Details of the internal structure of the hydrophobic core of the central aggregate in the repulsive force regime at three distances between the tubes d_{CNT} as indicated in the figure: left column - density isosurfaces for $\rho = 0.4$ with the upper tube removed for clarity and right column - local density maps for a plane through the center of the crossing, parallel to the lower tube and perpendicular to the upper tube. The Arrow in part (b) indicates the point of highest bead/CNT potential where beads are in the potential minimum of both tubes simultaneously. Note the diminishing length of the torus of highest density with increasing d_{CNT}.

increases, goes through a repulsive maximum and decreases again. To analyze the origin of this behaviour computer simulations have the great advantage that they provide insighed into the internal structure of the central aggregate. To investigate this internal structure it is represented by local density maps and density isosurfaces in 6.4. The local density maps are shown for a plane that cuts through the center of the central aggregate; the plane is perpendicular to the upper tube and parallel to the lower tube.

The local density maps for tube/tube distances $d_{\mathrm{CNT}} = 2.00, 3.25$ and 3.75 shown in 6.4(b), (d) and (f) reveal that the density of hydrophobic beads is high at positions close to the nanotubes. This is caused by the high hydrophobic-bead/CNT interaction. These regions of high density indicate the position of the potential minimum. The potential minimum for each individual tube forms a cylindrical surface with radius $r_{\mathrm{tube}} + 2^{1/6}$. As the potentials are additive, the intersection line of the two cylindrical surfaces represents the global potential minimum of the crossing. We expect the density to be highest in the global potential minimum as in this position beads can interact with both tubes simultaneously. This is visible in 6.4(b) where the position of the global minimum is indicated by the arrow. The deformed torus in 6.4(a) demarcates the location of highest density in the system and simultaneously the location of the global potential minimum. Consequently, particles in this torus are likely to dominate the effective force between the tubes.

The magnitude of the surfactant generated force between the tubes depends on three factors: (i) the number of particles directly interacting with the two tubes, (ii) the relative size of their force z-component, i.e. the angle between the total force and the z-direction and (iii) the magnitude of the total bead/CNT force.

As is clearly shown in the sequence of density isosurfaces in 6.4 the length of the deformed torus indicating the location of beads near the global potential minimum shrinks with increasing distance between the tubes. Since the density in this region is approximately constant (6.4) the number of beads in the torus is approximately proportional to its length. Thus, the number of bead interacting with both tubes simultaneously decreases with increasing CNT/CNT distance. The dependence is non-linear; it is slow initially and becomes faster as the distance increases.

A bead near the global potential minimum is surrounded by other beads. These beads

are located in the attractive range of the bead/CNT potential which pulls them towards the tubes. This generates a force pushing the first bead out of the potential minimum into the repulsive region of the potential. The general direction of this pushing force is towards the center of the crossing. Like a wedge, the hydrophobic beads are pulled in between the tubes. As the relevant region of the total bead/CNT potential does not change too much we assume this "push" to be approximately constant in the considered tube/tube distance range.

Following again the picture of the wedge it becomes clear that for a constant pushing force the z-component of the responding bead/CNT repulsion becomes larger the smaller the angle between the z-component and the pushing force is. Although not all positions in the torus are identical this angle generally increases as the beads move into the center of the crossing. Thus the force in the z-direction increases as the distance between the tubes increases. This continues until the reduction in the number of force mediating beads overcompensates the effect and the force starts to decrease again creating a repulsive maximum (6.2(a)).

At distances $d \gtrsim 3.5$ the torus is short enough that the particles in it start to correlate. The potential energy of the beads in the torus is minimal if they are located in the global minimum of the bead/CNT potential and simultaneously in the minimum of the bead/bead potentials. For a torus consisting of 8 beads one can calculate the optimal tube/tube distance to be $d_{\mathrm{CNT}} = 3.712$. A bead located in the potential energy minimum does not exert a force on the nanotubes. The force curve in 6.2(a) indicates a zero in the force very near the predicted point.

As discussed above, beads surrounding the inner torus push its particles towards the region between the tubes. Because the particles in the torus are now correlated and interact strongly with each other this push does not need to be compensated by the bead nanotube interactions but is compensated by a slight compression of the torus. As a consequence the zero in the force would be expected at tube/tube separations slightly larger than the "undisturbed" prediction of $d_{\mathrm{CNT}} = 3.712$.

Because of the symmetry of the system another zero in the force is expected for a torus consisting of four hydrophobic beads. Following the same arguments detailed above one obtains $d_{\mathrm{CNT}} = 4.089$ as the predicted location of the zero. This result is again

consistent with the force curve in 6.2(a).

Between the two zeros the force initially becomes attractive, goes through a maximum, them becomes repulsive after going through another zero, and reaches a repulsive maximum before approaching zero again. The natural response of a stable state to distortion is a force counteracting the distortion. Thus, as the tube/tube distance is increased from $d_{\mathrm{CNT}} = 3.712$ the force between the tubes becomes attractive trying to resist the stretching. At some point the structure cannot withstand the deformation any more and yields. This results in a rapid drop of the force. Now the force decreases with increasing distance. As is well known, for a system where the tubes are allowed to move this situation would lead to mechanical instability. In fact, all branches of the force curve with a negative force gradient would be mechanically unstable for free nanotubes.

The next mechanically stable state is the repulsive maximum at $d \approx 4.0$. The structure of the system now resembles that at $d_{\mathrm{CNT}} = 4.089$. As it is compressed the force is repulsive.

It is somewhat surprising that the number of particles in the global potential minimum reflects the symmetry of the system, yet there appears to be no particular structuring of the beads in this region that would indicate a link to the structure of the crossing. This is indicated by the local densities in 6.5(a) and (b). They represent a thick slab of the central aggregate such that the entire torus shown in 6.4(e) is included. The slab is centered in the center between the tubes and oriented parallel to both tubes. The torus depicted in 6.4(e) is clearly visible as an almost perfect circle in the center of 6.5(a). There appears to be significant structuring surrounding the innermost ring of highest density. This is generated as the slab cuts through a number of further tori belonging to regions of high density surrounding the innermost torus depicted in 6.4(e) (6.5(c)).

Between $d \approx 4$ and $d \approx 7.5$ the force goes through a number of oscillations with a wavelength significantly larger than that of the oscillation between $d \approx 3.7$ and $d \approx 4$. Fitting a damped sin-function to this oscillatory region of the force reveals a wavelength of 1.1 which is very close to the location of the bead/bead potential minimum $s^{1/6}$.

Oscillations in force/distance curves have been observed for many confined fluids

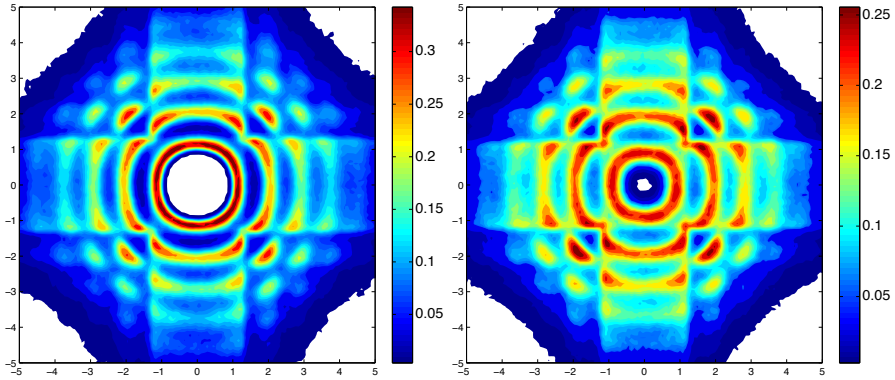

(a) $d_{\mathrm{CNT}} = 3.75$

(b) $d_{\mathrm{CNT}} = 4.00$

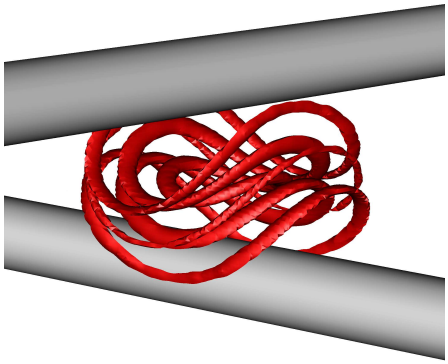

(c) $d_{\mathrm{CNT}} = 3.75$, $\rho = 0.1$. Upper tube is slightly offset to allow better view of the torii structure.

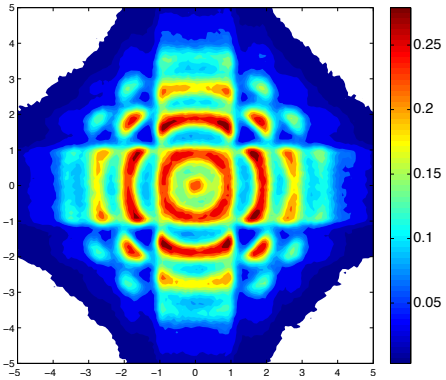

(d) $d_{\mathrm{CNT}} = 4.15$

Figure 6.5: Details of the internal structure of the hydrophobic core of the central aggregate in the regime of high-frequency oscillations: (a), (b), (d) local density maps for a thick slab incorporating the entire inner torus for different tube/tube distances as indicated in the figure and (c) as (a), but density isosurfaces for $\rho = 0.1$. In part (c) the upper tube is slightly offset to allow better view of the tori structure. Note that no particular structure of the inner torus is visible. The intense structure in the region beyond the inner torus is generated by cutting through the outer tori.

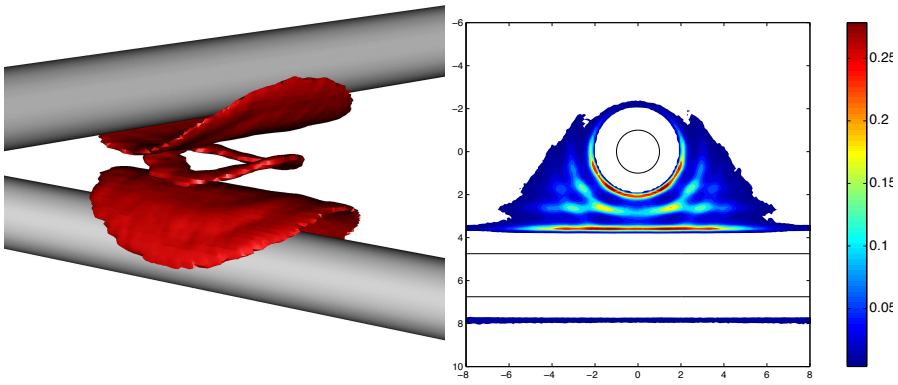

(a) $d_{\mathrm{CNT}} = 5.75, \rho = 0.12$ (b) $d_{\mathrm{CNT}} = 5.75$

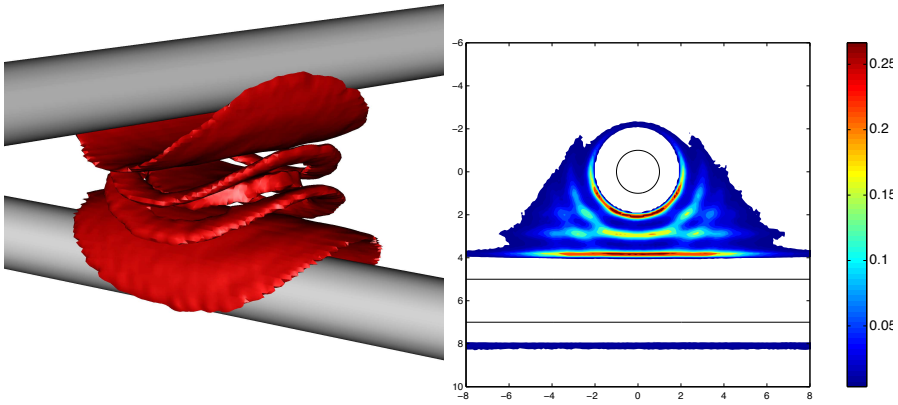

(c) $d_{\mathrm{CNT}} = 6.00, \rho = 0.12$ (d) $d_{\mathrm{CNT}} = 6.00$

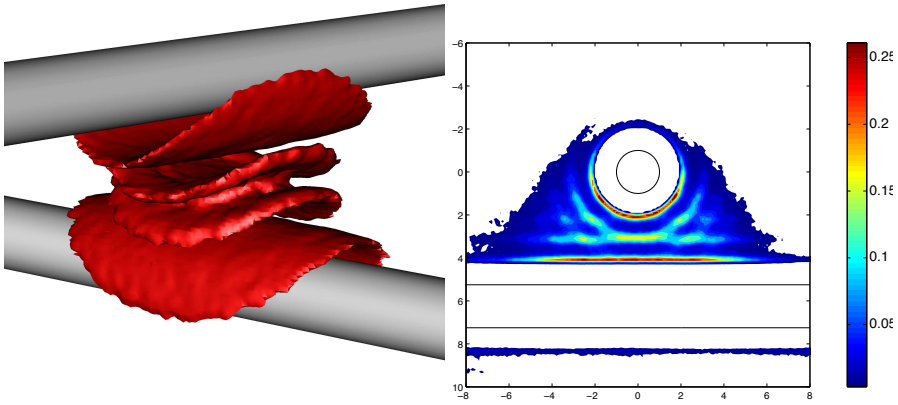

(e) $d_{\mathrm{CNT}} = 6.25, \rho = 0.12$ (f) $d_{\mathrm{CNT}} = 6.25$

Figure 6.6: Details of the internal structure of the hydrophobic core of the central aggregate in the layering regime for three distances around the three layer state: left column - density isosurfaces for $\rho = 0.12$ and right column - local density maps as 6.4. The inner layer forms a hole in the middle when compressed or a bifurcation when stretched. The increasing deformation, i.e. stretching, of the central aggregate with increasing distance between the tubes is visible in the density maps in the right column.

in theoretical and computer simulation studies [120–123] as well as experimentally [124, 125] . They are attributed to layering, i.e. organisation of the molecules of the confined fluid into layers parallel to the surfaces. The ordering is induced by the surface/fluid interaction causing the formation of a dense layer of fluid molecules in the potential minimum. This fluid "surface layer" in turn induces the formation of a second layer. The distance between the first and the second layer is equal to the location of the fluid/fluid potential minimum. If the surface layer is located in the minimum of the surface/fluid potential no forces are excreted on the solid surfaces. If the confined fluid is compressed or stretched by reducing or increasing the distance between the surfaces the confined fluid responds with a repulsive or attractive force, respectively. When, e.g., the compression becomes too strong the fluid yields. The stress is released by reducing the number of layers by one layer. The resulting state is very similar to the initial one but consists of one layer less. This leads to the well known oscillations in the force curve.

The density isosurfaces in 6.6 reveal the layered structure of the hydrophobic core of the central aggregate around $d \approx 6.0$. As the distance between the CNTs is reduced from $d \approx 6.0$ to $d \approx 4.2$ the number of layers is reduced from three in 6.6(b) to one in 6.5(d) where the system is shown at the verge of formation of the first layer. Two layers have been "pushed out" during the compression and the system went through two oscillations in the force curve.

Because of the high curvature of the confining CNTs the layers are not planar (6.6). During compression and stretching the system undergoes a number of morphological changes. Most striking is the creation of a hole in the center of the middel layer where the confinement is highest (6.6(a) and (b)). The formation of the forth layer upon stretching appears to be an essentially continuous process in which the bifurcation, visible in 6.6(e) and (f), moves to the center of the aggregate.

It is important to realize that hydrophobic beads can not just be "pushed out" as they belong to surfactant molecules and these molecules belong to a self-assembled aggregate that is larger than the region of confinement. Thus, the only way of pushing beads out of the region of highest confinement is by deformation of the aggregate. Therefore the oscillations in the number of molecules in the central aggregate is not as strong as one might expect for confined simple fluids. Most importantly, it does not decrease as

the distance between the tubes decreases but increases.

The most striking feature of the force curve is that the surfactant generated force is generally attractive in the region where we observe layering. Following the discussion above it is clear that this attraction can not be generated by the layered confined fluid alone as this would lead to oscillations around $F = 0$. As the system is heterogeneous a surface tension could have the observed effect. The attractive force would be the result of the tendency of the system to reduce the number of molecules in the interface. However, on the contrary, we observe an increase of the number of molecules in the central aggregate with decreasing tube/tube distance suggesting an increase in the size of the interface.

To identify the reason for the attractive interaction let us assume a system with three layers similar to the one shown in 6.6(c). Let us further assume that all layers are located in the respective bead/CNT and bead/bead potentials. The surfactant/CNT force of this system would be zero. (The forceless state is actually slightly different as the middle layer is in the attractive range of the bead/CNT potential but we can ignore this for the moment – a system with two layers would not have this contribution.) In order to cause an attraction between the tubes there must be a constant force trying to pull the beads out of the bead/CNT potential minimum into the attractive region.

The only possible sources of this force are the surfactant head groups. The existence of the pulling force can be proven by calculating the average force stretching the bond that connects the head and the tail parts of the surfactant molecules. The result is presented in 6.7. The bond force is always attractive meaning that heads pull on the tails. Initially it has approximately the same value as in bulk micelles. In this case the pulling is compensated by the attractions between tail beads. If we assume the same to be true for the adsorbed micelle, constituting the central aggregate, the pulling of the head groups is compensated by the attraction of the tails alone. As the distance between the tubes increases to $d \approx 5$ and beyond the bond stretching force increases rapidly. This increase in the force must be compensated by the interaction between the surfactant tail beads and the CNTs.

Comparison of 6.4(b) and 6.6(e) and (f) indicates that at larger tube/tube separations the hydrophobic core of the central aggregate becomes more and more cylindrical.

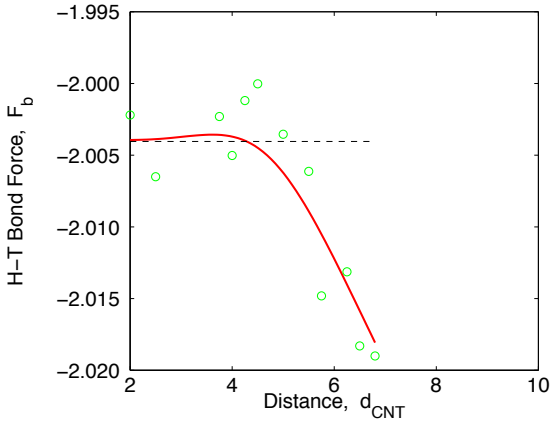

Figure 6.7: Tube/tube distance dependence of the force exerted by the surfactant head groups on the tail groups along the H-T bond connecting the head to the tail of surfactant molecules in the central aggregate. The horizontal line demarcates the bond-stretching force in bulk micelles. Not that for $d_{CNT} \gtrsim 5$ the bond stretching force increases beyond the value found for bulk micelles, indicated by the horizontal line. The solid line is a guide to the eye.

This means that the heads pull essentially perpendicular to the axis of the central aggregate. This can only create a force component acting on the nanotubes and pointing in the z-direction because the tube surfaces are curved. Applying the same arguments detailed to explain the repulsive region $2 \lesssim d \lesssim 3.7$ leads to the conclusion that the additional pulling from the head groups leads to an effective attraction between the tubes.

This leaves the question about the origin of the force excreted by the head groups. As the distance between the tubes increases from $d_{\mathrm{CNT}} = 2.00$ to $d \approx 7.5$ the central aggregate is deformed from an essentially spherical shape to a cylindrical shape. The initial spherical shape is similar to that of bulk micelles. The high curvature provides room for the head groups to move although they are already feeling the confinement and pull on the interface. As the shape becomes more and more cylindrical head groups are becoming more and more confined (6.8). This increased degree of confinement causes some of the molecules to leave the central aggregate (6.2(b)), while the remaining head groups pull more strongly on the tails (6.7). It is interesting to note, that because the attractive force between the tubes is caused by mutual repulsion of surfactant head groups, it is entropic in nature.

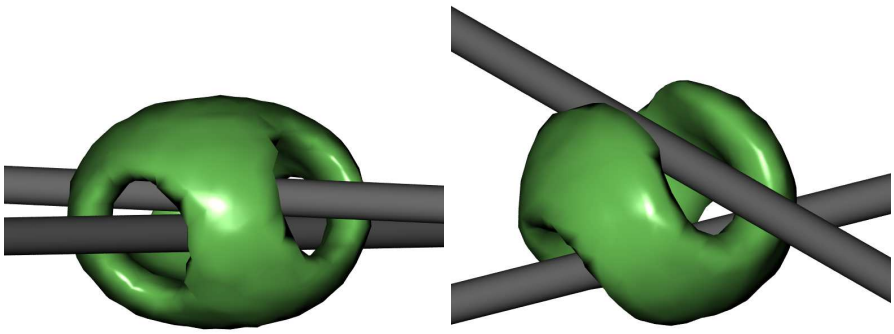

(a) $d_{\mathrm{CNT}} = 2.00, \rho = 0.10$ (b) $d_{\mathrm{CNT}} = 5.75, \rho = 0.10$

Figure 6.8: Density isosurfaces $\rho = 0.10$ for the hydrophilic head groups showing the increased confinement with increasing tube/tube distance.

6.4 Conclusions

Surfactants adsorb and aggregate on crossing carbon nanotubes at concentrations well below the CMC. If the concentration is chosen well, self-assembly occurs only at the crossing where a central aggregate is formed. At small distances between the CNTs this central aggregate resembles a bulk micelle[20].

The results of the present study show that a central aggregate is formed as long as the tube/tube distance is not larger than $d \approx 7.5$. In other words, the aggregate is not formed if the gap between the surfaces of the tubes is larger than the diameter of the hydrophobic core of a bulk micelle[20] which is around 5.

The surfactants in the central aggregate interact with the tubes and create an effective force between them. The dependence of the force on the tube/tube separation is very rich. The key features are: (i) At small separations the force is repulsive as surfactant tail beads are drawn to the tubes by the strong hydrophobic-bead/CNT interaction. (ii) As molecules move into the gap between the tubes, strong layering is observed creating the well known oscillations in the force. Just before a single layer is formed correlations of beads located in the global bead/CNT potential minimum cause additional oscillations at higher frequencies. (iii) The central aggregate disappears at $d \approx 7.5$ and no force is observed at $d \gtrsim 7.5$. (iv) Most importantly, the surfactants create a large attractive region between $d \approx 4$ up to the rupturing distance. This attraction

is entropic in nature and caused by the deformation of the central aggregate and the resulting confinement of the head groups.

The latter observation is most important for the bottom-up design of CNT composite materials: (i) It is possible to direct adsorption and self-assembly to the CNT crossings. (ii) The tubes need to be near each other but do not have to touch. (iii) The aggregate pulls the tube together, thus, stabilizes their target structure.

CHAPTER 7

Surfactant mediated CNT forces

7.1 Introduction

During the past twenty years, Carbon Nanotubes (CNTs) have inspired a wealth of new applications, ranging from biomedical applications [13–15], drug delivery systems [8], to catalyst support in gas diffusion electrodes [9], to sensors [10–12]. It must be expected that many more applications will be developed in the future exploiting one or more of the CNT record properties. Most of these applications will achieve their performance and economic optimum only if they are based on individual tubes instead of bundles. However, the preparation of stable dispersions of individual tubes still represents a formidable challenge.

Due to the strong tube/tube van der Waals (vdW) forces and hydrophobic forces in aqueous solution carbon nanotubes form bundles. The size of these bundles can vary, e.g. SWCNT of approximately $1nm$ diameter typically form bundles with diameters

between $15 - 30nm$ containing $30 - 100$ tubes [126] . To produce dispersions of unbundled and non-functionalized CNTs the bundles are ultrasonicated in presence of a stabilizing agent. Ultrasonication provides the energy needed to break the bundles while the stabilizing agent prevents rebundling. The most common class of stabilizers are amphiphilic molecules such as surfactants and copolymers [41–45].

As CNTs are very hydrophobic, surfactants adsorb with their tail group, thus, orienting the hydrophilic head groups outward. When two surfactant decorated CNTs approach each other from large separations, head groups of surfactants adsorbed on different tubes repel each other generating an effective tube/tube repulsion which shields the tubes from rebundling [127]. Efforts have been made to optimize the dispersions i.e to maximize the concentration of individually suspended CNTs, by changing various experimentally accessible parameters such as concentration, surfactant geometry or surfactant chemistry [128, 129].

The dependance of the stability of SWCNT suspensions on the surfactant concentration has been investigated in a number of experimental studies [49, 51, 52, 55, 56]. These studies illustrate that high surfactant concentrations, well above the Critical Micelle Concentration (CMC), are necessary to stabilize suspensions for long times. However, interestingly, it has also been shown that it is possible to suspend CNTs at concentrations below the CMC [46, 70].

Surfactant geometry has also been proven to be an important parameter. Shvartzman-Cohen et al. [47] used single chain mean field theory to study the dependence of the tube/tube potential on the length of grafted polymers, a situation very similar to adsorbed surfactants. Their results suggest that longer polymeric chains give rise to a longer ranged tube/tube repulsion. It is reasonable to expect that this longer ranged repulsion would lead to better suspension stabilization. White et al. [130], who used zeta-potential measurements, showed that surfactants with the same head group but with shorted tail groups are more efficient as stabilizing agents for SWCNTs.

This is also indicated by the 2D density functional theory study of Patel et al. who showed that even below the CMC the surfactant mediated force for a pair of parallel tubes can be large enouch to dominate the tube/tube attraction. Using atomistic molecular dynamics Xu et al. [61] observed a reduction of the surfactant induced

tube/tube potential of mean force with decreasing SDS coverage of a pair of parallel tubes. However, the high computational cost of their simulations does not allow to establish a link to experimental work via the bulk concentration.

The complexity of the interplay between the surfactant/surfactant interactions, the surfactant/tube interaction, adsorption and aggregation, continues to prevent full comprehension of the role surfactants play in SWCNT dispersion. In all of the aforementioned experimental studies, direct access to the adsorbed surfactant layer morphology is unavailable. Critically, the morphology of the adsorbed layer controls the attractive surfactant mediated tube/tube interaction but is itself controlled by the surfactant properties and the concentration. As computer simulations allow simultaneous access to all these properties they are ideally suited to study surfactant mediated interactions between CNTs.

In this work we determine the surfactant mediated forces between two perpendicular CNTs using DPD simulations of a coarse-grain model, at a concentration approximately equal to the CMC. A coarse grain model is used as it allows control of the surfactant concentration in the solution surrounding the pair of CNTs. The perpendicular configuration is chosen for two reasons: (i) it must be expected to have the lowest surfactant induced barrier for rebundling compared to all other tube/tube angles, as it is associated with the smallest possible overlap volume of the head groups, and (ii) rebundling tubes will almost always collide at an angle. We investigate the origin of the "shielding effectiveness" by establishing a link between the structural properties of the adsorbed layer and the rebundling barrier is established via the tube/tube force-distance curve. Interestingly, a first order transition between the repulsive force regime and an attractive regime at smaller tube/tube separations is discovered. Our ultimate goal is to provide rational arguments for the selection of surfactants that are optimal to stabilize SWCNT dispersions.

7.2 Model and Simulation

7.2.1 The Model

The model and simulation methodology used here have been described before[20, 64]. Surfactant molecules (H_xT_y) are represented as a chain of x hydrophilic head (H) beads followed by y hydrophobic tail (T) beads. The solvent is treated implicitly. This and the coarse-grain character of the surfactant beads causes the beads to interact via effective potentials. We employ a common empirical potential [20, 63], where the interaction between hydrophobic beads is attractive, while all other bead/bead interactions are repulsive. The force shifted Lennard-Jones (LJ)(12,6) potential $\phi(r_{ij})$ is used to represent attractive interactions between beads i and j

$$\phi_{\mathrm{LJ}}(r_{ij}) = 4\epsilon \left[\left(\frac{\sigma}{r_{ij}} \right)^{12} - \left(\frac{\sigma}{r_{ij}} \right)^{6} \right], \tag{7.1}$$

$$\phi(r_{ij}) = \begin{cases} \phi_{\mathrm{LJ}}(r_{ij}) - \phi'_{\mathrm{LJ}}(r_{\mathrm{cut}})(r_{ij} - r_{\mathrm{cut}}) - \phi^{\mathrm{LJ}}(r_{\mathrm{cut}}) & r_{ij} < r_{\mathrm{cut}} \\ 0 & r_{ij} \geq r_{\mathrm{cut}}, \end{cases} \tag{7.2}$$

where r_{cut} is the cut-off-radius, $\phi'_{\mathrm{LJ}}(r) = d\phi_{\mathrm{LJ}}(r)/dr$, $r_{ij} = \|\mathbf{r}_{ij}\|$, $\mathbf{r}_{ij} = \mathbf{r}_j - \mathbf{r}_i$ and $\mathbf{r}_i$ and $\mathbf{r}_j$ are the positions of i and j, respectively; ϵ is the well depth and σ the length parameter of the LJ potential. Repulsive interactions are modeled using the WCA potential given by eq.(7.2) with $r_{\mathrm{cut}} = 2^{1/6}$. Beads k and l which are nearest neighbors in the same chain additionally interact via the harmonic bond potential $\phi_{\mathrm{bond}}(r_{kl}) = \epsilon_{\mathrm{bond}}(r_{kl} - r_{\mathrm{bond}})^2$, where ϵ_{bond} is the depth of the potential well and r_{bond} the bond length.

At the present level of coarse graining of the surfactant molecules CNTs are smooth cylinders. Here we model their interactions with hydrophobic surfactant beads via the force shifted Lennard-Jones (12,6) potential in eq.(7.2) which is also shifted to the surface of the nanotubes

$$\phi_{\mathrm{CNT}}(r_i) = \frac{\epsilon_{\mathrm{CNT}}}{\epsilon} \phi(r_i - r_{\mathrm{CNT}}) \tag{7.3}$$

where r_i is the shortest distance between bead i and the nanotube axis and r_{CNT} is the radius of the nanotube. Repulsive interactions with the hydrophilic head beads

Surfactants					
T beads	=	5	H beads	=	$5, 10$
ϵ	=	1.0	σ	=	1.0
ϵ_{bond}	=	4.0	σ_{bond}	=	1.2
Nanotubes					
r_{CNT}	=	1.0	d	=	$2.0 - 20.5$
			ϵ_{CNT}	=	2.5
Simulation					
T	=	0.7	Δt	=	0.005
attractive: r_{cut}	=	2.5	repulsive: r_{cut}	=	$2^{1/6}$
non-conservative: r_{cut}	=	2.5	DPD:ξ	=	1.0
minimum number of chains used	=	750	production	=	$0.5 \cdot 10^8 \Delta t$
elongated box	=	$100 \times 100 \times 200$	equilibration	=	$(1-2) \cdot 10^8 \Delta t$

Table 7.1: Model and simulation parameters in reduced units. d is the distance between the tube axes.

are modeled using the WCA potential, i.e. $\phi_{\text{CNT}}(r_i)$ with $r_{\text{cut}} = 2^{1/6}$. All potential parameters can be found in table I.

7.2.2 The Simulations

We investigate the system in the canonical ensemble using the dissipative particle dynamics (DPD) method[79]. In DPD any two particles i and j interact via the pairwise force $F_{ij} = F_{ij}^C + F_{ij}^R + F_{ij}^D$, where F_{ij}^C, F_{ij}^R and F_{ij}^D are the conservative, the random and the dissipative force, respectively.

The random force is given by:

$$F_{ij}^R = \begin{cases} -\xi\omega^R(r_{ij})\theta_{ij}\widehat{\mathbf{r}}_{ij} & r_{ij} \le r_c \\ 0 & r_{ij} > r_c \end{cases} \tag{7.4}$$

where $\widehat{\mathbf{r}}_{ij} = \mathbf{r}_{ij}/\|\mathbf{r}_{ij}\|$, ξ is the strength parameter, θ_{ij} is a random variable with limits -1 and 1, and zero mean (see Ref.[78] for the utilized random number generator), and $\omega^R(r_{ij})$ is the weight function of the random force. The dissipative force is given by:

$$F_{ij}^D = \begin{cases} -\gamma\omega^D(r_{ij})(\widehat{\mathbf{r}}_{ij} \cdot \mathbf{v}_{ij})\widehat{\mathbf{r}}_{ij} & r_{ij} < r_c \\ 0 & r_{ij} > r_c \end{cases} \tag{7.5}$$

where γ is the strength parameter, $\mathbf{v_{ij}} = \mathbf{v_j} - \mathbf{v_i}$ and $\mathbf{v_i}$ is the velocity of particle i and $\omega^D(r_{ij})$ is the weight function of the dissipative force. In the canonical ensemble the dissipative and the random force are connected by the fluctuation dissipation theorem leading to

$$\omega^D(r_{ij}) = \left[\omega^R(r_{ij})\right]^2, \quad \xi^2 = 2\gamma k_B T, \tag{7.6}$$

where k_B is Boltzmann's constant and T is the temperature. Thus, the random and the dissipative forces together constitute the DPD thermostat. Here we use the weight functions originally published in Ref. [79]

$$\omega^D(r_{ij}) = \begin{cases} (1 - r_{ij}/r_{\text{cut}})^2, & r_{ij} < r_{\text{cut}} \\ 0 & r_{ij} > r_{\text{cut}} \end{cases} \tag{7.7}$$

where we have chosen $\omega^D(r)$ to be of the same range as the attractive conservative force. It is important to recognize that F_{ij}^R is a stochastic force which requires slight modifications of the integration algorithm[79].

As the bulk surfactant concentration is not one of the natural parameters of the inhomogeneous canonical ensemble, it can not be pre-set. Therefore it has been maintained in the initial part of the equilibration period by insertion and deletion of surfactant molecules if the actual concentration in the bulk-like region deviates by more than 5% from the target. Because the concentration might change somewhat during the remaining equilibration time, the resulting average concentrations for the individual simulations might deviate by about 10% from the target $C = CMC$. These deviations are not expected to have any important influence on the adsorbed structures or forces, as the adsorbed amount levels off well below the CMC, at $C \approx 0.5 \cdot CMC$ [46]. We have further confirmed that none of the quantities of interest correlate with the random deviations in the concentration.

An elongated box is used to provide a bulk-like region for concentration control and the usual periodic boundary conditions are employed.

7.2.3 Definition of Relevant Quantities

The cluster size distribution for adsorbed surfactant clusters is defined here as the (canonical ensemble average of the) probability mass function

$$P(N) = \left\langle \frac{N n_N}{\sum_{N=0}^{\infty} N n_N} \right\rangle, \tag{7.8}$$

where n_N is the instantaneous number of adsorbed clusters of size N and $\langle \cdot \rangle$ denotes the canonical ensemble average .

To investigate the structure of the adsorbed phase, radial density profiles are defined as

$$\rho_r(r) = \left\langle \sum_{i=1}^{N^{ads}} \delta\left(r - r_i\right) \right\rangle, \tag{7.9}$$

where N^{ads} is the number of adsorbed beads and r_i is the distance between bead i and the tube axis and the bead must be part of an adsorbed molecule [91]. A molecule is considered to be an adsorbed molecule if either the molecule itself or one molecule of the same cluster has a bead that is located at a distance from the tube surface no greater than 1.5. Two molecules are considered to belong to the same cluster, if the distance of a tail bead of the first molecule to at least one tail bead of the second molecule is no greater than 1.5. The radial density profile of a bulk micelle is defined in a similar way but in this case r is the distance to the center-of-mass of the hydrophobic core.

We also study the location of micelles adsorbed along the tubes. To specify the position of a micelle J we use the center of mass of its hydrophobic core $\mathbf{C}_J$. The $1D$ density of adsorbed micelles is then given as:

$$\rho_l(l) = \left\langle \sum_{J=1}^{M^{ads}} \delta\left(l - C_J\right) \right\rangle, \tag{7.10}$$

where C_J is the projection of $\mathbf{C}_J$ onto the tube axis, l the position along the tube, and M^{ads} is the instantaneous number of adsorbed micelles. Accordingly, the pair correlation between adsorbed micelles is defined as

$$g(l) = \left\langle \frac{1}{M^{ads}(M^{ads}-1)} \sum_{IJ} \delta(l - |C_I - C_J|) \right\rangle \tag{7.11}$$

where the sum runs over all $M^{ads}(M^{ads}-1)$ pairs of adsorbed micelles.

7.2.4 Reduced Units

Throughout we use reduced quantities: lengths are given in units of the LJ length parameter σ, the energy is scaled with the well depth of the bead/bead LJ interaction ϵ, the temperature scale is given in terms of ϵ/k_B and time is represented in units of $\sqrt{m\sigma^2/\epsilon}$, where m is the mass of a bead. Concentrations are defined as molecular number densities and given in units of $1/\sigma^3$.

7.2.5 Bulk Properties of the Surfactants Used in the Adsorption Studies

Both surfactants used in this study ($H_5T_5, H_{10}T_5$) form spherical micelles in bulk solution at concentrations beyond the respective CMCs of $CMC_{H_5T_5} = 5.2 \cdot 10^{-5}$, and $CMC_{H_{10}T_5} = 1.2 \cdot 10^{-4}$.

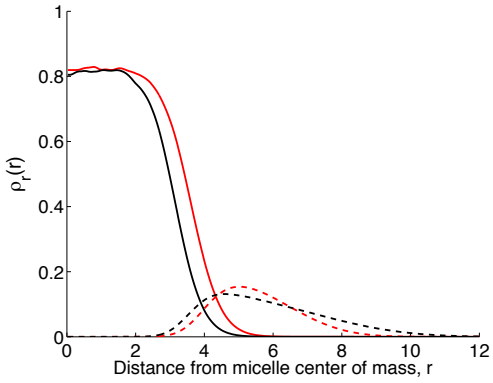

Figure 7.1: The structure of spherical bulk micelles of H_5T_5 (red) and $H_{10}T_5$ (black) at $C \approx CMC$ shown as the radial density of head (dashed lines) and tail beads (solid lines) as a function of the distances from the center of mass. $H_{10}T_5$, the surfactant with longer head group has a smaller core but a larger corona of head groups. Only micelles with sizes deviating by less than 25% from the mean aggregation number are considered.

$CMC_{H_5T_5} < CMC_{H_{10}T_5}$ is expected since a smaller head makes the surfactant less hydrophilic. As commonly done [92] we define the micellar radius r^{mic}, by the inflection point in the radial density profile of the tails beads eq. (7.9) (Fig. 7.1). We find $r^{mic}_{H_5T_5} \approx 3.65$, and $r^{mic}_{H_{10}T_5} \approx 3.125$. The smaller core radius of $H_{10}T_5$ is consistent with the expected stronger steric repulsion between the longer head groups, requiring aggregates with a larger curvature. The mean cluster size of a H_5T_5 bulk micelle was found to be $\overline{N} = 41$, whereas for a $H_{10}T_5$ is $\overline{N} = 30$.

7.3 Results and Discussion

Previously we found that surfactant molecules can self-assemble into a micelle-like central aggregate covering the junction formed by two crossing CNTs (Fig. 7.2) [64]. At low enough concentrations, well below the CMC, no significant adsorption is found on the tube surface [46]. However the high hydrophobic potential at the crossing due to the presence of two hydrophobic surfaces stabilizes the central aggregate. The surfactant mediated forces between the tubes are mostly attractive (Fig. 7.4(a)). Thus, the central aggregate "glues" the tubes together. When the distance between the tubes becomes too large the aggregate ruptures leaving two independent tubes with essentially empty surfaces. As expected, no tube/tube force is detected in this state.

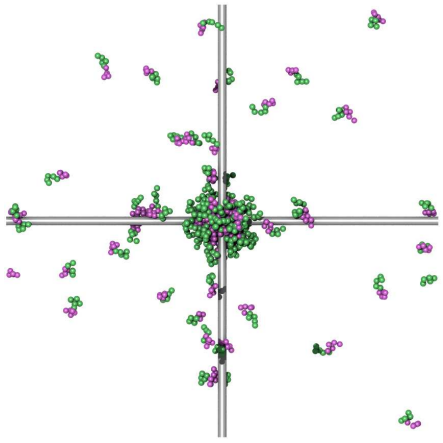

.

Figure 7.2: Snapshot of the system showing a central aggregate covering the crossing point. The distance between the tube axes is $d = 3.0$ and $C \approx 0.20 \cdot CMC$. Hydrophobic tails are shown in purple and hydrophilic heads in green.

Curiously, surfactants are widely used to hinder tube re-bundling in CNT dispersions. The key difference between the two situations – gluing versus shielding– is the difference in concentration. For dispersion, surfactant concentrations are much higher than in the case where we observe gluing – usually well above the CMC. At these concentrations adsorption and aggregation also occurs on individual tubes and not only at the crossing point. The resulting surfactant "coating" is expected to stabilize the dispersion by preventing re-bundling.

The goal of this study is to reveal the origin of the two regimes (attraction versus repulsion) and develop understanding of the intricate details of the dispersion mechanism. Comprehension of these details will enable informed optimization of dispersion stability and thus, dispersion quality.

7.3.1 Surfactant Mediated Force Between CNTs

In vacuum two CNT interact via vdW forces. Even though the strength of this force depends on the tube diameter [36, 68], it is always short ranged. For example, the vdW minumum of two parallel CNTs of $r_{CNT} = 0.95nm$ is $r_{min} = 0.32nm$ [131]. Due to their hydrophobic nature, tubes interact also via an effective hydrophobic interaction when in aqueous solution. In this case, the total force between the tubes becomes slightly longer ranged than in vacuum, i.e $r_{min} \approx 1.1nm$ for the example above [38].

In surfactant solutions surfactant molecules adsorb and self-assemble along the CNTs (Fig.7.3), adding an additional force contribution. In the canonical ensemble the sur-

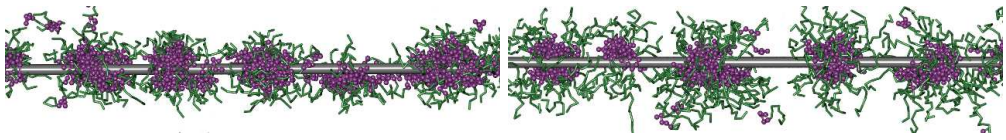

(a) (b)

Figure 7.3: Snapshots of isolated tubes covered with surfactants at $C \approx CMC$. (a) H_5T_5 and (b) $H_{10}T_5$. Adsorbed molecules of both surfactants aggregate into spherical micelles. The longer head groups of $H_{10}T_5$ reach further away from the tube and cause micellar cores to be smaller in size. Hydrophobic tails are shown in purple and hydrophilic heads are are shown in green.

factant mediated force between the tubes is given as

$$F = \left\langle \sum_{i=1}^{N} \sum_{k=1}^{N_{beads}} f_z(i,k) \right\rangle \tag{7.12}$$

where $f_z(i,k)$ is the z-component of the force, i.e the component of the force that is perpendicular to the tube axes, exerted by bead k in chain i on the nanotube, $\langle \cdots \rangle$ denotes the canonical ensemble average, the first sum runs over all N surfactant molecules and the second over all N_{beads} in the respective chain.

The force between two perpendicular tubes mediated by the surfactant H_5T_5 at the CMC is presented in Fig. 7.4(b) . The force curve consists of two distinct regions: An essentially attractive region (blue) for distances between the tube axes $d \leq 8.75$ and a strictly repulsive regime (red) for $d \geq 6.25$. It is also obvious that these two regions overlap for $6.25 \leq d \leq 8.75$.

The shape of the attractive force regime of the curve obtained at $C \approx CMC$ (Fig.7.4 (b)) is nearly identical to that found at $C = 0.2 \cdot CMC$ (Fig. 7.4(a)). The overall attractive nature is caused by a force opposing the deformation of the central aggregate. It originates from increasing steric repulsion between head groups due to the reduced curvature of the central aggregate in the stretched regions. This causes the surfactant heads to pull the tails out of the center of the aggregate between the tubes. As the tails are attracted by the tubes this results in an effective tube/tube attraction. The oscillations in the force is a direct consequence of layering of the tail beads between the tubes (Fig. 7.5).

It is instructive to compare the range of the surfacant mediated forces to that of the vdW and the hydrophobic force. The range of the surfactant mediated attraction is roughly equal to the diameter of the core of a bulk micelle while the length scale of the hydrophobic force is related to the size of a water molecule. If we assume the diameter of one of our beads to be the same as the vdW diameter of one of the water molecules used in [38] the length scale of the hydrophobic interaction is similar to that of the first layer of beads. The vdW interaction is even shorter ranged. Thus, both the vdW and the hydrophobic force influence only the short range part of the attractive-regime essentially by making it more attractive.

At a large enough distance between the tubes the central aggregate ruptures. While at low surfactant concentration rupture leads to empty tube; at $C \approx CMC$ the tubes are covered with surfactants. As a consequence, the surfactant mediated force jumps to zero when the tubes are uncovered and to a repulsive force in the case of covered tubes.

7.3.2 The Repulsive Barrier

The repulsive region of the force curve for H_5T_5 is re-plotted for clarity in Fig. 7.6 (red points). The magnitude of the repulsive force decays monotonically without any obvious distinctive features and vanishes at a tube/tube distance $d_{force} \approx 16.3$. As one would expect, the point where the surfactant mediated force approaches zero is related to the distance $d_{density} = 8.1$ where the radial head-head density around an isolated tube vanishes (Fig. 7.7), i.e $d_{force} \approx 2d_{density}$.

Inspection of Fig. 7.7 also reveals that the radial density of tail beads vanishes at $r^{tail}_{density} \approx 3.5$. Thus, the repulsive regime is not affected by tail/tail interactions. It extends over tube/tube distances where the head densities overlap down to distances where the tail densities begin to overlap.

Clearly, the repulsive regime of the surfactant mediated tube/tube force prevents a pair of approaching tubes from reaching the attractive regime including vdW, hydrophobic and also surfactant mediated interactoins, provided the repulsion barrier is strong enough. As the repulsive regime is correlated with the radial density of head beads it should be controllable via the properties of the surfactant head group. To test this we repeat the study for another surfactant $H_{10}T_5$ with a longer head group. The head group of $H_{10}T_5$ consists of 10 hydrophilic beads, i.e. it is twice as long as that of H_5T_5; otherwise the two surfactants are identical.

Comparison of the repulsive regime of the two surfactants (Fig. 7.6) reveals that increasing the length of the head group has two effects. Firstly, as one expects from the head density profiles (Fig. 7.7), it makes the repulsive region longer ranged and secondly, it leads to a larger force (at all distances). It is immediately obvious that $H_{10}T_5$ shields the tube better than the H_5T_5.

To analyze how much better $H_{10}T_5$ shields the tubes, we estimate the time scale for rebundling which should give a good indication of dispersion stability. As re-bundling can be viewed as a thermally activated process, its rate scales as (7.13)

$$R \sim e^{-B/kT} \tag{7.13}$$

where B is the activation energy. The activation energy is equal to the work required to overcome the repulsive barrier. This work is given by the maximum of the potential of mean force:

$$PMF(d) = -\int_{\infty}^{d} F(d')dd', \tag{7.14}$$

where d is the CNT-CNT distance measured from their axes and $F(d)$ is the surfactant mediated force (Fig. 7.6). The PMFs are shown in Fig. 7.8 and have been obtained by numerical integration of the simulation raw data (Fig. 7.6). Both PMFs are monotonous functions of approximately parabolic shape, in agreement to the ones obtained by Xu et al. in [61] for SDS on two parralel CNT. They are also very similar

to the PMF curves obtained by Cohen et al. [47] obtained for grafted polymers on nanotubes by single chain mean field theory.

The repulsive barrier for $H_{10}T_5$ and H_5T_5 is found to be $B_{H_5T_5} = 7.14kT$, and $B_{H_{10}T_5} = 9.40kT$, respectively. The surfactants with the larger head group shows, expectantly, a higher barrier. Although the difference in the barrier height is small, the difference in the associated time scales for re-bundling can be quite significant. Using (7.13) we estimate that the re-bundling rate of tubes shielded by $H_{10}T_5$ is 10 times lower than in the case of H_5T_5. Thus $H_{10}T_5$ would produce significantly better dispersions compared to H_5T_5.

7.3.3 Structural Origin of the Barrier

To enable an informed optimization process of the repulsive barrier it is essential that its structural origin is understood in detail. By inspecting the snapshot in Fig. 7.3(a) it is immediately obvious that the adsorbed phase of H_5T_5 consists of micelles reminiscent of the sperical micelles the surfactant forms in the bulk. The cluster size distribution in Fig.7.9(a) indicates that the average aggregation number of the adsorbed micelles $\overline{N}_{ads} \approx 50$ is somewhat larger then the bulk value of $\overline{N}_{bulk} \approx 41$. The distinct tail in the cluster size distribution in Fig. 7.9 (a) and the secondary maximum at $N \approx 100$ are caused by occational connections between neighboring adsorbed micelles. As indicated by the $1D$ micelle/micelle correlation function in Fig. 7.9(b) the adsorbed micelles are correlated along the tubes. The origin of the correlation is the competition between adsorption trying to increase the number of adsorbed micelles and micelle/micelle repulsion trying to increase the distance between adsorbed micelles. The average distance between neighbooring H_5T_5 adsorbed micelles is given by the position of the first maximum in the correlation curve $\overline{l} = 16$. The curious "secondary peaks" in Fig. 7.9(b) located at distances $l = \overline{l} + 1/2 \cdot \overline{l} \approx 24$ and $l = 2\overline{l} + 1/2 \cdot \overline{l} \approx 42$ are caused by the random connections between adsorbed micelles of the H_5T_5 surfctant. As two connecting micelles are considered to be one aggregate the center of mass of the "new" aggregate is located halfway between the two original micelles. Since these connections are not too frequent, the respective peaks in Fig. 7.9(b) are weaker than the primary peaks.

Also $H_{10}T_5$ forms adsorbed spherical micelles. However, they have a smaller aggregation number of $\overline{N}_{ads} \approx 30$ which is identical to the bulk value $\overline{N}_{ads} = \overline{N}_{bulk}$ adsorbed micelles rarely connect to their neighbours illustrated by the much less pronouced tail in the cluster size distribution (Fig. 7.9 (a)) and the lack of secondary peaks in g_l (Fig. 7.9(b)).

At this point we shall note that our box size is too small to avoid finite size effects. Clearly, the micelle/micelle correlation function in Fig. 7.9(b) does not decay within the simulation box. To quantify the impact of this finite size effect we have studied the system at tube/tube distance of $d = 7.10$ varying the relevant box dimensions in several steps by up to $\overline{l}$ which should make any finite size effects apparent. Increasing the box size by $\approx 14\sigma$ leads to an increase in the adsorbed amount but no change in the number of aggregates, i.e micelles grow from $\overline{N} = 30$ to $\overline{N} = 35$. Further increase led to an increase of the number of adsorbed aggregates by 2 (one one each tube) and a reduction of the aggregate size to $\overline{N} \approx 30$. Most importantly the surfactant mediated tube/tube force was unaltered , i.e no change beyond the expected sampling error of $\approx 10\%$ was observed. Thus, finite size effects on the forces seem to be insignificant. We also like to remark that the confinement effect imposed by the periodicity of the system might occur naturally in dense systems where a CNT might be contacted by other tubes at several points along the tube.

As expected, at very large separations between the tubes where adsorbed molecules do not interact with molecules adsorbed on the other tube, we do not observe any correlation between the position of the crossing and the position of the micelles (Fig. 7.10 green curve) consequently micelles are mutually correlated (Fig. 7.9(b)) but otherwise free to move along the tubes. As the distance between the tubes is reduced and their surfactant coatings start to interact, the lateral density $\rho_l(l)$ shown in Fig. 7.10(a) changes dramatically. The most striking effect is that micelles close to the crossing are no longer free to move but get pinned indicated by the peaks in $\rho_l(l)$. Their position is now correlated with the position of the crossing located at $l = 0$. Simultaneously the density plot indicates that micelles largely avoid the crossing. This is also illustrated by the representative snapshot in Fig. 7.10 (b).

A more subtle but critical effect is that the distance between the pair of micelles closest to the crossing ($l \approx 19$) is considerably larger than the equilibrium distance of the

undisturbed structure ($l \approx 16$). Thus, the correlated micellar structure does not only get pinned but micelles are repelled from the crossing. The repulsion is caused by head/head repulsion between micelles adsorbed on different tubes. As a consequence, the head density at the crossing is reduced (Fig. 7.11(a)) relieving some of the repulsive forces between the surfactant covered tubes at the crossing.

However, the distance between the innermost micelles is not large enough to avoid repulsive interactions completely. The overlap density in Fig 7.11(b) clearly shows that there is a deformed torus around the crossing where head groups overlap.

The repulsive forces resulting from this overlap can sustain a repulsive force pushing the inner micelles further away from the crossing. In order for the inner micelles to move away from the crossing the other adsorbed micelles would have to make room. An extreme possibility would be desorption of a complete micelle. This is not the case, however, as comparison of Figs. 7.9(b) and 7.10(a) reveals, i.e. six micelles are adsorbed whether the tubes are far apart or close together. This might not surprise as the adsorption energy is fairly large. The required space at the crossing is instead provided by compression of the remaining adsorbed phase, i.e. micelles move closer together as the 1D density in Fig. 7.10(a) shows. The distance between micelles, except at the crossing, is now 14 instead of 16

A near identical structure is observed for $H_{10}T_5$. However the longer head groups of $H_{10}T_5$ require more space at the crossing (Fig. 7.10(a)). This leads to stronger compression of the adsorbed micellar phase compared to the H_5T_5 system. This stronger compression must be expected to be the origin of the larger tube/tube repulsion because it is the only force that keeps the inner micelles from moving away from the crossing.

From these observations we conclude that longer head groups and a lower lateral compressibility of the adsorbed phase should lead to a larger repulsive barrier.Our results suggest, the larger heads lead to a longer range of the repulsive force and the lower compressibility leads to a higher magnitude of the force.

7.3.4 The Hysteresis in the Force Curve

Inspection of the force curves in Figs. 7.4(b) and (c) clearly reveals strong hysteresis for the transitions between the repulsive and the attractive regime. For a single crossing this hysteresis closely resembles a first-order phase transition but lacks the required scaling with system size.In the simulations this scaling with system size is artificially created through the periodic boundary conditions. The transition is essentially morphological and causes only an insignificant change in the adsorbed amount of less than 10 molecules. In the attractive state a central micelle connects both tubes (Fig. 7.12 (a)), while in the repulsive state the it is replaced by two new micelles, one adsorbed on each tube (Fig. 7.12 (c)).

For the transition from the attractive to the repulsive regime the central aggregate has to be destroyed. As the adsorbed amount is essentially constant during this process and because of the symmetry of the system one expects that the central aggregate is split into two fragments, each one remaining on a different tube. However, this process can occur only if the resulting fragments are large enough to be stable. At the relevant tube/tube distances the aggregation number of the central aggregate is approximately 20 leading to two fragments of approximately 10 surfactant molecules. Comparison with the cluster size distributions in Fig. 7.9 (a) reveals that adsorbed clusters of this size are too small to be stable. Thus, rupture of the central aggregated can occur only if more molecules are involved in the process.

Studying many rupturing events revealed that the process is initiated by simultaneous extrusion of an extension towards the central aggregate by neighboring inner micelles on both sides of the central aggregate. This forms a complex of three aggregates which then ruptures near the center of the crossing, where the central aggregate has been, forming two very big aggregates - one on each of the tubes. Subsequently, each of these big aggregates ruptures into two normal size aggregates. After and also during this process molecules are exchanged with the other adsorbed micelles until a new equilibrium is reached. Interestingly, in the attractive state adsorbed micelles are in average 5 chains larger than in the repulsive region ($\overline{N}_{ads} \approx 30$) and in the case of isolated tubes ($\overline{N}_{ads} \approx 30$). This is consistent with our finite size analysis in Sec. 7.3.2 and seems to be a consequence of the reduced compression of the adsorbed phase in the attractive state caused by the reduced space requirement of the central aggregate

compared to a ”regular” adsorbed micelle.

The hysteretic nature of the transition has also consequences for rebundling, as it involves a transition of the system from the repulsive to the attractive state. This requires sufficient approach of the two tubes and therefore, overcoming of the ”approach barrier” discussed in Sec. 3.2. This is necessary but not sufficient to reach the attractive state as the hysteresis indicates that another barrier separating the repulsive and the attractive states exists, which has to be overcome as well. Thus, the true barrier, i.e. the actual activation energy for rebundling is the sum of the ”approach barrier” and the barrier of the hysteretic force at the respective tube/tube distance.

The barrier associated with the hysteretic force cannot be determined within the present simulation framework. However, the transition from the repulsive to the attractive region is thermally activated as is overcoming the approach barrier and this is the case in the actual CNT suspension and in the present simulation system. For both surfactants we observe that only very near the end of the repulsive branch the system jumps to the attractive branch and does not return. This indicates that only in this very small region the thermal energy is large enough to activate the transition. As the temperature is the same for both systems it can be concluded that at the tube/tube distance where the two systems jump from the repulsive to the attractive regime the barriers are similar. This indicates that it is the approach barrier that discriminates between the two systems. In other words, the two systems require different amounts of energy to reach the tube/tube distance where the transition occurs and approximately equal amounts to activate the transition. Because the activation energy is additive eq. (7.13) factorizes and the conclusions about the relative rebundling rate in Sec. 7.3.2 hold.

7.3.5 Conclusions

We have used DPD simulations of a coarse grain surfactant model to study the rebundling of a pair of surfactant coated and perpendicular CNTs. By detailed analysis of the shielding mechanism we are able to identify the key parameters that influence the surfactants shielding efficiency. We have used two surfactants with different head group length both of which self-assemble into spherical micelles in the bulk and on the tubes.

As the distance between the pair of surfactant coated CNTs is reduced the surfactant mediated tube/tube force changes sign from attractive to repulsive. In the two systems studied this transition is first order but it would lead to a hysteric force even for a single crossing. Reaching of the attractive regime is necessary for rebundling. Thus, suspensions are stabilized if this can be prevented. Rebundling can be viewed as a thermally activated process where in the present simulation system the barrier is the sum of the approach barrier and the transition barrier. The transition barrier cannot be determined within the present simulation framework but it can be argued that it is very similar for the two surfactants (see Sec. 7.3.3).

The approach barrier is the integral of the repulsive surfactant mediated tube/tube force. We found that longer head groups lead to a surfactant mediated repulsive tube/tube force that is (i) longer ranged and (ii) stronger. Both effects result in a larger rebundling barrier. The longer head groups cause a longer range of the force as these molecules form an absorbed phase with a further reaching head corona. This leads to overlap of the head coronas of a rebundling tube pair at larger distances. The larger magnitude of the surfactant mediated force appears to be a consequence of the larger compressive forces the adsorbed phase can sustain. This compressive force is the only force preventing surfactant molecules to leave the overlap region near the crossing where the surfactant mediated tube/tube force originates.

This results in a small but distinct difference in the rebundling barrier of the two surfactants of 2.5kT. Critically, this difference leads to a 10-fold lower rebundling rate of the surfactant with the larger head groups. This indicates a significantly better dispersion stability for the surfactant with the larger head group.

Although the length of the head group might be an interesting control parameter, it is the magnitude of compressive force the adsorbed phase can sustain along the tube axis that appears to limit the repulsive tube/tube force. This suggests that the morphology of the adsorbed phase is the critical factor.

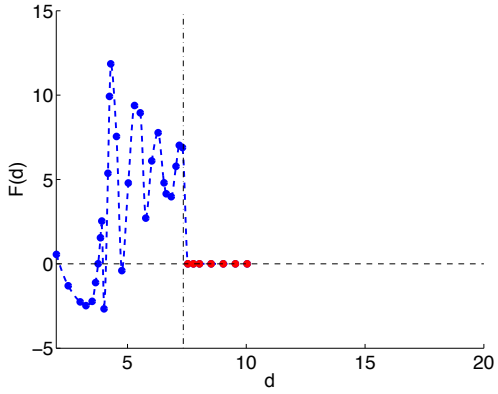

(a) H_5T_5, $C \approx CSAC$

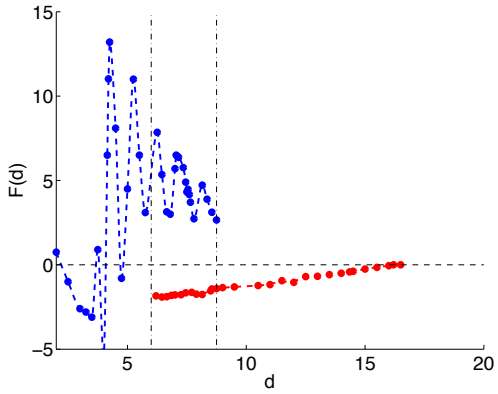

(b) H_5T_5, $C \approx CMC$

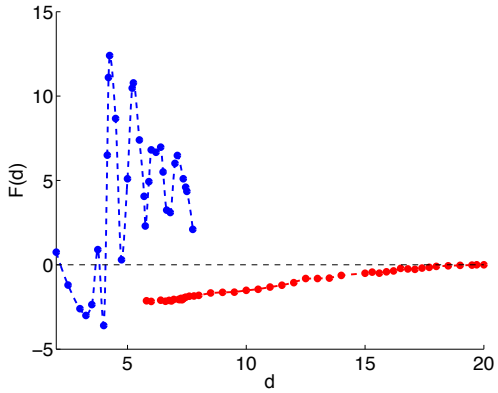

(c) $H_{10}T_5$, $C \approx CMC$

Figure 7.4: Force-distance curves for the surfactant mediated force between a pair of perpendicular carbon nanotubes: (a) H_5T_5 at low concentration $C \approx 0.2 \cdot CMC$ (data taken from Ref.[64]), (b) H_5T_5 at $C \approx CMC$ and (c) $H_{10}T_5$ at $C \approx CMC$. For the two systems at the CMC (part (b) and (c)) we find pronounced hysteresis between the attractive (blue) and repulsive branch (red). Note that at low concentrations (part (a)) the repulsive region is replaced by a regime with vanishing force (red) as at large distances no aggregation occurs on the tubes; possible hysteresis has not been investigated for this case.

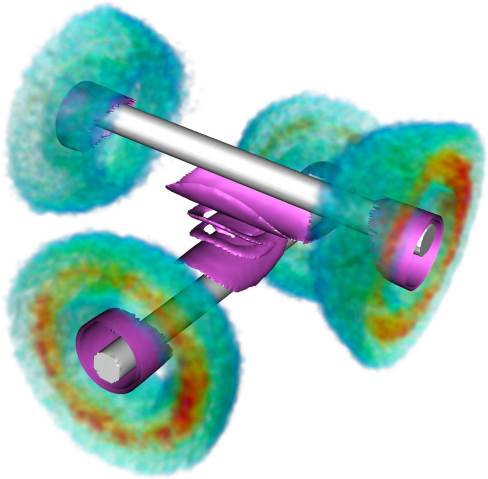

Figure 7.5: Internal structure of a H_5T_5 system in the attractive region at $d = 6.20$. The local density of tail beads is shown by the (purple) isosurfaces at $\rho^T = 0.8$. Clearly visible is the central aggreagte with its layered structure. The central aggregate is surrounded by four adsorbed micelles. The local density of the head beads of these micelles is shown as a color coded cloud. Blue indicates the lowest density $\rho^H_{min} = 0.002$ and red the highest density $\rho^H_{max} = 0.2$. Between these two values the jet color code is used. As neither tail nor head density of the inner most adsorbed micelles overlap they don't contribute to the surfactant mediated tube/tube interaction. The head density of the central aggregate is not shown for clarity.

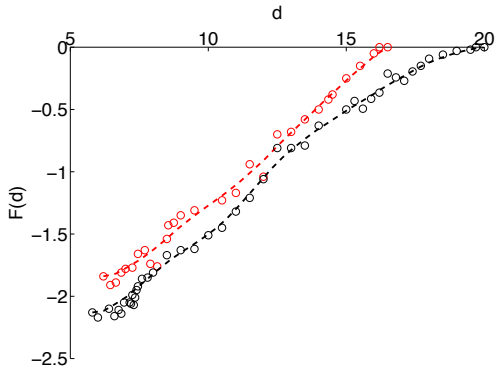

Figure 7.6: Comparison of the repulsive regions of the force distance curves (Fig. 7.4) for H_5T_5 (red) and $H_{10}T_5$ (black): Lines are a guide to the eye. The longer head groups of $H_{10}T_5$ lead to a longer ranged force of higher magnitude compared to H_5T_5.

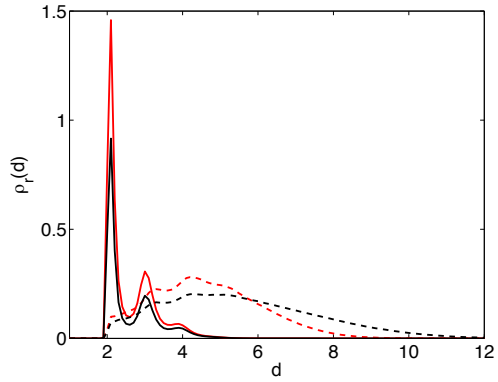

Figure 7.7: Average structure of the adsorbed phase of H_5T_5 (red) and $H_{10}T_5$ (black) on isolated tubes as the radial density of head (dashed lines) and tail beads (solid lines) as defined in eq. (7.9). The head density shows that the longer heads of $H_{10}T_5$ reach futher away from the tubes. Note that the adsorbed phase is inhomogeneous in the lateral direction over which is averaged here (Fig. 7.3).

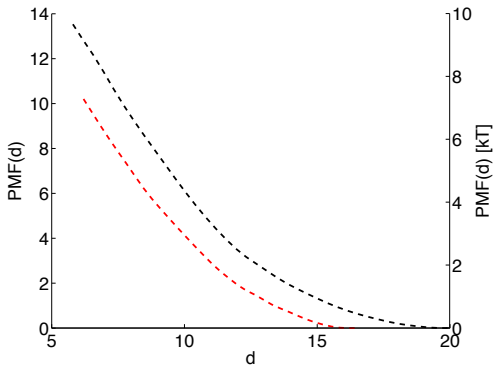

Figure 7.8: The potential of mean force (PMF) versus distance d for the two different surfactants: $H_{10}T_5$ (red) and H_5T_5 (blue). The PMF of $H_{10}T_5$ is longer ranged and larger in magnitude.

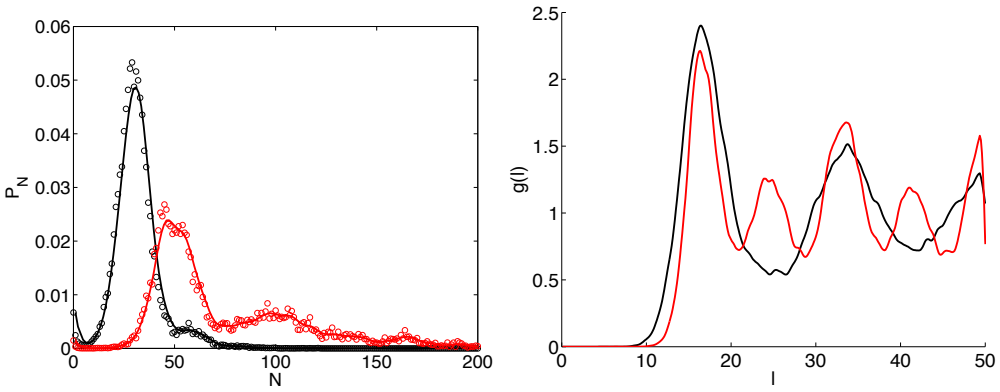

(a) (b)

Figure 7.9: Structure of the micellar adsorbed phase of H_5T_5 (red) and $H_{10}T_5$ (black) on independent isolated tubes. (a) Cluster size distribution as the probability mass function P_N versus cluster size N. (b) $1D$ micelle/micelle correlation function along the tubes $g_{ads}(r)$ versus the micelle/micelle distance r, where the position of a micelle is the projection of its center of mass onto the tube axis. Adsorbed micelles of H_5T_5 frequently connect leading to the secondary maximum in P_N at twice the mean aggregation number and to the secondary maxima halfway between the primary maximum in $g_{ads}(r)$.

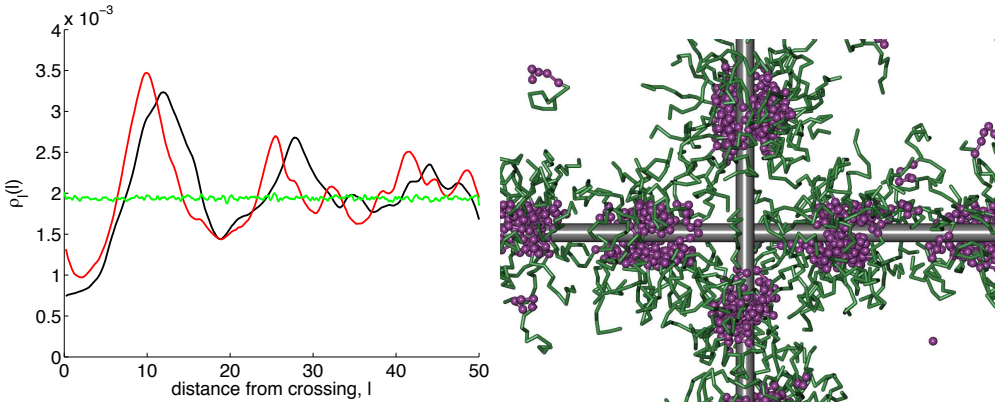

(a) (b)

Figure 7.10: (a) $1D$ (one-particle) density of micelles adsorbed along the tubes $\rho_l(l)$ as defined in eq.(7.10), where the position of a micelle is the projection of its center of mass onto the tube axis. The origin ($l = 0$) is chosen to be the center of the crossing. At large distances between tubes ($H_{10}T_5, d = 18.10$, green curve) micelles are free to move along the tubes. At close distances ($d = 6.95$) the crossing is depleted and the structure get pinned: H_5T_5 (red) and $H_{10}T_5$ (black). (b) Snapshot of the H_5T_5 system at $d = 6.95$ indicating the depletion of the crossing and the pinning of four "inner" micelles surrounding it.

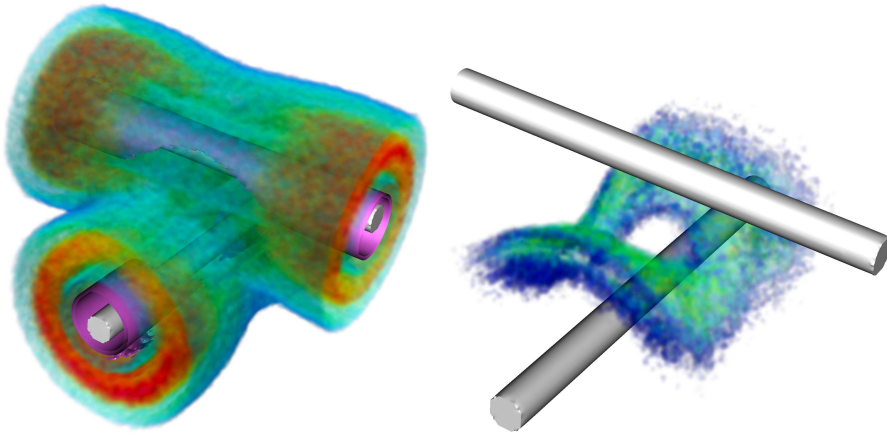

(a) (b)

Figure 7.11: Structure of the overlap region of $H_{10}T_5$ in the repulsive regime. (a) Local head and tail bead densities as in Fig.7.5. Clearly visible is the depletion of head groups near the crossing. (b) Local density of repulsive contacts (per time step) between head groups of molecules adsorbed on different tubes. Color code is the same as in Fig. 7.5

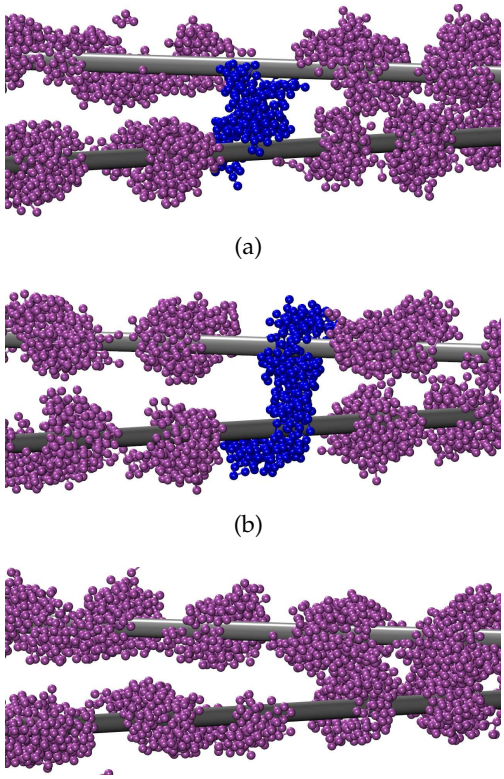

(a)

(b)

(c)

Figure 7.12: Snapshots illustrating the transition between the attractive and the repulsive regime at $d = 8.15$ for $H_{10}T_5$. Purple beads indicate hydrophobic beads, hydrophilic beads have been omitted for clarity. (a) Attractive state with central aggregate (blue beads), (b) Transition state consisting of a complex of three aggregates just before rupture (protrusions from micelles adjacent to the junction and central aggreagate in blue), (c) Repulsive state with no central aggregate.

CHAPTER 8

Dispersing Individual Single-Wall Carbon Nanotubes in Aqueous Surfactant Solutions below the cmc

Dispersing Individual Single-Wall Carbon Nanotubes in Aqueous Surfactant Solutions below the cmc

Panagiotis Angelikopoulos,[†] Andrei Gromov,*[,‡] Ailsa Leen,[‡,§] Oleg Nerushev,[‡] Henry Bock,*[,†] and Eleanor E. B. Campbell[‡,||]

Department of Chemical Engineering, Heriot-Watt University, Edinburgh, EH14 4AS, U.K., School of Chemistry, University of Edinburgh, Edinburgh, EH9 3JJ, U.K., and Mary Erskine School, Edinburgh EH4 3NT, U.K.

Received: June 24, 2009; Revised Manuscript Received: September 22, 2009

Dispersions of single-wall carbon nanotubes (SWCNTs) in surfactant solutions below the critical micelle concentration (cmc) have been studied theoretically and experimentally. Dissipative particle dynamics (DPD) simulations of a coarse-grained model predict that surfactant adsorption on small diameter tubes is dominated by aggregation of the surfactant molecules into adsorbed micelles at $C \approx 0.3C_{cmc}$. We also find that the surfactant adsorption is nearly complete at a concentration of around $C \approx 0.5C_{cmc}$. Further increase of the surfactant concentration has only minor effects on the radial density of surfactant headgroups, indicating that SWCNT may be fully stabilized in solutions below the cmc. SWCNT dispersions in solutions of anionic surfactants sodium dodecyl sulfate (SDS) and sodium dodecylbenzenesulfonate (SDBS) below the cmc show a significant fraction of dispersed individual tubes and small bundles, in agreement with the model calculations.

Introduction

Preparation of high-concentration stable dispersions of debundled carbon nanotubes (CNTs) is an important challenge for a number of current and potential applications of CNTs, e.g., mechanical reinforcement of polymer[1,2] and metal[3] matrices, development of conducting polymeric materials,[4−6] improvement of thermal conductivity of composites,[7−12] etc. Also, dispersion of individual nanotubes is indispensable for separation of SWCNT according to their electronic properties.[13−18]

However, due to strong van der Waals forces, carbon nanotubes tend to form bundles. The general approach for producing dispersions of unbundled nonfunctionalized CNTs includes splitting bundles by input of energy (e.g., ultrasonication) in the presence of a stabilizing agent which would prevent reagglomeration of the CNTs into bundles. Different classes of stabilizing agents have been used such as (i) aqueous solutions of numerous surfactants;[19−24] (ii) solutions of synthetic[25−30] and biopolymers[31−37] in appropriate solvents (in this case stabilization of CNTs in solution proceeds due to polymer wrapping around the tube along its axis); and (iii) ionic liquids and solutions of organic salts.[38−40] Recently, it was also shown that a significant degree of dispersion can be achieved by spontaneous debundling in common organic solvents such as *N*-methyl-2-pyrrolidone[41] and γ-butyrolactone.[42] Covalent functionalization also may be used to facilitate the dispersion of CNTs.[43−50] It must, however, be taken into account that sidewall functionalization of SWCNT changes their properties.[51−57]

For preparation of stable dispersions with relatively high concentrations of CNTs it is generally recommended in the literature to use surfactant concentrations equal to several critical micelle concentration (cmc) values.[22,23,58−61] Even at the optimum concentration of surfactants, dispersions with a large fraction of individual SWCNT have only been reported for low concentrations of SWCNT. There are only a few publications where CNT dispersions in surfactant solutions with concentrations close to or below cmc were reported,[59,60,62,63] although, without much emphasis on the properties of such dispersions.

Whether surfactant adsorption on CNTs leads to their dispersion or not clearly depends on the adsorbed amount and possibly also on the adsorbed structures. Both are difficult to access experimentally but are available through computer simulations. This potential of molecular simulations is demonstrated by a number of recent studies. In their coarse grained molecular dynamics (CGMD) simulations Shvartzman-Cohen et al.[64] found that amphiphilic block-copolymers of the Pluronic family form adsorbed random structures on CNTs. Wallace et al.[65,66] used CGMD to investigate adsorption of DPPC (dipalmitoylphosphatidylcholine) and DHPC (dihexanoylphosphatidylcholine) phospholipids and zwitterionic detergent LPC (lysophosphatidylcholine) on CNTs. They found a variety of adsorbed structures including randomly arranged surfactant molecules and encapsulation by spherical and cylindrical micelles, which depend on the type of amphiphile as well as the number of surfactant molecules in the simulation box. Tummala et al.[67] used fully atomistic MD to show that the aggregation morphology of sodium dodecyl sulfate (SDS) molecules on SWCNTs is influenced by the tube diameter, its chirality and the number of SDS molecules placed in the simulation box. Specifically, they find an increase in the adsorbed amount and variation from "rings" of SDS molecules lying flat on the tube surfaces and parallel to the tube axis to adsorbed micelles with disordered internal structure when the number of surfactants in the simulation box was increased.

Patel et al.[68] studied the dispersion of two parallel nanotubes with the surfactant DTMAC (*n*-decyltrimethylammonium chloride) using 2D density functional theory and a coarse-grained model with implicit solvent. Their results indicate that SWCNT

* Corresponding authors. E-mail: h.bock@hw.ac.uk (H.B.); a.v.gromov@ed.ac.uk (A.G.).
[†] Heriot-Watt University.
[‡] University of Edinburgh.
[§] Mary Erskine School.
[||] Also at Division of Quantum Phases and Devices, Konkuk University, Seoul 143-701, Korea.

10.1021/jp905925r
Published on Web 12/11/2009

dispersions may occur below the cmc, since the surfactant-mediated force overcomes the direct SWCNT−SWCNT attraction. This conclusion was drawn by studying the system below the experimental cmc, thus, not taking into account likely deviations of the model cmc compared to the bulk cmc.

While these studies demonstrate a dependence of the adsorbed amount and the adsorbed structures on the number of molecules in the simulation box, concentration control has not been achieved. Consequently, knowledge and understanding of the concentration dependence of surfactant adsorption on CNTs is still lacking. This, however, is essential for the interpretation of experimental findings as well as the optimization of technical processes and applications.

Here we report on the preparation of stable aqueous dispersions with increased fraction of individual SWCNT in anionic surfactant solutions below the cmc. In the simulation part of this paper we use dissipative particle dynamics (DPD) and a coarse-grained surfactant model to investigate the concentration dependence of surfactant adsorption on CNTs. Specifically, we study the adsorbed amount and the adsorbed structures. Using the bulk cmc as a reference, we find good agreement between the experimental and the simulation results. In particular, the dispersion of CNTs below the cmc is demonstrated and explained.

Experimental and Simulation Methods

Experiments. Typically 1 mg of SWCNTs (as produced HiPco[69] tubes from Carbon Nanotechnologies Inc., USA) was dispersed in 10 mL of surfactant solution (concentration of SWCNTs, $c_{CNT} = 0.1$ mg/mL). The following surfactant solutions were used (see Table 2): SDS (sodium dodecyl sulfate, cmc_{SDS} value in water is 2.4 mg/mL[70,71]): 10 mg/mL, ∼4 cmc (further denoted as SDS10); 3 mg/mL, ∼1.2 cmc (further denoted as SDS3); 1 mg/mL, ∼0.4 cmc (further denoted as SDS1); and 0.5 mg/mL, ∼0.2 cmc (further denoted as SDS05); SDBS (sodium dodecylbenzenesulfonate, cmc_{SDBS} value in water is 0.35 mg/mL[60]): 10 mg/mL, ∼30 cmc (further denoted as SDBS10); 3 mg/mL, 8−9 cmc further denoted as (SDBS3), 1 mg/mL, ∼3 cmc (further denoted as SDBS1); and 0.2 mg/mL, ∼0.6 cmc (further denoted as SDBS02).

The dispersions were sonicated with an ultrasonic tip (*Bandelin Sonoplus* ultrasonic homogenizer HD 2200 with titanium tip KE76 with a diameter of 6 mm) in plastic test tubes at an average power of 20 W for 6−7 min (in 1 min periods in order not to overheat the sample) while cooling in an ice bath. Subsequently, the dispersions were centrifuged for 2 × 30 min at 20 500*g*. The supernatant fraction of each dispersion was analyzed by AFM. As there was always some precipitant visible, the actual concentrations of SWCNTs in the supernatant were always lower than the original 0.1 mg/mL.

AFM measurements were performed using a Veeco DI NanoMan VS instrument in tapping mode. For preparation of samples for AFM a piece of polished Si wafer, surface modified with (3-aminopropyl)triethoxysilane for better adhesion of SWCNT,[72−74] was completely covered with the supernatant part of the SWCNT dispersion and left for 3 h in saturated water vapor environment for prevention of liquid evaporation. Then the substrate was rinsed in distilled water and blown dry with nitrogen gas.

The concentrations of SWCNT in the original dispersions and the dispersions after centrifugation were evaluated by Raman spectroscopy. A Renishaw InVia Raman confocal microscope with an excitation energy of 2.41 eV was used for the Raman studies. The dispersions were analyzed through a 90 μm thick glass slide using backscattering geometry and a laser power of 3 mW.

TABLE 1: Simulation Parameters in Reduced Units

Surfactants	
no. of T-beads = 5	no. of H-beads = 5
$\varepsilon = 1.0$	$\sigma = 1.0$
attractive: $r_{cut} = 2.5$	repulsive: $r_{cut} = \sqrt[6]{2}$
$\varepsilon_{bond} = 4.0$	$\sigma_{bond} = 1.2$
Nanotubes	
$r_{CNT} = 1.0$	$\varepsilon_{CNT} = 2.5$
Simulation	
$T = 0.7$	$\Delta t = 0.005$
nonconservative: $r_{cut} = 2.5$	$\xi = 1$
equilibration = $10^8 \Delta t$	production = $10^8 \Delta t$

Simulations. ***Model.*** The simulation method and the model employed in this study have been used and discussed in detail before[75] and therefore we confine this section to a brief overview. The surfactant molecules used in this study (H_5T_5) are represented as chains of five hydrophilic head (H) beads followed by five hydrophobic tail (T) beads. The solvent is treated implicitly. The beads interact via effective potentials due to the coarse-grained character of the surfactant beads along with the implicit representation of the solvent. In this study, we employ a common empirical model where the interaction between hydrophobic beads is attractive, while all other bead/bead interactions are repulsive. The force shifted Lennard-Jones (LJ) (12,6) potential ϕ_{ij} is used to represent attractive interactions between beads i and j:

$$\phi(r_{ij}) = \begin{cases} \phi_{LJ(r_{ij})} + \phi'_{LJ}(r_{cut})(r_{ij} - r_c) - \phi_{LJ}(r_{cut}) & r_{ij} < r_{cut} \\ 0 & r_{ij} \geq r_{cut} \end{cases}$$

$$\phi_{LJ(r_{ij})} = 4\varepsilon\left[\left(\frac{\sigma}{r_{ij}}\right)^{12} - \left(\frac{\sigma}{r_{ij}}\right)^{6}\right] \quad (1)$$

where $\phi'_{LJ}(r) = d\phi_{LJ}/dr$ and r_{cut} is the cutoff radius. In eq 1 ε and δ are the well depth and the length parameter of the LJ potential, respectively, $r_{ij} = ||\boldsymbol{r}_{ij}||$, $\boldsymbol{r}_{ij} = \boldsymbol{r}_j - \boldsymbol{r}_i$, and $\mathbf{r}_i$ and $\mathbf{r}_j$ are the positions of beads i and j, respectively. Repulsive interactions are modeled using the WCA potential given by eq 1 with

$$r_{cut} = \sqrt[6]{2}$$

Beads k and l which are nearest neighbors in a chain interact via the bead/bead potentials and, additionally, via a quadratic harmonic bond potential

$$\phi_{bond}(r_{kl}) = \varepsilon_{bond}(r_{kl} - \sigma_{bond})^2 \quad (2)$$

where ε_{bond} and σ_{bond} are the well depth and the bond length, respectively.

At the level of coarse graining of the surfactant molecules, CNTs can be regarded as smooth cylinders. Their interactions with surfactant beads are modeled via the force shifted Lennard-Jones (12,6) potential in eq 1 which is also shifted to the surface of the nanotubes

$$\phi_{CNT}(r_i) = \varepsilon_{CNT}\phi(r_i - r_{CNT}) \quad (3)$$

where r_i is the shortest distance[76] between bead i and the nanotube axis and r_{CNT} is the radius of the nanotube. All simulation parameters are summarized in Table 1.

Simulation Methodology. We investigate the system in the canonical ensemble using the dissipative particle dynamics

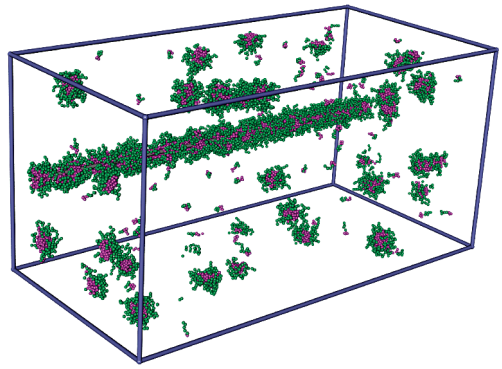

Figure 1. Simulation snapshot showing the simulation box ($100\sigma \times 100\sigma \times 200\sigma$) and the system above the cmc.

(DPD) method.[77] In DPD any two particles i and j interact via a pair wise force $F_{ij} = F^{C}_{ij} + F^{R}_{ij} + F^{D}_{ij}$ where F^{C}_{ij}, F^{R}_{ij}, and F^{D}_{ij} are the conservative, the random, and the dissipative force, respectively. The conservative force is given by the derivative of the potentials discussed above. As the random and dissipative forces should not affect the equilibrium results we chose them to be the same as the ones commonly used in most studies (e.g., refs 75 and 78).

The simulation box is large which allows us to determine and control the bulk surfactant concentration (Figure 1). To determine the bulk concentration, a slice of the system of 50σ width centered at the tube axis in the x-direction (perpendicular to the tube axis) was excluded. The remaining volume is considered bulklike. The size of the simulation box was chosen such that there were typically 200 chains in the bulk control volume but no less than 40 in uncritical cases and no less than 160 chains adsorbed. The concentration is adjusted in the initial part of the equilibration period by insertion and deletion of surfactant molecules if the actual concentration in the bulklike region deviates by more than 5% from the target. The usual periodic boundary conditions are also employed.

Reduced Units. When describing the simulations, we use reduced quantities: lengths are given in units of the LJ length parameter σ, the energy is scaled with the well depth of the bead/bead LJ interaction ε, the temperature scale is given in terms of ε/k_B, and time is represented in units of $[m\sigma^2/\varepsilon]^{1/2}$, where m is the mass of a bead. Concentrations are defined as molecular number densities and given in units of $1/\sigma^3$.

Results and Discussion

Computer Simulations. Here we study adsorption of the model surfactant H_5T_5 with 5 hydrophilic head beads (H) and 5 hydrophobic tail beads (T) on a SWCNT. We have determined the cmc of this model surfactant in an earlier publication[75] and at a reduced temperature of $T = 0.7$ found $C_{cmc} = 5.2 \times 10^{-5}$. We observed a rather sharp transition from $C_1 = C$ to $C_1 =$ constant at the cmc, where C_1 is the concentration of free surfactant molecules. This allowed us to define the cmc to be the center of the very small transition region between the two domains.[75] For the further discussion it is interesting to note that this model surfactant forms spherical micelles of approximately 41 chains in bulk solution.

Adsorption of Surfactants on Single-Wall Nanotubes. We investigate adsorption of surfactants on SWCNTs using the bulk concentration as the control parameter (Figure 2). At low concentrations, the number of adsorbed surfactant molecules increases linearly with increasing concentration (Figure 2b). We then observe a steep increase in the adsorbed amount around $C = 2.0 \times 10^{-5}$. Any further increase in the concentration leads to only a very slight increase in the number of adsorbed chains. (Observe the logarithmic concentration scale.) Thus, adsorption is nearly complete at a concentration significantly smaller than the cmc, i.e., around $C \approx 0.5C_{cmc}$. Evidently, the leveling off of the adsorbed amount is associated with saturating the surfaces rather than with reaching the bulk cmc as in the case of adsorption on hydrophilic surfaces (e.g., refs 79 and 80).

The initial linear region, $C < 0.6 \times 10^{-5}$, is consistent with adsorption of individual molecules in the Henry's law regime. The evidence for adsorption of individual molecules is provided by the respective cluster size distribution in Figure 3. The cluster size distributions are defined here as the (canonical ensemble average of the) probability mass function, i.e., the probability that an adsorbed chain belongs to a cluster of aggregation number N

$$P(N) = \left\langle \frac{Nn_N}{\sum_{N=1}^{\infty} Nn_N} \right\rangle \tag{4}$$

where n_N is the instantaneous number of clusters of size N adsorbed on the CNT and $\langle \cdots \rangle$ denotes the canonical ensemble average. At $C = 0.51 \times 10^{-5}$, $P(N)$ in Figure 3 decays steeply, thus demonstrating that at very low surfactant concentrations adsorption is dominated by individual surfactant molecules.

As the bulk concentration increases, the adsorbed amount increases faster than linear. This superlinear increase is a clear sign of cooperative adsorption. At these still low concentrations cluster size distributions ($P(N)$ for $C = 1.35 \times 10^{-5}$ in Figure 3) still decay exponentially indicating the formation of (small) clusters of no preferred size (Figure 4a). Clusters in this regime form statistically and, thus, grow in size with increasing concentration.

As the concentration increases above a certain threshold, a shoulder appears in P(N) (Figure 3, $C = 1.49 \times 10^{-5}$). This shoulder is indicative of the formation of clusters of preferred size, that is, surfactant aggregation on the CNT. These adsorbed aggregates are clearly visible in the snapshot in Figure 4b. At even higher concentrations, the shoulder has developed into a well-defined local maximum (Figure 3, $C = 2.39 \times 10^{-5}$). This indicates that adsorption is now dominated by adsorbed micelles (Figure 4c−e). The concentration where this maximum first appears is often used as a reference point for surface aggregation called critical surface aggregation concentration (CSAC). In the present case $C_{CSAC} \approx 1.5 \times 10^{-5} \approx 0.3C_{cmc}$. This surface aggregation causes the adsorbed amount to increases steeply and faster than in the initial linear regime (Figure 2). Thus, surface aggregation dominates surfactant adsorption on the small diameter tube studied here.

At concentrations immediately above the CSAC, aggregates have a size of about 13 surfactant molecules. This is significantly smaller than the aggregation number of bulk micelles which is approximately 41. As the bulk concentration increases, the aggregate size increases up to approximately 45 at $C = 33.1 \times 10^{-5}$. Moreover, at concentrations beyond $C \approx 2 \times 10^{-5}$, cluster size distributions have a tail at large cluster sizes which is caused by temporary connection of two or more clusters. This tail grows with increasing concentration. At the highest concentrations the tail has maxima at integer multiples of the position of the first peak implying the connection of two or more adsorbed micelles (Figure 4c,d).

A final remark on the relevance of the simulation results for the interpretation of the experimental measurements is appropri-

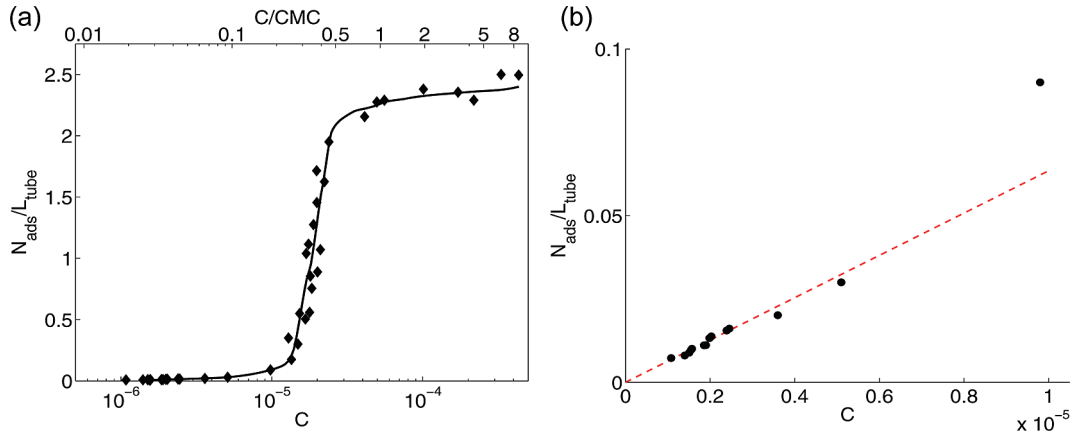

Figure 2. Adsorption isotherm as number of adsorbed molecules per tube length N_{ads}/L_{tube} versus bulk surfactant concentration: (a) complete isotherm and (b) magnification of the low coverage regime. The solid line in part (a) is a guide to the eye, and the dashed line in part (b) is a linear fit to the results for $C < 0.6 \times 10^{-5}$.

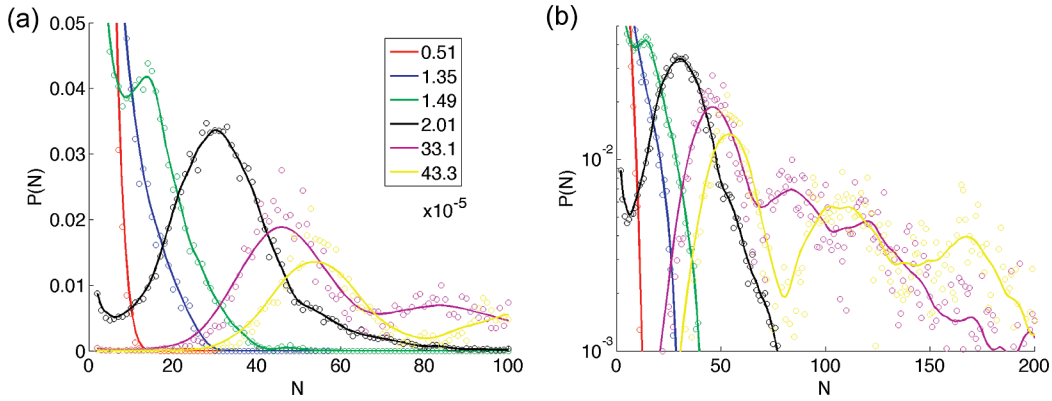

Figure 3. Cluster size distributions at six different concentrations as indicated in part a: (a) linear N scale and (b) logarithmic N scale to emphasize the tails at large concentrations.

ate. It must be expected that the adsorbed self-assembled structures depend on the diameter of the CNTs.[67,81] Clearly, if the tube diameter is very large, adsorption of concentric micelles, as shown in Figure 4d,e is not possible. Although very little is known about this, the tube diameter is likely to influence the adsorption isotherm.

However, in the experiments we are using single-wall CNTs where the overwhelming majority of tubes has diameters between 0.7 and 1.4 nm.[82] Typical bulk micelles of the two surfactants used in this study, SDS and SDBS, have diameters of ~4 nm[83] and ~6 nm,[84] respectively. Thus, the diameters of the SWCNTs in the sample are significantly smaller than the diameter of the (bulk) micelles. This situation is well reproduced by our model where the tube diameter is 2 and the diameter of the hydrophobic core of the micelles is ~4.6.[75] Therefore, it appears reasonable to assume that adsorption in the experimental system results in structures which are similar to the ones we find in the model system. Consequently, it is also reasonable to make a qualitative comparison between the model and the experimental system.

Stabilization of CNT Suspensions by Surfactants. Steric repulsion between the head groups of surfactant molecules adsorbed onto different tubes generates a barrier against CNT rebundling. The strength of this repulsion between the coated tubes depends on many parameters such as the strength of the repulsive interaction between the head groups, the distance dependence of this interaction, the flexibility of the head groups, the temperature, etc. However, it is reasonable to assume that the shielding against rebundling is better the higher the density of the head groups is.

This is difficult to assess from snapshots such as the one shown in Figure 4e. However, together with Figure 4d it shows that, although surfactant molecules form adsorbed micelles and thus generate a very heterogeneous structure of adsorbed surfactant tails, surfactant head groups are much more evenly distributed. Therefore, it is sensible to introduce a radial density profile which is defined as the (canonical ensemble average of the) local density of head beads at distance R from the tube axis averaged over the length of the tube and rotation around the tube axis. These density profiles are shown in Figure 5.

In the lower concentration regime, i.e., for values below the CSAC, the density of head groups is low and increases only slightly with increasing concentration. As the concentration increases past the CSAC, the head density quickly increases. This is consistent with the steep increase of the adsorbed amount at the CSAC. As discussed above, adsorption is essentially complete at $C \approx 2 \times 10^{-5}$. Consequently, the head density remains almost constant if the concentration is increased beyond $C \approx 2 \times 10^{-5}$. As the density profiles do not show significant changes after the leveling-off of the adsorbed amount somewhat above the CSAC, we do not expect significantly improved shielding for surfactant concentrations well beyond the CSAC. In other words, our results indicate that a concentration just above the CSAC, and thus significantly lower than the cmc, should be sufficient to stabilize the dispersion. If this is insufficient for stabilization, any further concentration increase should not improve the stabilization significantly.

Experimental Results. In order to verify the predictions of the simulations we prepared a series of dispersions of SWCNTs

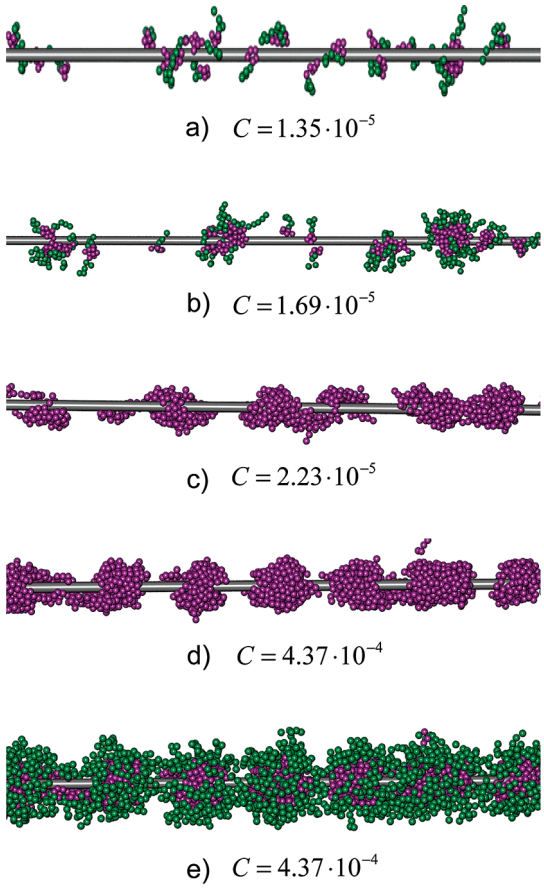

Figure 4. Simulation snapshots at different bulk concentrations as indicated in the figure. In parts a, b, and e the hydrophilic surfactant head beads are shown in green and the hydrophobic tail beads in purple, while in parts c and d only the hydrophobic tail beads are shown for clarity.

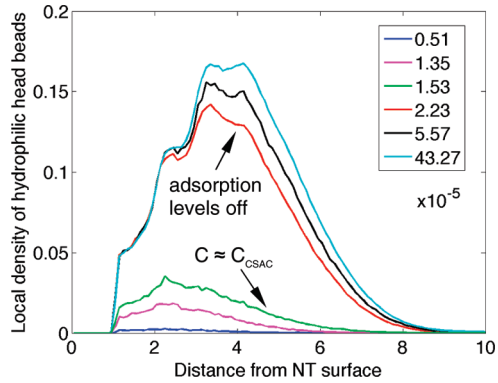

Figure 5. Radial density distributions of head groups as the local density of heads groups as a function of distance from the tube surface at various concentrations indicated in the figure. Head densities are low below the CSAC, increase quickly just after the CSAC, and remain essentially unchanged when the adsorbed amount levels off at $C \approx 2 \times 10^{-5}$.

in solutions of the anionic surfactants SDS and SDBS for a wide range of concentrations above and below the cmc.

After centrifugation of the original dispersions, the resultant supernatant fractions had different color densities. For the SDS series the color density clearly decreased with decreasing surfactant concentration, while for the SDBS series only sample SDBS02 ($C = 0.53C_{cmc}$) appeared less dense than dispersions obtained with surfactant concentrations above the cmc. The actual SWCNT concentrations in dispersions were determined

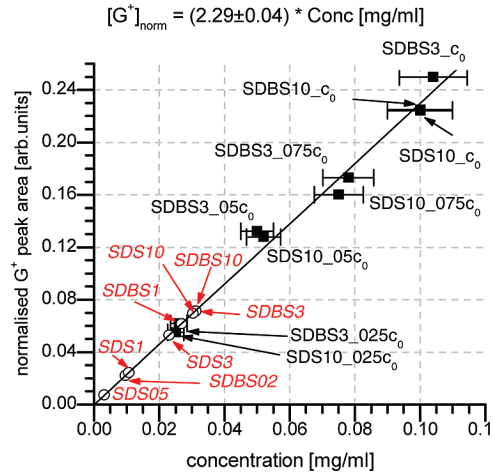

Figure 6. G^+-band area normalized to water peak (ν_{O-H}) versus concentration. Dispersions with known concentrations are marked with black squares and were used for creating the linear concentration calibration curve. The unknown concentrations for dispersions after centrifugation (small circles) were estimated on the basis of the normalized area of the G^+-band in the Raman spectra of corresponding dispersions and the created calibration line.

by means of Raman spectroscopy.[85] The original dispersions SDS10 and SDBS3 with concentration (c_0) of 0.1 mg SWCNT per mL were diluted with appropriate surfactant to a series of concentrations (c/c_0 of 0.75, 0.5, and 0.25) immediately after ultrasonic treatment. These dispersions with known concentrations were then used for creation of the plot of concentration vs G^+ -peak area normalized to the water peak (ν_{O-H}).[85] The resulting calibration curve was then used for determination of concentrations in dispersions after centrifugation (Figure 6). The concentration values for the centrifuged dispersions are shown in Table 2.

The diameter distributions of both individual SWCNT and nanotube bundles in the obtained dispersions for different surfactants after centrifugation were measured by AFM. In order to obtain sufficient statistics, about 200 species were measured for each dispersion sample. We assume that the process of "sticking" of the SWCNT from dispersion to the functionalized Si surface under normal gravity and after centrifugation is random and governed only by the Brownian motion of tubes in solution. Therefore, the diameter distribution of tubes/bundles obtained from AFM height measurements should directly represent the aggregation state of the SWCNT in dispersion. In our SWCNT samples the diameter (i.e., the AFM profile height) distributions for all concentrations of surfactants fitted well with log-normal distributions, however, with different widths and positions of maxima, as shown in Figures 7 and 8.

The AFM data (Figures 7 and 8) clearly exhibit a decrease in diameter values in dispersions with surfactant concentrations below the cmc as follows from a shift of distribution maxima and its narrowing toward lower numbers. Additionally, the root mean square of the diameter distribution ($D_{rms} = (\sqrt{\langle D^2 \rangle})$ of tubes in dispersion, previously used by Coleman et al.[41,42,59,86−88] for estimation of the fraction of individual tubes per volume, also shows a significant decrease for dispersions produced in surfactant solutions below the cmc (Table 2). The difference in experimental conditions during preparation of dispersions (centrifugation carried out at 3000g by Sun et al.[59] and 20 000g in our case) resulted in our dispersions showing D_{rms} values <2 (and even <1 for the solution SDS05), contrary to Sun's data[59] where D_{rms} stabilized at values of ~2.4 nm. Although still significant, the mass fraction (concentration) of SWCNT in

TABLE 2: Parameters of SWCNT Dispersions

dispersion	surfactant concn (mg/mL)	surfactant concn in cmc	SWCNT concentration (mg/mL) in supernatant	surfactant/SWCNT ratio (w/w)	D_{rms} ($\sqrt{\langle D^2 \rangle}$) (nm)	fraction of individual tubes (%)[b]	max value of dia obsd in supernatant (nm)
SDBS10	10	26.61	0.0325	307.7	1.818	35	4.3
SDBS3	3	7.98	0.032	93.8	2.051	22	4.4
SDBS1	1	2.66	0.0265	37.7	1.714	47	4.5
SDBS02	0.2	0.53	0.0095	21.1	1.250	67	2.7
SDS10	10	4.34	0.0305	327.9	1.503	52	3.3
SDS3	3	1.3	0.0225	133.3	2.105	32	4.9
SDS1	1	0.43	0.0105	95.2	1.342	63	2.8
SDS05	0.5	0.22	0.0032	156.3[a]	0.815	98	1.5

[a] This is an overevaluated number since it does not take into account the consumption of surfactant on air−liquid and liquid−solid (walls of the container) interfaces. [b] Assuming that species with diameter <1.3 nm are individual tubes.

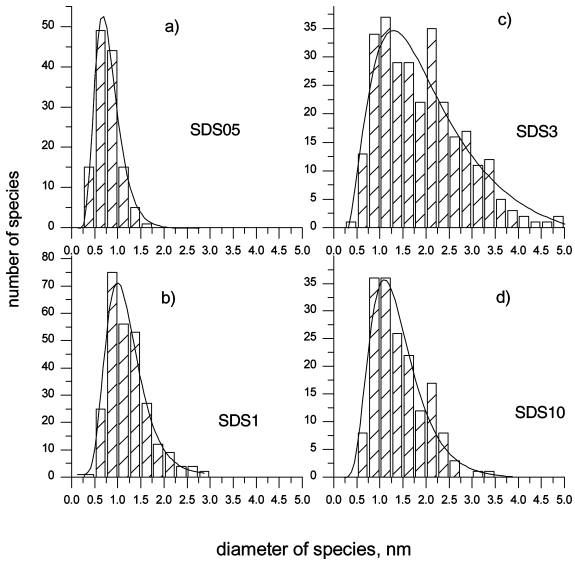

Figure 7. Diameter distribution of SWCNT species in centrifuged SDS dispersions prepared at different surfactant concentrations: (a) 0.5 mg SDS/mL of solution, (b) 1 mg SDS/mL, (c) 3 mg SDS/mL, and (d) 10 mg SDS/mL.

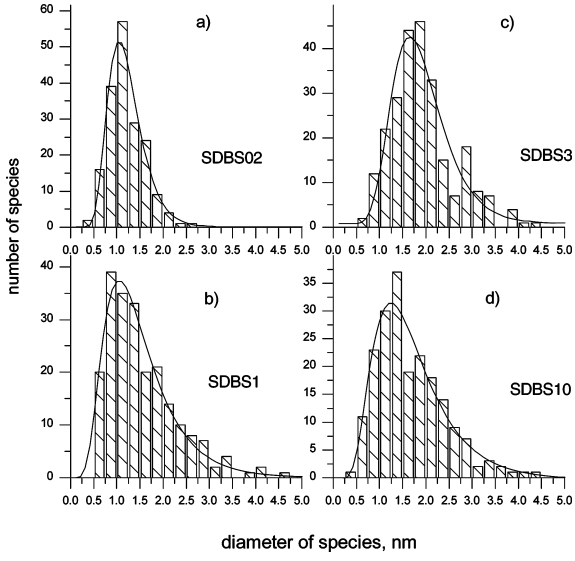

Figure 8. Diameter distribution of SWCNT species in centrifuged SDBS dispersions prepared at different surfactant concentrations: (a) 0.2 mg SDBS/mL of solution, (b) 1 mg SDBS/mL, (c) 3 mg SDBS/mL, and (d) 10 mg SDBS/mL.

surfactant solutions below cmc is lower than in solutions above cmc, in general correspondence with literature data.[59] It is interesting to note that the w/w ratio of surfactant-to-SWCNT shows the tendency to decrease along with the decrease of the surfactant concentration (Table 2).

The HiPco individual SWCNT have diameters in the range 0.7−1.4 nm.[82,89] Simple geometry considerations show that an AFM height profile of 1.3 nm may be the result of a bundle consisting of three tubes with diameter of 0.7 nm. Bundles composed of thicker tubes and/or greater number of tubes should have larger diameters. Therefore in further analysis of dispersions we assume that the species with heights <1.3 nm are individual carbon nanotubes. (This could also include agglomerates of two carbon nanotubes lying flat on the substrate surface.) Thus, from AFM-based height distributions it follows that for dispersions SDBS02 and SDS1 (0.53 cmc and 0.43 cmc, respectively) the content of individual tubes in dispersion is around 65% at a fairly high concentration of tubes of approximately 0.01 mg/mL. The dispersion SDS05 (∼0.2 cmc) consists almost completely of individual tubes (98%) with a CNT concentration of 3×10^{-3} mg/mL. The SWCNT dispersions prepared from surfactant solutions above cmc exhibit an individual tube content of only 22−52% (Table 2).

Additional information on the bundle size distribution in SWCNT dispersions below cmc may be extracted from the maximum diameter value of deposited species. It is obvious from diameter distributions in our samples (Figures 7 and 8) that centrifugation of dispersions at 20 000*g* completely removes the species with diameters >5 nm. If it is assumed that the sedimentation velocity of SWCNT aggregates in surfactant solution depends on the number of tubes in the bundle (i.e., bundle size),[90] then all examined dispersions should contain species with diameters of no more than 5 nm. Indeed, a significant amount of species with diameters $3.5 < d_t < 5$ nm is observed for all dispersions with surfactant concentration above cmc, except for SDS10 with a maximum diameter value of 3.3 nm (Table 2). It is, however, interesting that for SWCNT dispersions, prepared in below-cmc surfactant solutions, the maximum diameter values are 2.8 nm for SDS1, 2.25 nm for SDBS02 and 1.5 nm for SDS05 dispersions. Thus, only small aggregates are stabilized in dispersions with surfactant solutions below the cmc. There are two possible explanations for this: (i) surfactant adsorption is insufficient to prevent the reagglomeration of small to larger bundles or (ii) it is insufficient to stabilize the small bundles in the suspension against the centrifugal force. In any case, our results suggest that adsorption on individual tubes and bundles might follow different surfactant concentration dependencies and possibly different mechanisms.

Summary and Conclusions

In this paper, we present the results of an experimental/theoretical study of the physical processes relevant to the

dispersion of CNTs. In particular we have investigated the dispersive capabilities of surfactant solutions below the cmc.

The experiments were carried out on HiPco SWCNTs with two surfactants SDS and SDBS, with different cmc values $C_{cmc}(SDS) \approx 6C_{cmc}(SDBS)$. The results obtained for both surfactants are remarkably similar if the concentration scale is normalized by the respective cmc. In both systems we find as follows:

1. CNT may be dispersed in surfactant solutions below the cmc.

2. A relatively small but significant fraction of tubes is suspended in below-cmc dispersions.

3. SWCNT in surfactant solutions below cmc show a tendency to be dispersed as individual tubes and small bundles.

4. Diameter distribution of SWCNT species in above-cmc surfactant dispersions is significantly broader and is shifted to larger diameters, compared to in below-cmc dispersions.

Using computer simulations of a coarse-grained model, we studied the concentration dependence of surfactant adsorption on a small individual SWCNT. The simulation results show as follows:

1. Adsorption is essentially complete at approximately 0.5 cmc.

2. Above the cmc only minimal changes in the adsorbed amount and the radial head density profile are observed.

3. Adsorption is dominated by surfactant self-assembly.

To develop an understanding of the experimentally obtained diameter distributions it is important to realize that the experimental results are influenced by three processes: (i) ultrasonication, (ii) relaxation to equilibrium and (iii) centrifugation. The latter, centrifugation, is also the last processing step before the samples are measured and might, therefore, dominate the results.

Centrifugation separates objects with higher density (larger agglomerates of SWCNT) out of solution. In the present case these objects are CNT/surfactant composites. Although it is difficult to determine the boundaries of these CNT/surfactant composites as they are soft and have attractive interactions with water, it is clear that a higher number of adsorbed surfactant molecules reduces the over all density of the complex and makes them more hydrophilic. Both effects support the dispersibility of the CNT/surfactant composite.

The simulation results show that surfactant adsorption on small tubes is essentially complete well below the cmc. This means that increasing the concentration beyond the cmc should not further improve the dispersibility of individual CNTs. This is consistent with our experimental observation of dispersed individual tubes below the cmc.

There remain a number of key questions that need further clarification:

1. Why are small bundles dispersed only at higher concentration? This indicates a different adsorption mechanism compared to individual tubes which might be caused by the different surface morphologies and interaction energies of bundles compared to individual tubes.

2. Why does the number of dispersed individual tubes increase with concentration? This can only happen if the number of exfoliated tubes depends on the concentration.

3. What is the actual surfactant concentration in the sample? Surfactant adsorption on all available surfaces, including CNTs as well as the containers, decreases the number of molecules in solution and thus the concentration. However, for detailed interpretation and comparability of the experimental results knowledge of the actual concentration is essential.

Further experimental and simulation studies are in progress to provide answers.

Acknowledgment. Financial support for an EPSRC DTA award and from EastChem is gratefully acknowledged. A.L. acknowledges financial support from the Nuffield Foundation.

References and Notes

(1) Coleman, J. N.; Khan, U.; Gun'ko, Y. K. *Adv. Mater.* **2006**, *18*, 689.
(2) Thostenson, E. T.; Chou, T.-W. *J. Phys. D: Appl. Phys.* **2002**, L77.
(3) Reibold, M.; Paufler, P.; Levin, A. A.; Kochmann, W.; Patzke, N.; Meyer, D. C. *Nature* **2006**, *444*, 286.
(4) Regev, O.; ElKati, P. N. B.; Loos, J.; Koning, C. E. *Adv. Mater.* **2004**, *16*, 248.
(5) Suryasarathi, B.; Arup, R. B.; Rupesh, A. K.; Ajit, R. K.; Patro, T. U.; Sivaraman, P. *Nanotechnology* **2008**, 335704.
(6) Star, A.; Stoddart, J. F.; Steuerman, D.; Diehl, M.; Boukai, A.; Wong, E. W.; Yang, X.; Chung, S.-W.; Choi, H.; Heath, J. R. *Angew. Chem., Int. Ed.* **2001**, *40*, 1721.
(7) Yamamoto, T.; Watanabe, K.; Hernández, E. Mechanical Properties, Thermal Stability and Heat Transport in Carbon Nanotubes. In *Topics in Applied Physics: Carbon Nanotubes*; Springer: Berlin, 2008; p 165.
(8) Hsu, I. K.; Pettes, M. T.; Bushmaker, A.; Aykol, M.; Shi, L.; Cronin, S. B. *Nano Lett.* **2009**, *9*, 590.
(9) Yu, A.; Ramesh, P.; Sun, X.; Bekyarova, E.; Itkis, M. E.; Haddon, R. C. *Adv. Mater.* **2008**, *20*, 4740.
(10) Wang, S.; Liang, R.; Wang, B.; Zhang, C. *Carbon* **2009**, *47*, 53.
(11) Duong, H. M.; Papavassiliou, D. V.; Mullen, K. J.; Wardle, B. L.; Maruyama, S. *J. Phys. Chem. C* **2008**, *112*, 19860.
(12) Cai, D.; Song, M. *Carbon* **2008**, *46*, 2107.
(13) Arnold, M. S.; Green, A. A.; Hulvat, J. F.; Stupp, S. I.; Hersam, M. C. *Nat. Nanotechnol.* **2006**, *1*, 60.
(14) Tu, X.; Zheng, M. *Nano Res.* **2008**, *1*, 185.
(15) Lopez-Pastor, M.; Dominguez-Vidal, A.; Ayora-Canada, M. J.; Simonet, B. M.; Lendl, B.; Valcarcel, M. *Anal. Chem.* **2008**, *80*, 2672.
(16) Arnold, M. S.; Stupp, S. I.; Hersam, M. C. *Nano Lett.* **2005**, *5*, 713.
(17) Green, A. A.; Hersam, M. C. *Nano Lett.* **2008**, *8*, 1417.
(18) Zheng, M.; Jagota, A.; Strano, M. S.; Santos, A. P.; Barone, P.; Chou, S. G.; Diner, B. A.; Dresselhaus, M. S.; McLean, R. S.; Onoa, G. B.; Samsonidze, G. G.; Semke, E. D.; Usrey, M.; Walls, D. J. *Science* **2003**, *302*, 1545.
(19) Strano, M. S.; Moore, V. C.; Miller, M. K.; Allen, M. J.; Haroz, E. H.; Kittrell, C.; Hauge, R. H.; Smalley, R. E. *J. Nanosci. Nanotechnol.* **2003**, *3*, 81.
(20) Vaisman, L.; Wagner, H. D.; Marom, G. *Adv. Colloid Interface Sci.* **2006**, *128*−*130*, 37.
(21) Gong, X.; Liu, J.; Baskaran, S.; Voise, R. D.; Young, J. S. *Chem. Mater.* **2000**, *12*, 1049.
(22) Islam, M. F.; Rojas, E.; Bergey, D. M.; Johnson, A. T.; Yodh, A. G. *Nano Lett.* **2003**, *3*, 269.
(23) Wenseleers, W.; Vlasov, I. I.; Goovaerts, E.; Obraztsova, E. D.; Lobach, A. S.; Bouwen, A. *Adv. Funct. Mater.* **2004**, *14*, 1105.
(24) Fugetsu, B.; Han, W.; Endo, N.; Kamiya, Y.; Okuhara, T. *Chem. Lett.* **2005**, *34*, 1218.
(25) O'Connell, M. J.; Boul, P.; Ericson, L. M.; Huffman, C.; Wang, Y.; Haroz, E.; Kuper, C.; Tour, J.; Ausman, K. D.; Smalley, R. E. *Chem. Phys. Lett.* **2001**, *342*, 265.
(26) Manivannan, S.; Jeong, I.; Ryu, J.; Lee, C.; Kim, K.; Jang, J.; Park, K. *J. Mater. Sci.: Mater. Electron.* **2009**, *20*, 223.
(27) Tetsuya Uchida, S. K. *J. Appl. Polym. Sci.* **2005**, *98*, 985.
(28) Rasheed, A.; Dadmun, M. D.; Ivanov, I.; Britt, P. F.; Geohegan, D. B. *Chem. Mater.* **2006**, *18*, 3513.
(29) Rice, N. A.; Soper, K.; Zhou, N.; Merschrod, E.; Zhao, Y. *Chem. Commun.* **2006**, 4937.
(30) Chen, H.; Xue, Q.; Zheng, Q.; Xie, J.; Yan, K. *J. Phys. Chem. C* **2008**, *112*, 16514.
(31) Ortiz-Acevedo, A.; Xie, H.; Zorbas, V.; Sampson, W. M.; Dalton, A. B.; Baughman, R. H.; Draper, R. K.; Musselman, I. H.; Dieckmann, G. R. *J. Am. Chem. Soc.* **2005**, *127*, 9512.
(32) Zheng, M.; Jagota, A.; Semke, E. D.; Diner, B. A.; McLean, R. S.; Lustig, S. R.; Richardson, R. E.; Tassi, N. G. *Nat. Mater.* **2003**, *2*, 338.
(33) Salzmann, C. G.; Lee, G. K. C.; Ward, M. A. H.; Chu, B. T. T.; Green, M. L. H. *J. Mater. Chem.* **2008**, *18*, 1977.
(34) Takahashi, T.; Tsunoda, K.; Yajima, H.; Ishii, T. *Jpn. J. Appl. Phys., Part 1: Regular Pap., Short Notes Rev. Pap.* **2004**, *43*, 3636.
(35) Minami, N.; Kim, Y.; Miyashita, K.; Kazaoui, S.; Nalini, B. *Appl. Phys. Lett.* **2006**, *88*, 093123/1.
(36) Yan, L. Y.; Poon, Y. F.; Chan-Park, M. B.; Chen, Y.; Zhang, Q. *J. Phys. Chem. C* **2008**, *112*, 7579.

(37) Star, A.; Steuerman, D. W.; Heath, J. R.; Stoddart, J. F. *Angew. Chem., Int. Ed.* **2002**, *41*, 2508.
(38) Fukushima, T.; Kosaka, A.; Ishimura, Y.; Yamamoto, T.; Takigawa, T.; Ishii, N.; Aida, T. *Science* **2003**, *300*, 2072.
(39) Wang, J.; Li, Y. *J. Am. Chem. Soc.* **2009**, *131*, 5364.
(40) Wang, J.; Chu, H.; Li, Y. *ACS Nano* **2008**, *2*, 2540.
(41) Giordani, S.; Bergin, S. D.; Nicolosi, V.; Lebedkin, S.; Kappes, M. M.; Blau, W. J.; Coleman, J. N. *J. Phys. Chem. B* **2006**, *110*, 15708.
(42) Bergin, S. D.; Nicolosi, V.; Giordani, S.; de Gromard, A.; Carpenter, L.; Blau, W. J.; Coleman, J. N. *Nanotechnology* **2007**, *18*, 455705.
(43) Banerjee, S.; Hemraj-Benny, T.; Wong, S. S. *Adv. Mater.* **2005**, *17*, 17.
(44) Hilding, J.; Grulke, E. A.; Zhang, Z. G.; Lockwood, F. *J. Dispersion Sci. Technol.* **2003**, *24*, 1.
(45) Penicaud, A.; Poulin, P.; Derre, A.; Anglaret, E.; Petit, P. *J. Am. Chem. Soc.* **2005**, *127*, 8.
(46) Price, B. K.; Tour, J. M. *J. Am. Chem. Soc.* **2006**, *128*, 12899.
(47) Wang, Y.; Iqbal, Z.; Mitra, S. *J. Am. Chem. Soc.* **2006**, *128*, 95.
(48) Bauer, B. J.; Becker, M. L.; Bajpai, V.; Fagan, J. A.; Hobbie, E. K.; Migler, K.; Guttman, C. M.; Blair, W. R. *J. Phys. Chem. C* **2007**, *111*, 17914.
(49) Hung, N.; Anoshkin, I.; Dementjev, A.; Katorov, D.; Rakov, E. *Inorg. Mater.* **2008**, *44*, 219.
(50) Kharisov, B. I.; Kharissova, O. V.; Gutierrez, H. L.; Mendez, U. O. *Ind. Eng. Chem. Res.* **2009**, *48*, 572.
(51) Zhao, J.; Park, H.; Han, J.; Lu, J. P. *J. Phys. Chem. B* **2004**, *108*, 4227.
(52) Umeyama, T.; Tezuka, N.; Fujita, M.; Matano, Y.; Takeda, N.; Murakoshi, K.; Yoshida, K.; Isoda, S.; Imahori, H. *J. Phys. Chem. C* **2007**, *111*, 9734.
(53) Fagan, S. B.; da Silva, A. J. R.; Mota, R.; Baierle, R. J.; Fazzio, A. *Phys. Rev. B* **2003**, *67*, 033405.
(54) Lu, J.; Wang, D.; Nagase, S.; Ni, M.; Zhang, X.; Maeda, Y.; Wakahara, T.; Nakahodo, T.; Tsuchiya, T.; Akasaka, T.; Gao, Z.; Yu, D.; Ye, H.; Zhou, Y.; Mei, W. N. *J. Phys. Chem. B* **2006**, *110*, 5655.
(55) Cho, E.; Kim, H.; Kim, C.; Han, S. *Chem. Phys. Lett.* **2006**, *419*, 134.
(56) Kang, H. S. *J. Chem. Phys.* **2004**, *121*, 6967.
(57) Kim, K. S.; Bae, D. J.; Kim, J. R.; Park, K. A.; Lim, S. C.; Kim, J. J.; Choi, W. B.; Park, C. Y.; Lee, Y. H. *Adv. Mater.* **2002**, *14*, 1818.
(58) Bonard, J.-M.; Stora, T.; Salvetat, J.-P.; Maier, F.; Stöckli, T.; Duschl, C.; Forró, L.; de Heer, W. A.; Châtelain, A. *Adv. Mater.* **1997**, *9*, 827.
(59) Sun, Z.; Nicolosi, V.; Rickard, D.; Bergin, S. D.; Aherne, D.; Coleman, J. N. *J. Phys. Chem. C* **2008**, *112*, 10692.
(60) Utsumi, S.; Kanamaru, M.; Honda, H.; Kanoh, H.; Tanaka, H.; Ohkubo, T.; Sakai, H.; Abe, M.; Kaneko, K. *J. Colloid Interface Sci.* **2007**, *308*, 276.
(61) Moore, V. C.; Strano, M. S.; Haroz, E. H.; Hauge, R. H.; Smalley, R. E.; Schmidt, J.; Talmon, Y. *Nano Lett.* **2003**, *3*, 1379.
(62) Matarredona, O.; Rhoads, H.; Li, Z.; Harwell, J. H.; Balzano, L.; Resasco, D. E. *J. Phys. Chem. B* **2003**, *107*, 13357.
(63) McDonald, T. J.; Engtrakul, C.; Jones, M.; Rumbles, G.; Heben, M. J. *J. Phys. Chem. B* **2006**, *110*, 25339.
(64) Nativ-Roth, E.; Shvartzman-Cohen, R.; Bounioux, C.; Florent, M.; Zhang, D.; Szleifer, I.; Yerushalmi-Rozen, R. *Macromolecules* **2007**, *40*, 3676.
(65) Wallace, E. J.; Mark, S. P. S. *Nanotechnology* **2009**; 045101.
(66) Wallace, E. J.; Sansom, M. S. P. *Nano Lett.* **2007**, *7*, 1923.
(67) Tummala, N. R.; Striolo, A. *ACS Nano* **2009**, *3*, 595.
(68) Patel, N.; Egorov, S. A. *J. Am. Chem. Soc.* **2005**, *127*, 14124.
(69) Nikolaev, P.; Bronikowski, M. J.; Bradley, R. K.; Rohmund, F.; Colbert, D. T.; Smith, K. A.; Smalley, R. E. *Chem. Phys. Lett.* **1999**, *313*, 91.
(70) Mukerjee, P.; Kapauan, P.; Meyer, H. G. *J. Phys. Chem.* **1966**, *70*, 783.
(71) Thévenot, C.; Grassl, B.; Bastiat, G.; Binana, W. *Colloids Surf. A: Physicochem. Eng. Aspects* **2005**, *252*, 105.
(72) Liu, J.; Casavant, M. J.; Cox, M.; Walters, D. A.; Boul, P.; Lu, W.; Rimberg, A. J.; Smith, K. A.; Colbert, D. T.; Smalley, R. E. *Chem. Phys. Lett.* **1999**, *303*, 125.
(73) Lewenstein, J. C.; Burgin, T. P.; Ribayrol, A.; Nagahara, L. A.; Tsui, R. K. *Nano Lett.* **2002**, *2*, 443.
(74) Burgin, T. P.; Lewenstein, J. C.; Werho, D. *Langmuir* **2005**, *21*, 6596.
(75) Angelikopoulos, P.; Bock, H. *J. Phys. Chem. B* **2008**, *112*, 13793.
(76) Weisstein, E. W. Point-Line Distance—3-Dimensional. In MathWorld—A Wolfram Web Resource.
(77) Robert, D. G.; Patrick, B. W. *J. Chem. Phys.* **1997**, *107*, 4423.
(78) Rekvig, L.; Kranenburg, M.; Vreede, J.; Hafskjold, B.; Smit, B. *Langmuir* **2003**, *19*, 8195.
(79) Bock, H.; Gubbins, K. E. *Phys. Rev. Lett.* **2004**, *92*, 135701.
(80) Dietsch, O.; Eltekov, A.; Bock, H.; Gubbins, K. E.; Findenegg, G. H. *J. Phys. Chem. C* **2007**, *111*, 16045.
(81) Richard, C.; Balavoine, F.; Schultz, P.; Ebbesen, T. W.; Mioskowski, C. *Science* **2003**, *300*, 775.
(82) Brar, V. W.; Samsonidze, G. G.; Santos, A. P.; Chou, S. G.; Chattopadhyay, D.; Kim, S. N.; Papadimitrakopoulos, F.; Zheng, M.; Jagota, A.; Onoa, G. B.; Swan, A. K.; Unlu, M. S.; Goldberg, B. B.; Dresselhaus, G.; Dresselhaus, M. S. *J. Nanosci. Nanotechnol.* **2005**, *5*, 209.
(83) Hassan, P. A.; Fritz, G.; Kaler, E. W. *J. Colloid Interface Sci.* **2003**, *257*, 154.
(84) Segota, S.; Heimer, S.; Tezak, Đ. *Colloids Surf. A: Physicochem. Eng. Aspects* **2006**, *274*, 91.
(85) Salzmann, C. G.; Chu, B. T. T.; Tobias, G.; Llewellyn, S. A.; Green, M. L. H. *Carbon* **2007**, *45*, 907.
(86) Cathcart, H.; Quinn, S.; Nicolosi, V.; Kelly, J. M.; Blau, W. J.; Coleman, J. N. *J. Phys. Chem. C* **2007**, *111*, 66.
(87) Bergin, S. D.; Nicolosi, V.; Cathcart, H.; Lotya, M.; Rickard, D.; Sun, Z.; Blau, W. J.; Coleman, J. N. *J. Phys. Chem. C* **2008**, *112*, 972.
(88) Bergin, S. D.; Nicolosi, V.; Streich, P. V.; Giordani, S.; Sun, Z.; Windle, A. H.; Ryan, P.; Niraj, N. P. P.; Wang, Z.-T. T.; Carpenter, L.; Blau, W. J.; Boland, J. J.; Hamilton, J. P.; Coleman, J. N. *Adv. Mater.* **2008**, *20*, 1876.
(89) Izard, N.; Riehl, D.; Anglaret, E. *Los Alamos National Laboratory, Preprint Archive, Condensed Matter*; 2005, Vol. 1; http://arxiv1.library.cornell.edu/abs/cond-mat/0501426.
(90) Nadler, M.; Mahrholz, T.; Riedel, U.; Schilde, C.; Kwade, A. *Carbon* **2008**, *46*, 1384.

JP905925R

References

[1] S. Iijima, "Helical microtubules of graphitic carbon," *Nature*, vol. 354, pp. 56–58, November 1991.

[2] A. Thess, R. Lee, P. Nikolaev, H. Dai, P. Petit, J. Robert, C. Xu, Y. H. Lee, S. G. Kim, A. G. Rinzler, D. T. Colbert, G. E. Scuseria, D. Tomanek, J. E. Fischer, and R. E. Smalley, "Crystalline Ropes of Metallic Carbon Nanotubes," *Science*, vol. 273, no. 5274, pp. 483–487, 1996.

[3] P. M. Ajayan, "Nanotubes from carbon," *Chemical Reviews*, vol. 99, no. 7, pp. 1787–1800, 1999. PMID: 11849010.

[4] B. G. Demczyk, Y. M. Wang, J. Cumings, M. Hetman, W. Han, A. Zettl, and R. O. Ritchie, "Direct mechanical measurement of the tensile strength and elastic modulus of multiwalled carbon nanotubes," *Materials Science and Engineering A*, vol. 334, no. 1-2, pp. 173 – 178, 2002.

[5] L. Zanello, "Electrical properties of osteoblasts cultured on carbon nanotubes," *Nano Lett.*, vol. 1, pp. 19–22, July 2006.

[6] W. Yang, P. Thordarson, J. J. Gooding, S. P. Ringer, and F. Braet, "Carbon nanotubes for biological and biomedical applications," *Nanotechnology*, vol. 18, no. 41, pp. 412001–412013, 2007.

[7] W. Zhao, C. Song, and P. E. Pehrsson, "Water-soluble and optically ph-sensitive single-walled carbon nanotubes from surface modification," *J. Am. Chem. Soc*, vol. 124, no. 42, pp. 12418–12419, 2002.

[8] Z. Liu, S. Tabakman, K. Welsher, and H. Dai, "Carbon nanotubes in biology and medicine: In vitro in vivo detection, imaging and drug delivery," *Nano Research*, vol. 2, pp. 85–120, February 2009.

[9] J.-F. Drillet, H. Bueb, R. Dittmeyer, U. Dettlaff-Weglikowska, and S. Roth, "Efficient swcnt-based anode for dmfc applications," *J. Electrochemical Soc.*, vol. 156, no. 10, pp. F137–F144, 2009.

[10] E. Cubukcu, F. Degirmenci, C. Kocabas, M. A. Zimmler, J. A. Rogers, and F. Capasso, "Aligned carbon nanotubes as polarization-sensitive, molecular near-field detectors," *Proc. Nat. Ac. Sci.*, vol. 106, no. 8, pp. 2495–2499, 2009.

[11] I. Capek, "Dispersions, novel nanomaterial sensors and nanoconjugates based on carbon nanotubes," *Adv. Colloid Interfac.*, vol. 150, no. 2, pp. 63 – 89, 2009.

[12] W. Cheung, P. L. Chiu, R. R. Parajuli, Y. Ma, S. R. Ali, and H. He, "Fabrication of high performance conducting polymer nanocomposites for biosensors and flexible electronics: summary of the multiple roles of dna dispersed and functionalized single walled carbon nanotubes," *J. Mat. Chem.*, vol. 19, no. 36, pp. 6465–6480, 2009.

[13] J. Cveticanin, G. Joksic, A. Leskovac, S. Petrovic, A. V. Sobot, and O. Neskovic, "Using carbon nanotubes to induce micronuclei and double strand breaks of the dna in human cells," *Nanotechnology*, vol. 21, no. 1, p. 015102 (7pp), 2010.

[14] M. Mahmood, A. Karmakar, A. Fejleh, T. Mocan, C. Iancu, L. Mocan, D. T. Iancu, Y. Xu, E. Dervishi, Z. Li, A. R. Biris, R. Agarwal, N. Ali, E. I. Galanzha, A. S. Biris, and V. P. Zharov, "Synergistic enhancement of cancer therapy using a combination of carbon nanotubes and anti-tumor drug," *Nanomedicine*, vol. 4, no. 8, pp. 883–893, 2009. PMID: 19958225.

[15] T. Simmons, S.-H. Lee, T.-J. Park, D. Hashim, P. Ajayan, and R. Linhardt, "Antiseptic single wall carbon nanotube bandages," *Carbon*, vol. 47, no. 6, pp. 1561 – 1564, 2009.

[16] M. Tarasov, J. Svensson, L. Kuzmin, and E. E. B. Campbell, "Carbon nanotube bolometers," *Appl.Phys. Lett.*, vol. 90, no. 16, p. 163503, 2007.

[17] J. Suhr, W. Zhang, P. M. Ajayan, and N. A. Koratkar, "Temperature-activated interfacial friction damping in carbon nanotube polymer composites," *Nano Lett.*, vol. 6, no. 2, pp. 219–223, 2006.

[18] W. Dacheng and L. Yunqi, "The intramolecular junctions of carbon nanotubes," *Adv. Mat.*, vol. 20, no. 15, pp. 2815–2841, 2008.

[19] J. Coleman, U. Khan, and Y. Gunko, "Mechanical reinforcement of polymers using carbon nanotubes," *Adv. Mat.*, vol. 18, no. 6, pp. 689–706, 2006.

[20] P. Angelikopoulos and H. Bock, "Directed self-assembly of surfactants in carbon nanotube materials," *J. Phys. Chem. B*, vol. 112, no. 44, pp. 13793–13801, 2008.

[21] N. Grossiord, H. E. Miltner, J. Loos, J. Meuldijk, B. Van Mele, and C. E. Koning, "On the crucial role of wetting in the preparation of conductive polystyrene;carbon nanotube composites," *Chem. Mat.*, vol. 19, no. 15, pp. 3787–3792, 2007.

[22] K. Koziol, J. Vilatela, A. Moisala, M. Motta, P. Cunniff, and M. Sennett, "High-performance carbon nanotube fiber," *Science*, vol. 318, no. 5858, pp. 775–778, 2007.

[23] B. Vigolo, A. Pnicaud, C. Coulon, C. Sauder, R. Pailler, C. Journet, P. Bernier, and P. Poulin, "Macroscopic fibers and ribbons of oriented carbon nanotubes.," *Science*, vol. 290, no. 5495, pp. 1331–1334, 2000.

[24] M. Motta, Y.-L. Li, I. Kinloch, and A. Windle, "Mechanical properties of continuously spun fibers of carbon nanotubes," *Nano Lett.*, vol. 5, no. 8, pp. 1529–1533, 2005.

[25] S. W. Lee, B. Kim, D. S. Lee, H. J. Lee, J. G. Park, S. J. Ahn, E. E. B. Campbell, and Y. W. Park, "Fabrication and mechanical properties of suspended one-dimensional polymer nanostructures: polypyrrole nanotube and helical polyacetylene nanofibre," *Nanotech.*, vol. 17, no. 4, pp. 992–996, 2006.

[26] L. Berhan, Y. B. Yi, A. M. Sastry, E. Munoz, M. Selvidge, and R. Baughman, "Mechanical properties of nanotube sheets: Alterations in joint morphology and achievable moduli in manufacturable materials," *J. Appl. Phys.*, vol. 95, no. 8, pp. 4335–4345, 2004.

[27] J. N. Coleman, W. J. Blau, A. B. Dalton, E. M. noz, S. Collins, B. G. Kim, J. Razal, M. Selvidge, G. Vieiro, and R. H. Baughman, "Improving the mechanical properties of single-walled carbon nanotube sheets by intercalation of polymeric adhesives," *Appl. Phys. Lett.*, vol. 82, no. 11, pp. 1682–1684, 2003.

[28] L. S. Schadler, S. C. Giannaris, and P. M. Ajayan, "Load transfer in carbon nanotube epoxy composites," *Appl. Phys. Lett.*, vol. 73, no. 26, pp. 3842–3844, 1998.

[29] A. Wall, J. N. Coleman, and M. S. Ferreira, "Physical mechanism for the mechanical reinforcement in nanotube-polymer composite materials," *Phys. Rev. B*, vol. 71, no. 12, 2005.

[30] A. T. C. Johnson, C. Staii, M. Chen, S. Khamis, R. Johnson, M. L. Klein, and A. Gelperin, "Dna-decorated carbon nanotubes for chemical sensing," *Semicond. Sci. Tech.*, vol. 21, no. 11, pp. S17–S21, 2006.

[31] R. J. Chen, S. Bangsaruntip, K. A. Drouvalakis, N. Wong Shi Kam, M. Shim, Y. Li, W. Kim, P. J. Utz, and H. Dai, "Noncovalent functionalization of carbon nanotubes for highly specific electronic biosensors," *Proc. Natl. Acad. Sci. Unit. States. Am.*, vol. 100, no. 9, pp. 4984–4989, 2003.

[32] R. H. Baughman, A. A. Zakhidov, and W. A. de Heer, "Carbon nanotubes–the route toward applications," *Science*, vol. 297, pp. 787–792, August 2002.

[33] M. J. O'Connell, P. Boul, L. M. Ericson, C. Huffman, Y. Wang, E. Haroz, C. Kuper, J. Tour, K. D. Ausman, and R. E. Smalley, "Reversible water-solubilization of single-walled carbon nanotubes by polymer wrapping," *Chem. Phys. Lett.*, vol. 342, no. 3-4, pp. 265 – 271, 2001.

[34] E. Schroder and P. Hyldgaard, "Van der waals interactions of parallel and concentric nanotubes," *Mater. Sci. Eng., C*, vol. 23, no. 6-8, pp. 721 – 725, 2003.

[35] J. Kleis, P. Hyldgaard, and E. Schrder, "Van der waals interaction of parallel polymers and nanotubes," *Comput. Mater. Sci.*, vol. 33, no. 1-3, pp. 192 – 199, 2005.

[36] L. A. Girifalco, M. Hodak, and R. S. Lee, "Carbon nanotubes, buckyballs, ropes, and a universal graphitic potential," *Phys. Rev. B*, vol. 62, pp. 13104–13110, Nov 2000.

[37] E. A. Muller, L. F. Rull, L. F. Vega, and K. E. Gubbins, "Adsorption of water on activated carbons; a molecular simulation study," *J. Phys. Chem.*, vol. 100, no. 4, pp. 1189–1196, 1996.

[38] J. H. Walther, R. L. Jaffe, E. M. Kotsalis, T. Werder, T. Halicioglu, and P. Koumoutsakos, "Hydrophobic hydration of c60 and carbon nanotubes in water," *Carbon*, vol. 42, no. 5-6, pp. 1185 – 1194, 2004. European Materials Research Society 2003, Symposium B: Advanced Multifunctional Nanocarbon Materials and Nanosystems.

[39] J. Chen, H. Liu, W. A. Weimer, M. D. Halls, D. H. Waldeck, and G. C. Walker, "Noncovalent engineering of carbon nanotube surfaces by rigid, functional conjugated polymers," *J. Am. Chem. Soc.*, vol. 124, no. 31, pp. 9034–9035, 2002.

[40] M. Monthioux, B. W. Smith, B. Burteaux, A. Claye, J. E. Fischer, and D. E. Luzzi, "Sensitivity of single-wall carbon nanotubes to chemical processing: an electron microscopy investigation," *Carbon*, vol. 39, no. 8, pp. 1251 – 1272, 2001.

[41] V. C. Moore, M. S. Strano, E. H. Haroz, R. H. Hauge, R. E. Smalley, J. Schmidt, and Y. Talmon, "Individually suspended single-walled carbon nanotubes in various surfactants," *Nano Lett.*, vol. 3, no. 10, pp. 1379–1382, 2003.

[42] H. Wang, W. Zhou, D. L. Ho, K. I. Winey, J. E. Fischer, C. J. Glinka, and E. K. Hobbie, "Dispersing single-walled carbon nanotubes with surfactants; a small angle neutron scattering study," *Nano Lett.*, vol. 4, no. 9, pp. 1789–1793, 2004.

[43] S. Cosnier, R. E. Ionescu, and M. Holzinger, "Aqueous dispersions of swcnts using pyrrolic surfactants for the electro-generation of homogeneous nanotube composites. application to the design of an amperometric biosensor," *J. Mat. Chem.*, vol. 18, no. 42, pp. 5129–5133, 2008.

[44] K. Yurekli, C. A. Mitchell, and R. Krishnamoorti, "Small-angle neutron scattering from surfactant-assisted aqueous dispersions of carbon nanotubes," *J. Am. Chem. Soc.*, vol. 126, no. 32, pp. 9902–9903, 2004.

[45] M. S. Strano, M. Valerie, M. Michael, A. Mathew, H. Erik, C. Kittrell, H. Robert, and S. R.E., "Reversible water-solubilization of single-walled carbon nanotubes by polymer wrapping," *J. Nanosci. Nanotechnol.*, no. 1-2, pp. 81 – 86, 2003.

[46] P. Angelikoulos, A. Gromov, A. Leen, O. Nerushev, H. Bock, and E. E. Campbell, "Dispersing individual single-wall carbon nanotubes in aqueous surfactant solutions below the cmc," *J. Phys. Chem C*, vol. 114, no. 1, pp. 2–9, 2010.

[47] R. Shvartzman-Cohen, E. Nativ-Roth, E. Baskaran, Y. Levi-Kalisman, I. Szleifer, and R. Yerushalmi-Rozen, "Selective dispersion of single-walled carbon nanotubes in the presence of polymers; the role of molecular and colloidal length scales," *J. Am. Chem. Soc.*, vol. 126, no. 45, pp. 14850–14857, 2004.

[48] Q. Wang, Y. Han, Y. Wang, Y. Qin, and Z.-X. Guo, "Effect of surfactant structure on the stability of carbon nanotubes in aqueous solution," *J. Phys. Chem. B*, vol. 112, no. 24, pp. 7227–7233, 2008.

[49] J.-Y. Shin, T. Premkumar, and K. E. Geckeler, "Dispersion of single-walled carbon nanotubes by using surfactants: Are the type and concentration important?," *Chem. Eur. J.*, vol. 14, no. 20, pp. 6044–6048, 2008.

[50] O. Matarredona, H. Rhoads, Z. Li, J. Harwell, L. Balzano, and D. E. Resasco *J. Phys. Chem.*, vol. 107, pp. 13357–13367, 2003.

[51] S. Utsumi, M. Kanamaru, H. Honda, H. Kanoh, H. Tanaka, T. Ohkubo, H. Sakai, M. Abe, and K. Kaneko, "Rbm band shift-evidenced dispersion mechanism of single-wall carbon nanotube bundles with naddbs," *J. Colloid Interface Sci.*, vol. 328, no. 1, pp. 276–284, 2007.

[52] X. Qi, W. Ping-Hua, J. Ling-Ling, T. Xiao-Ke, and O. Lin-Li, "Dispersion of carbon nanotubes in aqueous solution with cationic surfactant ctab," *Journal of Inorganic Materials*, vol. 22, no. 6, pp. 1122–1126, 2007.

[53] E. Wallace and M. Sansom, "Carbon nanotube/detergent interactions via coarse-grained molecular dynamics," *Nano Lett.*, vol. 7, no. 7, pp. 1923–1928, 2007.

[54] E. J. Wallace and M. S. P. Sansom, "Carbon nanotube self-assembly with lipids and detergent: a molecular dynamics study," *Nanotechnology*, vol. 20, no. 4, p. 045101 (6pp), 2009.

[55] R. Shvartzman-Cohen, M. Florent, D. Goldfarb, I. Szleifer, and R. Yerushalmi-Rozen, "Aggregation and self-assembly of amphiphilic block copolymers in aqueous dispersions of carbon nanotubes," *Langmuir*, vol. 24, no. 9, pp. 4625–4632, 2008.

[56] E. Nativ-Roth, R. Shvartzman-Cohen, C. Bounioux, M. Florent, D. Zhang, I. Szleifer, and R. Yerushalmi-Rozen, "Physical adsorption of block copolymers to swnt and mwnt: A nonwrapping mechanism," *Macromolecules*, vol. 40, no. 10, pp. 3676–3685, 2007.

[57] R. Qiao and P. Ke, "Lipid-carbon nanotube self-assembly in aqueous solution," *J. Am. Chem. Soc*, vol. 128, no. 42, pp. 13656–13657, 2006.

[58] T. Düren and F. J. Keil, "Molecular modeling of adsorption in carbon nanotubes," *Chem. Eng. Technol.*, vol. 24, no. 7, pp. 698–702, 2001.

[59] I. Gurevitcha and S. Srebnik, "Monte carlo simulation of polymer wrapping of nanotubes," *Chem. Phys. Lett.*, vol. 444, no. 1–3, pp. 96–100, 2007.

[60] N. R. Tummala and A. Striolo, "Sds surfactants on carbon nanotubes: Aggregate morphology," *ACS Nano*, vol. 3, no. 3, pp. 595–602, 2009.

[61] X. Zhijun, Y. Xiaoning, and Z. Yang, "A molecular simulation probing of structure and interaction for supramolecular sodium dodecyl sulfate/single-wall carbon nanotube assemblies," *Nano Lett.*, 2010. Article ASAP.

[62] N. M. Uddin, F. Capaldi, and B. Farouk, "Molecular dynamics simulations of carbon nanotube interactions in water/surfactant systems," *Journal of Engineering Materials and Technology*, vol. 132, no. 2, p. 021012, 2010.

[63] P. Angelikopoulos and H. Bock, "The differences in surfactant adsorption on carbon nanotubes and their bundles," *Langmuir*, vol. 26, no. 2, pp. 899–907, 2010.

[64] P. Angelikopoulos, S. Al-Harthy, and H. Bock, "Structural forces from directed self assembly," *J. Phys. Chem. B*, vol. 42, no. 113, pp. 13817–13824, 2009.

[65] P. Angelikopoulos and H. Bock, "Surfactant induced forces between carbon nanotubes," *Phys. Chem. Chem. Phys.*, 2010. submitted.

[66] E. W. Weisstein, "" Point-Line Distance–3-Dimensional." From MathWorld—A Wolfram Web Resource. `http://mathworld.wolfram.com/Point-LineDistance3-Dimensional.html`."

[67] T. Desai, P. Keblinski, and S. K. Kumar, "Computer simulations of the conformations of strongly adsorbed chains at the solid ??liquid interface," *Polymer*, vol. 47, p. 722, 2006.

[68] V. Kirsch *Adv. Colloid. Interfac.*, vol. 104, pp. 311–324, 2003.

[69] H. Tanaka, M. El-Merraoui, W. A. Steele, and K. Kaneko, "Methane adsorption on single-walled carbon nanotube: a density functional theory model," *Chem. Phys. Lett.*, vol. 352, pp. 334–341, 2002.

[70] N. Patel and S. Egorov, "Dispersing nanotubes with surfactants: A microscopic statistical mechanical analysis," *J. Am. Chem. Soc*, vol. 127, no. 41, pp. 14124–14125, 2005.

[71] B. Lee and F. M. Richards, "The interpretation of protein structures: estimation of static accessibility.," *J. Mol. Biol.*, vol. 55, no. 3, pp. 379–400, 1971.

[72] S. J. J. Wodak and J. Janin, "Analytical approximation to the accessible surface area of proteins.," *Proc. Natl. Acad. Sci. Unit. States. Am.*, vol. 77, pp. 1736–1740, April 1980.

[73] D. Leckband and J. Israelachvili, "Intermolecular forces in biology," *Q. Rev. Biophys.*, vol. 34, no. 02, pp. 105–267, 2001.

[74] Y. Lin and P. Alexandridis *Langmuir*, vol. 18, pp. 4220–4231, 2002.

[75] K. A., *Molecular Modeling of Proteins*. Humana Press, 2008.

[76] P. H. Hnenberger, "Thermostat algorithms for molecular dynamics simulations," in *Advanced Computer Simulation*, pp. 105–149, 2005.

[77] J. M. V. A. Koelman and P. J. Hoogerbrugge, "Dynamic simulations of hard-sphere suspensions under steady shear," *Europhysics Letters*, vol. 21, p. 363, 1993.

[78] M. Matsumoto and T. Nishimura, "Mersenne twister: a 623-dimensionally equidistributed uniform pseudo-random number generator," *ACM Trans. Model. Comput. Simul.*, vol. 8, no. 1, pp. 3–30, 1998.

[79] R. D. Groot and P. B. Warren, "Dissipative particle dynamics: Bridging the gap between atomistic and mesoscopic simulation," *J. Chem. Phys.*, vol. 107, no. 11, pp. 4423–4435, 1997.

[80] I. V. P. Nikunen, M. Karttunen, "How would you integrate the equations of motion in dissipative particle dynamics simulations?," *Computer Physics Communications*, vol. 153, p. 407, 2003.

[81] R. D. Groot and T. J. Madden, "Dynamic simulation of diblock copolymer microphase separation," *Journal of chemical physics*, vol. 108, p. 8713, 1998.

[82] C. Pastorino, K. Binder, and M. Mller, "Coarse-grained description of a brush:melt interface in equilibrium and under flow," *Macromolecules*, vol. 42, no. 1, pp. 401–410, 2009.

[83] C. Pastorino, T. Kreer, M. Müller, and K. Binder, "Comparison of dissipative particle dynamics and langevin thermostats for out-of-equilibrium simulations of polymeric systems," *Phys. Rev. E*, vol. 76, pp. 026706–026716, 2007.

[84] Z. Z. Iacovella, Mark A. Horsch and S. C. Glotzer, "Phase diagrams of self-assembled mono-tethered nanospheres from molecular simulation and comparison to surfactants," *Langmuir*, vol. 21, pp. 9488–9494, 2005.

[85] D. Frenkel and B. Smit, *Understanding Molecular Simulation*. Orlando, FL, USA: Academic Press, Inc., 2001.

[86] A. .Noske, *Efficient Algorithms for Molecular Dynamics Simulations and Other Dynamic Spatial Join Queries*. PhD thesis, 2004.

[87] S. Keith, "Surfactant induced forces between carbon nanotubes- a study of the tail length." Final Year Prject Report.

[88] T. H. Cormen, C. E. Leiserson, R. L. Rivest, and C. Stein, *Introduction to Algorithms, Second Edition*. The MIT Press, 2001.

[89] J. Israelachvili, "Self-assembly in two dimensions: Surface micelles and domain formation in monolayers," *Langmuir*, vol. 10, no. 10, pp. 3774–3781, 1994.

[90] M. R. Bohmer and L. K. Koopal, "Association and adsorption of nonionic flexible chain surfactants," *Langmuir*, vol. 6, no. 9, pp. 1478–1484, 1990.

[91] J.-P. Hansen and I. R. Mcdonald, *Theory of Simple Liquids, Third Edition*. Academic Press, 3 ed., April 2006.

[92] N. Chennamsetty, H. Bock, L. F. Scanu, F. R. Siperstein, and K. E. Gubbins, "Co-surfactant and cosolvent effects on surfactant self-assembly in supercritical carbon dioxide," *J. Chem. Phys.*, vol. 122, no. 9, pp. 094710–094721, 2005.

[93] K. Binder, "Modeling of wetting in restricted geometries," *Ann. Rev. Mat. Res.*, vol. 38, no. 1, pp. 123–142, 2008.

[94] C. Rascon and A. Parry, "Geometry-dominated fluid adsorption on sculpted solid substrates.," *Nature*, vol. 407, no. 6807, pp. 986–9, 2000.

[95] L. D. Gelb, K. E. Gubbins, R. Radhakrishnan, and M. Sliwinska-Bartkowiak, "Phase separation in confined systems," *Rep. Prog. Phys.*, vol. 62, no. 12, pp. 1573–1659, 1999.

[96] H. Bock and M. Schoen, "Phase behavior of a simple fluid confined between chemically corrugated substrates," *Phys. Rev. E*, vol. 59, pp. 4122–4136, Apr 1999.

[97] G. G. Pereira and D. R. M. Williams, "Diblock copolymer thin films on heterogeneous striped surfaces: Commensurate, incommensurate and inverted lamellae," *Phys. Rev. Lett.*, vol. 80, pp. 2849–2852, Mar 1998.

[98] M. M. Calbi, M. W. Cole, S. M. Gatica, M. J. Bojan, and G. Stan, "Condensed phases of gases inside nanotube bundles," *Rev. Mod. Phys.*, vol. 73, pp. 857–865, Nov 2001.

[99] L. Bruschi1 and M. G., "Adsorption within and on regularly patterned substrates," *J. Low. Temp. Phys.*, 2009. To appear.

[100] K. Sumithra and E. Straube, "Adsorption of diblock copolymers on stripe-patterned surfaces," *J. Chem. Phys.*, vol. 125, no. 15, p. 154701, 2006.

[101] J. J. Cerdá and T. Sintes, "Stiff polymer adsorption. onset to pattern recognition," *Biophys. Chem.*, vol. 115, no. 2-3, pp. 277 – 283, 2005.

[102] R. Shvartzman-Cohen, E. Nativ-Roth, E. Baskaran, Y. Levi-Kalisman, I. Szleifer, and R. Yerushalmi-Rozen, "Selective dispersion of single-walled carbon nanotubes in the presence of polymers: the role of molecular and colloidal length scales," *J. Am. Chem. Soc*, vol. 126, no. 45, pp. 14850–14857, 2004.

[103] J. J. Semler and J. Genzer, "Monte carlo simulations of copolymer adsorption at planar chemically patterned surfaces: Effect of surface domain sizes," *J. Chem. Phys.*, vol. 119, no. 10, pp. 5274–5280, 2003.

[104] X.-F. Wu and Y. A. Dzenis, "Guided self-assembly of diblock copolymer thin films on chemically patterned substrates," *J. Chem. Phys.*, vol. 125, no. 17, p. 174707, 2006.

[105] B. Duñweg and P. Wolfgang, "Brownian dynamics simulations without gaussian random numbers," *Int. J. Mod. Phys. C*, vol. 2, no. 3, pp. 817–827, 1991.

[106] R. Cyrille, B. Fabrice, S. Patrick, E. T. W, and M. Charles, "Supramolecular self-assembly of lipid derivatives on carbon nanotubes," *Science*, vol. 300, no. 5620, pp. 775–778, 2003.

[107] S. Talapatra and A. D. Migone, "Adsorption of methane on bundles of closed-ended single-wall carbon nanotubes," *Phys. Rev. B*, vol. 65, p. 045416, Jan 2002.

[108] L. Sarkisov and P. A. Monson, "Lattice model of adsorption in disordered porous materials: Mean-field density functional theory and monte carlo simulations," *Phys. Rev. E*, vol. 65, p. 011202, Dec 2001.

[109] L. Heroux, V. Krungleviciute, M. M. Calbi, and A. D. Migone, "Cf4 on carbon nanotubes; physisorption on grooves and external surfaces," *J. Phys. Chem. B*, vol. 110, no. 25, pp. 12597–12602, 2006.

[110] L. Grant and W. Ducker, "Effect of substrate hydrophobicity on surface-aggregate geometry: Zwitterionic and nonionic surfactants," *J. Phys. Chem. B*, vol. 101, no. 27, pp. 5337–5345, 1997.

[111] R. Strey, "Water-nonionic surfactant systems, and the effect of additives," *Ber. Bunsen Ges.*, vol. 100, no. 3, pp. 182–182, 1996.

[112] T. Futterer, T. Hellweg, G. H. Findenegg, J. Frahn, and A. D. Schluter, "Aggregation of an amphiphilic poly(p-phenylene) in micellar surfactant solutions. static and dynamic light scattering," *Macromolecules*, vol. 38, no. 17, pp. 7443–7450, 2005.

[113] C. Tanford, "Thermodynamics of micelle formation: Prediction of micelle size and size distribution," *Proc. Nat. Acad. Sci. U.S.A*, vol. 71, no. 5, pp. 1811–1815, 1974.

[114] R. Larson, "Monte carlo simulations of the phase behavior of surfactant solutions," *J. Phys. II*, vol. 6, pp. 1441–1463, oct 1996.

[115] R. Steitz, P. Muller-Buschbaum, S. Schemmel, R. Cubitt, and G. H. Findenegg, "Lateral structure of a surfactant layer adsorbed at a hydrophilic solid/liquid interface," *Europhys. Lett.*, vol. 67, no. 6, pp. 962–968, 2004.

[116] R. Shvartzman-Cohen, M. Florent, D. Goldfarb, I. Szleifer, and R. Yerushalmi-Rozen, "Aggregation and self-assembly of amphiphilic block copolymers in aqueous dispersions of carbon nanotubes," *Langmuir*, vol. 24, no. 9, pp. 4625–4632, 2008.

[117] G. Findenegg and A. Eltekov, "Adsorption isotherms of nonionic surfactants in sba-15 measured by micro-column chromatography," *J. Chromatogr. A*, vol. 1150, no. 1-2, pp. 236 – 240, 2007.

[118] O. Dietsch, A. Eltekov, H. Bock, K. E. Gubbins, and G. H. Findenegg, "Crossover from normal to inverse temperature dependence in the adsorption of nonionic surfactants at hydrophilic surfaces and pore walls;," *J. Phys. Chem. C*, vol. 111, no. 43, pp. 16045–16054, 2007.

[119] H. Bock and K. E. Gubbins, "Anomalous temperature dependence of surfactant self-assembly from aqueous solution," *Phys. Rev. Lett.*, vol. 92, p. 135701, Apr 2004.

[120] Z. Tang, L. E. Scriven, and H. T. Davis, "Effects of solvent exclusion on the force between charged surfaces in electrolyte solution," *J. Chem. Phys.*, vol. 100, no. 6, pp. 4527–4530, 1994.

[121] H. Bock and M. Schoen, "Thermomechanical properties of confined fluids exposed to a shear strain," *J. Phys.: Condens. Matter*, vol. 12, no. 8, pp. 1545–1568, 2000.

[122] S. H. L. Klapp and M. Schoen, "Spontaneous orientational order in confined dipolar fluid films," *J. Chem. Phys.*, vol. 117, no. 17, pp. 8050–8062, 2002.

[123] H. Bock, K. E. Gubbins, and K. G. Ayappa, "Solid/solid phase transitions in confined thin films: A zero temperature approach," *J. Chem. Phys.*, vol. 122, no. 9, p. 094709, 2005.

[124] S. H. L. Klapp, S. Grandner, Y. Zeng, and R. von Klitzing, "Asymptotic structure of charged colloids between two and three dimensions: the influence of salt," *J. Phys.: Condens. Matter*, vol. 20, no. 49, pp. 494232–494238, 2008.

[125] M. Heuberger, M. Zäch, and N. D. Spencer, "Density fluctuations under confinement: When is a fluid not a fluid?," *Science*, vol. 292, no. 5518, pp. 905–908, 2001.

[126] Q. Chen, C. Saltiel, S. Manickavasagam, L. S. Schadler, R. W. Siegel, and H. Yang, "Aggregation behavior of single-walled carbon nanotubes in dilute aqueous suspension," *J. Col. Interf. Sci.*, vol. 280, no. 1, pp. 91 – 97, 2004.

[127] M. S. Strano, "The role of surfactant absorption during ultrasonication in the dispersion of single-walled carbon nanotubes," *J. Nanosci. Nanotechnol.*, vol. 3, pp. 81–86, 2003.

[128] J. F. Cardenas and A. Gromov, "The effect of bundling on the raman band of single-walled carbon nanotubes," *Nanotechnology*, vol. 20, no. 46, p. 465703 (8pp), 2009.

[129] M. F. Islam, E. Rojas, D. M. Bergey, A. T. Johnson, and A. G. Yodh, "High weight fraction surfactant solubilization of single-wall carbon nanotubes in water," *Nano Lett.*, vol. 2, no. 3, pp. 269–273, 2003.

[130] B. White, S. Banerjee, S. O'Brien, N. J. Turro, and I. P. Herman, "Zeta-potential measurements of surfactant-wrapped individual single-walled carbon nanotubes," *J. Phys. Chem. C*, vol. 111, no. 37, pp. 13684–13690, 2007.

[131] R. Yerushalmi-Rozen and I. Szleifer, "Utilizing polymers for shaping the interfacial behavior of carbon nanotubes," *Soft Matter*, vol. 2, no. 1, pp. 24–28, 2006.